UNIVERSIDADE DE SÃO PAULO
INSTITUTO DE FÍSICA DE SÃO CARLOS

Pedro Monteiro Cônsoli

Extended Kitaev magnetism in magnetic fields

São Carlos

2020

Pedro Monteiro Cônsoli

Extended Kitaev magnetism in magnetic fields

Dissertation presented to the Graduate Program in Physics at Instituto de Física de São Carlos, Universidade de São Paulo, to obtain the degree of Master of Science.

Concentration area: Basic Physics

Supervisor: Prof. Dr. Eric de Castro e Andrade

Corrected version

(Original version available on the Program Unit)

São Carlos

2020

Cônsoli, Pedro Monteiro
Extended Kitaev magnetism in magnetic fields / Pedro Monteiro Cônsoli; advisor Eric de Castro e Andrade - corrected version -- São Carlos 2020.
129 p.

Dissertation (Master's degree - Graduate Program in Basic Physics) -- Instituto de Física de São Carlos, Universidade de São Paulo - Brasil , 2020.

1. Frustrated magnetism. 2. Heisenberg-Kitaev model. 3. Kitaev materials. 4. Spin-wave theory. 5. Exact diagonalization. I. Andrade, Eric de Castro e, advisor. II. Title.

ACKNOWLEDGEMENTS

I would like to begin by thanking my supervisor, Prof. Eric de Castro e Andrade. I am extremely grateful for our countless hours of discussions (sometimes grouped into a single day!), for your lessons on the importance of patience in research, and for the careful guidance throughout the three years since I first knocked on your door.

For welcoming me into his group as an exchange student and allowing me to live what proved to be a life-changing experience, I thank Prof. Matthias Vojta. Thank you as well to Dr. Lukas Janssen for joining us in many stimulating and fruitful discussions. I would also like to express my gratitude to Mrs. Tatjana Schoffer, whose help was invaluable during the difficult times of settling in Dresden.

I must thank a few professors whom, though not directly involved with the content of this dissertation, I consider to have had a great impact on my (so far short) journey as a scientist. To Prof. Leonardo Paulo Maia, thank you for always keeping an open door for discussions. Our chats during my freshman year, in particular, were one of the main reasons why I followed through with my undergraduate studies. To Prof. Cleber Renato Mendonça, thank you for being a true mentor and helping me find my way as a physicist. To Prof. Miled Hassan Youssef Moussa, thank you for showing me the first steps to become a theoretical physicist. To my dad, thank you for being my first reference as a scientist and for the always giving me wise advice. I also extend my gratitude to all the teachers and professors who had a role in my education.

I further acknowledge the São Paulo Research Foundation (FAPESP) for funding my studies, both in Brazil by means of Grant No. 2017/22133-3 and in Germany via Grant No. 2019/02099-0. For providing the basic services and infrastructure needed to develop my activities and for being a place I called home for nearly six years, I thank the São Carlos Institute of Physics (IFSC) of the University of São Paulo.

To all the friends I have made along the way, thanks for all the shared memories, for lightening the mood during good and tough times, and for just making life so much more enjoyable.

Finally, I would like to express my deepest gratitude to my family. To my grandpa Ailton, thank you for being such a huge example of perseverance in life. I have always admired your curiosity and hunger for knowledge, which are, to this day, a great inspiration for me. To my sister, “dona Lê”, thank you for your tenderness, companionship, and for making me want to be a better person in your eyes. To my parents, Fernando and Renata, thank you for never once casting doubt on my dreams, for pushing me to become the best version of myself, and, above all, for your unconditional love and support.

ABSTRACT

CÔNSOLI, P. M. **Extended Kitaev magnetism in magnetic fields**. 2020. 129p. Dissertation (Master of Science) - Instituto de Física de São Carlos, Universidade de São Paulo, São Carlos, 2020.

Over the past years, the physics of Kitaev's spin-1/2 honeycomb model and its extensions have attracted enormous interest, fueled by a pursuit of the fundamental understanding as well as experimental realizations of quantum spin-liquid phases. A notorious achievement in this field has been the discovery that, when applied in specific directions, a magnetic field can induce a gapped topological spin liquid in the Kitaev quantum magnet α-$RuCl_3$. In parallel, the search for other magnets with strong spin-orbit coupling has resulted in recent proposals of material candidates to host spin-1 and spin-3/2 analogs of the Kitaev interaction. Remarkably, all of these materials display nontrivial responses to magnetic fields, such as strongly anisotropic magnetization processes and novel field-induced states, due to the lack of spin-rotational symmetry. Given such a rich background, this dissertation aims at expanding the current knowledge of the effects of magnetic fields on extended Kitaev systems with three different contributions. First, we employ a combination of linear and nonlinear spin-wave theory to study the ordered field-induced phases of the nearest-neighbor Heisenberg-Kitaev model, which is often regarded as a minimal model to describe Kitaev magnetism for different spin quantum numbers S. By developing a consistent $1/S$ expansion, we analyze the influence of the leading-order quantum fluctuations on physical observables and phase diagrams of the experimentally relevant cases of $S = 1/2$, 1 and 3/2. Second, we consider a more realistic spin model to describe the low-temperature elastic response of α-$RuCl_3$ in an applied magnetic field and small uniaxial pressure. Our results suggest that anomalous features found in experiments are indicative of an intermediate-field quantum paramagnetic regime. Finally, we return to the Heisenberg-Kitaev model in a magnetic field, but by now applying the numerical technique of exact diagonalization for $S = 1/2$. Besides finding good agreement with our spin-wave calculations, we report possible evidence for a new quantum tricritical point.

Keywords: Frustrated magnetism. Heisenberg-Kitaev model. Kitaev materials. Spin-wave theory. Exact diagonalization.

RESUMO

CÔNSOLI, P. M. **Magnetismo de Kitaev estendido em campos magnéticos**. 2020. 129p. Dissertação (Mestrado em Ciências) - Instituto de Física de São Carlos, Universidade de São Paulo, São Carlos, 2020.

Nos últimos anos, a física do modelo de spin-1/2 de Kitaev na rede favo de mel e de suas generalizações tem atraído um enorme interesse, motivado pela busca pela compreensão de aspectos fundamentais e realizações experimentais de líquidos de spin quânticos. Um avanço notório nessa área foi a descoberta de que, quando aplicado em direções específicas, um campo magnético é capaz de induzir um líquido de spin topológico com *gap* no magneto quântico α-$RuCl_3$. Em paralelo, a busca por outros materiais magnéticos com forte acoplamento spin-órbita resultou em propostas recentes de candidatos a realizar versões de spin-1 e spin-3/2 da interação de Kitaev. Notavelmente, a ausência de simetria de rotação de spin nesses sistemas induz processos de magnetização altamente anisotrópicos e novos estados magnéticos. Dado um contexto tão rico, esta dissertação tem como objetivo aprofundar o conhecimento dos efeitos de campo magnéticos em sistemas de Kitaev generalizados por meio de três contribuições. Primeiro, nós empregamos uma combinação de teoria de ondas de spin lineares e não-lineares para estudar as fases ordenadas induzidas por campos magnéticos no modelo Heisenberg-Kitaev, tipicamente tido como um modelo mínimo para descrever magnetismo de Kitaev para diferentes números quânticos de spin S. Com o desenvolvimento de uma expansão consistente em $1/S$, nós analisamos a influência de flutuações quânticas de primeira ordem em observáveis físicos e nos diagramas de fases dos casos experimentalmente relevantes de $S = 1/2$, 1 e 3/2. Segundo, nós consideramos um modelo de spins mais realístico para descrever a resposta elástica a baixas temperaturas de α-$RuCl_3$ em um campo magnético externo e sob pressão uniaxial pequena. Nossos resultados sugerem que aspectos anômalos encontrados em experimentos indicam a presença de um regime quântico a campos intermediários. Finalmente, retornamos ao modelo de Heisenberg-Kitaev em um campo magnético, porém agora empregando a técnica numérica de diagonalização exata para $S = 1/2$. Além de obter resultados em bom acordo com o nosso estudo de ondas de spin, nós reportamos possíveis evidências para um novo ponto tricrítico quântico.

Palavras-chave: Magnetismo frustrado. Modelo de Heisenberg-Kitaev. Materiais Kitaev. Teoria de ondas de spin. Diagonalização exata.

LIST OF FIGURES

LIST OF TABLES

LIST OF ABBREVIATIONS AND ACRONYMS

AF	Antiferromagnetic
BZ	Brillouin zone
DMRG	Density matrix renormalization group
ED	Exact diagonalization
FM	Ferromagnetic
GSL	Gapless spin liquid
HK	Heisenberg-Kitaev
KSL	Kitaev spin liquid
LSW	Linear spin-wave
LSWT	Linear spin-wave theory
MS	Magnetostriction
NLO	Next-to-leading order
ObD	Order-by-disorder
QCP	Quantum critical point
QSL	Quantum spin liquid
TE	Thermal expansion

CONTENTS

1 INTRODUCTION

Over the past decades, the search for unconventional phases of matter has played a decisive role in shaping our understanding of nature and expanding the frontiers of condensed matter physics. Much of the progress achieved in this direction owes to remarkable advancements in material sciences, which have consistently improved the control over the synthesis of new compounds. Guided by the growing knowledge of the microscopic mechanisms behind effective interactions in solids, this trend has created the possibility of engineering materials with unusual physical properties. In particular, strong spin-orbit coupling has been singled out as a key ingredient to generate novel states of matter in both metallic and insulating systems.[9–14]

In the context of magnetic insulators, the interplay of strong spin-orbit coupling and strong electronic correlations provides a route to the realization of bond-directional interactions between magnetic degrees of freedom.[15] Several instances of this connection are now known to arise in Mott insulators constituted of magnetic ions with partially filled $4d$ or $5d$ shells.[3,16–22] Among such systems, the so-called Kitaev materials have attracted enormous interest as hosts for the Ising-like bond-dependent interactions which lie at the heart of Kitaev's celebrated honeycomb model.[3,17–19]

In its original form,[23] Kitaev's honeycomb model describes a system of spins 1/2 located at the vertices of a honeycomb lattice. Despite the frustrated nature of the spin interactions, the model admits an exact solution over its entire parameter space. Such a remarkable feature acquires special significance due the fact that the resulting ground states are different quantum spin liquids (QSLs), exotic phases of matter with fascinating properties such as long-range quantum entanglement, fractional excitations, and emergent gauge structures.[24–26] In the case of the Kitaev model, the last two properties manifest as the excitations take the forms of Majorana fermions and fluxes in a $\mathbb{Z}_2$ gauge field. While the latter are always gapped, the existence of a gapless Majorana spectrum in one of the phases sets it apart from the others. The low-energy excitations of this gapless QSL consist of itinerant Majorana fermions in a static $\mathbb{Z}_2$ background. Interestingly, a magnetic field can open a gap in the Majorana spectrum, so as to induce a transition to a nonabelian QSL that exhibits chiral Majorana edge modes.[23]

As a result of an intense search for Kitaev materials, it is now well established that Kitaev interactions are particularly strong in the honeycomb iridates[27–29] $A_2\mathrm{IrO}_3$ ($A = \mathrm{Li}, \mathrm{Na}$) and α-RuCl_3,[30–32] wherein Ir^{4+} and Ru^{3+} ions form effective $j_{\mathrm{eff}} = 1/2$ local magnetic moments distributed in stacked honeycomb planes. Nevertheless, the fact that these materials exhibit long-range magnetic order at sufficiently low temperatures indicates that other exchange interactions come into play and prevent the stabilization of a Kitaev

QSL phase. Still, this by no means renders the resulting physics dull nor discourages the quest for QSLs in Kitaev materials. Both experimental[5,33–35] and theoretical[1,36–39] efforts have demonstrated that the frustrated nature of the interactions gives rise to highly anisotropic responses in applied magnetic fields. These effects are particularly intriguing in α-$RuCl_3$, for which a moderate in-plane magnetic field can drive transitions between different magnetic ordered states[40,41] before inducing a gapped quantum paramagnet.[8,42,43] By now, several experiments suggest that this intermediate-field state corresponds to a QSL regime.[41,44–52] Perhaps the most striking evidence to support this proposal is the measurement of an approximate half-integer quantized thermal Hall conductivity in tilted magnetic fields,[44,51] which provides a direct link with the chiral Majorana edge modes predicted to arise in the Kitaev model.[53–55]

In parallel, the interest in finding different routes to realize QSLs and in uncovering novel magnetic phenomena in spin-orbit-coupled magnets has resulted in recent proposals of material candidates to host higher-spin analogs of the Kitaev interaction.[22,56] Though Kitaev interactions also seem to be dominant in this new class of materials, all candidates studied thus far exhibit long-range magnetic order at sufficiently low temperatures.[22,56–58] As in the spin-1/2 case, this calls for a study of the nature of additional interactions and their influence on the magnetic properties of these systems.

In this context, our main goal here is to expand the current understanding of the effects of magnetic fields on extended Kitaev systems, in which the Kitaev exchange coexists with other forms of spin-spin interactions. We shall be primarily interested in analyzing the influence of quantum fluctuations on the stability and thermodynamic behavior of field-induced magnetic phases predicted to occur in the classical limit. We then divide the remainder of this dissertation as follows:

- Chapter 2 is devoted to providing a deeper background on Kitaev magnetism and a few of its realizations in solid state systems. We begin by outlining the exact solution of Kitaev's honeycomb model and discussing some of its main physical properties, both in the absence and in the presence of an applied magnetic field. Next, we turn to the matter of how Kitaev interactions come about in real materials and use our conclusions to present extended spin models. In this regard, we shall be particularly interested in the nearest neighbor Heisenberg-Kitaev model, which is often considered as a minimal model to capture the main aspects of Kitaev materials in general, and in a more focused description for α-$RuCl_3$. We also discuss a few recent experimental results concerning α-$RuCl_3$ and higher-spin Kitaev materials.

- Chapter 3 lays the foundations of linear spin-wave theory, the main tool we have used in our investigations. We already shape our discussion so that it becomes appropriate for the two following chapters.

- In Chapter 4, we deal with the physics of the nearest-neighbor Heisenberg-Kitaev model in external magnetic fields applied along different directions. After reviewing classical results, we develop a comprehensive and systematic framework to study the effect of leading-order quantum fluctuations by means of a $1/S$ expansion, where S is the spin size. Importantly, we demonstrate that the noncollinearity of the field-induced magnetic states requires elements of nonlinear spin-wave theory for a consistent treatment. Our results show that substantial modifications to the classical phase diagrams and physical observables follow for small values of S, which are those of experimental interest. Furthermore, we argue that our work stands as an accessible analytical formalism to complement numerical methods in the study of spin models with broken spin-rotational symmetry.

- In Chapter 5, we take up the task of modeling the magnetic properties of α-$RuCl_3$. By using the tools developed in Chapter 3, we analyze the low-temperature elastic response of the material under uniaxial pressure and in an in-plane magnetic field. When compared to measurements performed by an experimental group from the IFW Dresden, our results support the interpretation of specific features found in experiment as signatures of an intermediate-field quantum paramagnetic regime. The key contribution of this undertaking is to provide thermodynamic evidence for the existence of an upper boundary of the putative QSL regime, which had been scarce before.

- In Chapter 6, we return to the analysis of the Heisenberg-Kitaev model in a magnetic field, but now by employing the numerical method of exact diagonalization for $S = 1/2$. Besides complementing our conclusions from Chapter 4, our findings provide a topic for future research, as they point toward the possible existence of a novel quantum tricritical point.

- We conclude in Chapter 7 by summarizing our achievements and providing an outlook for future work.

2 THE KITAEV HONEYCOMB MODEL AND ITS EXTENSIONS TO REAL MATERIALS

2.1 The Kitaev honeycomb model

2.1.1 Exact solution

The Kitaev honeycomb model[23] describes a system of spins 1/2 sitting on the vertices of a honeycomb lattice, and interacting with each other via nearest-neighbor Ising exchanges. These interactions, however, are tailored to exhibit an intrinsic bond-dependent nature, as the relevant spin component for each pair of spins (ij) is determined by the spatial orientation of the bond connecting both sites. Explicitly, we can distinguish the three different types of bonds on the honeycomb lattice by the label $\gamma \in \{x, y, z\}$, as shown in Fig. 1(a), and write the Kitaev Hamiltonian as[23]

$$\mathcal{H}_{\mathrm{K}} = \sum_{\gamma=x,y,z} \sum_{\langle ij \rangle_\gamma} K_\gamma \sigma_i^\gamma \sigma_j^\gamma, \tag{2.1}$$

where K_γ are model parameters and σ^γ denote Pauli matrices. Interestingly, the three interactions involving any given site cannot be simultaneously satisfied. Such an *exchange frustration* results in a massive degeneracy of the classical ground state, which grows exponentially with the system size.[59] This is known to be a crucial ingredient to generate quantum spin-liquid phases.[24]

Most prominent, however, is the fact that Eq. (2.1) hosts an extensive number of conserved quantities. In particular, for every plaquette (i.e., hexagon) p on the lattice, one

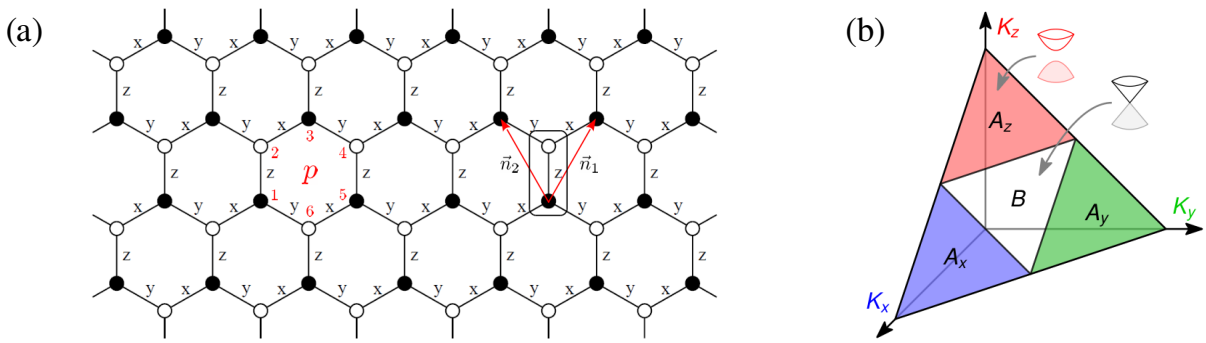

Figure 1 – (a) Representation of the honeycomb lattice containing a given convention of bond labels. We also show the unit cell of the lattice and its primitive vectors, $\mathbf{n}_1$ and $\mathbf{n}_2$. (b) Section of the plane $K_x + K_y + K_z = \text{const.}$ in the first octant of the parameter space. While the three A phases are gapped, the B phase has gapless Majorana excitations at zero external field.

Source: (a) Adapted from KITAEV.[23] (b) JANSSEN; VOJTA.[60]

can define a plaquette operator

$$W_p := \sigma_1^x \sigma_2^y \sigma_3^z \sigma_4^x \sigma_5^y \sigma_6^z \tag{2.2}$$

which commutes with $\mathcal{H}_\mathrm{K}$. As illustrated in Fig. 1(a), each of the six spin operators on the vertices of p enters Eq. (2.2) with a component given by the bond lying outside of the plaquette. Since $W_p^2 = \mathbb{1}$, the eigenvalues of W_p are $w_p = \pm 1$. Moreover, because $[W_p, W_q] = 0$ for any two plaquettes p and q on lattice, we can divide the Hilbert space into eigenspaces (sectors) labeled by different sets of eigenvalues $\{w_p\}$.

While the identification of W_p as constants of motion simplifies the problem considerably, it does not provide a route for an exact solution on its own. If N and N_p, respectively, denote the total number of sites and plaquettes in the system, then the dimension of each eigenspace is equal to $2^N/2^{N_p} \approx 2^{N/2}$. Thus, although reduced, the dimension of the Hilbert space one has to work in still increases exponentially with the system size.

Kitaev showed that the problem can be solved by ingeniously representing the spin degrees of freedom in terms of Majorana fermions.[23] To establish a connection with what is perhaps a more familiar setting, we recall that the Abrikosov pseudo-fermion representation[61] describes a spin operator $\boldsymbol{\sigma}_i = (\sigma_i^x, \sigma_i^y, \sigma_i^z)$ by combining two complex fermion modes $a_{i1}, a_{i1}^\dagger$ and $a_{i2}, a_{i2}^\dagger$, which satisfy the anticommutation relations $\left\{a_{i\alpha}, a_{i\beta}^\dagger\right\} = \delta_{\alpha\beta}$ and $\{a_{i\alpha}, a_{i\beta}\} = 0$. One can then define the *Majorana fermions*

$$\begin{aligned} b_i^x &:= a_{i1}^\dagger + a_{i1}, & b_i^y &:= \mathrm{i}\left(a_{i1}^\dagger - a_{i1}\right), \\ b_i^z &:= a_{i2}^\dagger + a_{i2}, & c_i &:= \mathrm{i}\left(a_{i2}^\dagger - a_{i2}\right). \end{aligned} \tag{2.3}$$

Besides being Hermitian, these operators obey the anticommutation relations

$$\left\{b_i^\alpha, b_j^\beta\right\} = 2\delta_{ij}\delta_{\alpha\beta}, \qquad \{c_i, c_j\} = 2\delta_{ij}, \qquad \{b_i^\alpha, c_j\} = 0. \tag{2.4}$$

However, it is important to realize that, while the local Hilbert space of a spin is two-dimensional, two complex fermions or, equivalently, four Majorana fermions act on an extended four-dimensional Fock space, $\widetilde{\mathscr{F}}_i$. Therefore, a valid representation of spin operators necessarily requires a constraint to eliminate redundant degrees of freedom. Keeping this in mind, we consider the following representation:

$$\tilde{\sigma}_i^\gamma = \mathrm{i}\, b_i^\gamma c_i. \tag{2.5}$$

Although Eqs. (2.4) guarantee the validity of $(\tilde{\sigma}_i^\gamma)^2 = \mathbb{1}$ and $(\tilde{\sigma}_i^\gamma)^\dagger = \tilde{\sigma}_i^\gamma$, the relation $\tilde{\sigma}_i^x \tilde{\sigma}_i^y \tilde{\sigma}_i^z = \mathrm{i} b_i^x b_i^y b_i^z c_i \neq \mathrm{i}$ shows that Eq. (2.5) does not fulfill SU(2) algebra in $\widetilde{\mathscr{F}}_i$. It then becomes clear that we must introduce a constraint operator $D_i := b_i^x b_i^y b_i^z c_i$ for every site i to define a *physical* subspace $\mathscr{F} \subset \widetilde{\mathscr{F}} = \otimes_i \widetilde{\mathscr{F}}_i$ such that

$$|\psi\rangle \in \mathscr{F} \iff D_i |\psi\rangle = |\psi\rangle\,, \ \forall\, i. \tag{2.6}$$

By noting that $D_i^2 = \mathbb{1}$, we find that Eq. (2.5) fulfills SU(2) algebra in $\mathscr{F}$, since $\tilde{\sigma}_i^x \tilde{\sigma}_i^y \tilde{\sigma}_i^z |\psi\rangle = \mathrm{i} D_i |\psi\rangle = \mathrm{i} D_i (D_i |\psi\rangle) = \mathrm{i}$ for any $|\psi\rangle \in \mathscr{F}$.

We can then employ Eq. (2.5) to construct the extended version of the Kitaev Hamiltonian

$$\tilde{\mathcal{H}}_{\mathrm{K}} = -\mathrm{i} \sum_{\gamma=x,y,z} \sum_{\langle ij \rangle_\gamma} K_\gamma \hat{u}_{ij} c_i c_j, \tag{2.7}$$

where we have defined $\hat{u}_{ij} := \mathrm{i}\, b_i^\gamma b_j^\gamma$ for nearest neighbor sites i and j connected by a γ-bond. Here, the problem is once again simplified by the existence of integrals of motion: The fact that $\left[\tilde{\mathcal{H}}_{\mathrm{K}}, \hat{u}_{ij}\right] = [\hat{u}_{ij}, \hat{u}_{kl}] = 0$ enables us to divide $\widetilde{\mathscr{F}}$ into orthogonal eigenspaces of $\hat{u}_{ij}$ and to evaluate $\tilde{\mathcal{H}}_{\mathrm{K}}$ at a fixed set of eigenvalues $\{u_{ij}\}$. Because $\hat{u}_{ij}^2 = \mathbb{1}$, each of these eigenvalues can only take on the values ± 1. Therefore, Eq. (2.7) reduces to a quadratic Hamiltonian of itinerant Majorana fermions coupled to a static $\mathbb{Z}_2$ gauge field, which is represented by the set $\{u_{ij}\}$. Such a remarkable feature consists of an example of the *fractionalization* of spin degrees of freedom.

It is crucial to realize that, after diagonalizing the quadratic Majorana hopping Hamiltonian for a certain set of eigenvalues $\{u_{ij}\}$, one has to project $|\psi_u\rangle \in \widetilde{\mathscr{F}}$ onto the physical subspace $\mathscr{F}$ by means of the operator $\mathcal{P} = \prod_i (1 + D_i)/2$, which filters out all components of $|\psi_u\rangle$ which do not respect Eq. (2.6). By showing that $\{D_i, \hat{u}_{ij}\} = 0$, one perceives that each D_i operator has the effect of changing the signs of the three eigenvalues u_{ij} emanating from site i,* and hence that $\mathcal{P}$ mixes states from different $\{u_{ij}\}$ sectors. Thus, a single eigenvalue u_{ij} does not carry physical significance. The actual physical quantities are the eigenvalues of

$$\tilde{W}_p = \prod_{(ij) \in \partial p} \hat{u}_{ij}, \tag{2.8}$$

which remain invariant after projection (i.e., are gauge-invariant) since $\left[\tilde{W}_p, \mathcal{P}\right] = 0$. Nonetheless, as one can easily verify by substituting Eq. (2.5) into Eq. (2.2), $\tilde{W}_p$ is just the extended version of the plaquette operator W_p. Consequently, different $\{u_{ij}\}$ sets that lead to the same $\{w_p\}$ eigenvalues are equivalent, in the sense that they give the same physical eigenstates.

In order to analyze the ground state of the model, one must therefore determine the configuration $\{w_p\}$ that minimizes the ground-state energy of the quadratic Majorana Hamiltonian. Fortunately, the solution to this nontrivial problem is given by Lieb's theorem,[62] which asserts that the ground state belongs to the sector with $w_p = +1$ for all plaquettes p†. A simple way to fulfill this condition is to take $u_{ij} = 1$ over all links (ij)

* More explicitly: $\hat{u}_{ij} (D_i |\psi_u\rangle) = -D_i \hat{u}_{ij} |\psi_u\rangle = -u_{ij} D_i |\psi_u\rangle$

† Actually, Lieb's theorem determines the ground state sector for any lattice that possesses a mirror symmetry with respect to a plane which does not contain any sites. In this general case, the corresponding values of w_p depend on the length of the elementary plaquette of the lattice.[62,63]

in Eq. (2.7). After doing so, one can diagonalize the Hamiltonian by means of a Fourier transform. Remarkably, the resulting dispersion can either be gapped or gapless, depending on the relative values of the parameters K_γ. If the triangle inequality $|K_\gamma| > |K_\alpha| + |K_\beta|$ is satisfied for some permutation $\{\alpha, \beta, \gamma\}$ of $\{x, y, z\}$, then the system will find itself in one of the three gapped A_γ phases shown in Fig. 1(b). Since "matter" excitations in the form of Majorana fermions have a finite energy cost, the low-energy degrees of freedom are, in this case, flux excitations, i.e., changes in pairs of eigenvalues w_p. On the other hand, the system enters a gapless B phase as one approaches the isotropic point $K_\gamma = K$, $\forall\, \gamma$. Thus, for energies below the $\mathbb{Z}_2$ flux gap, the excitations in this phase are Majorana fermions. We note that these spectral properties hold for all eight sign combinations of K_x, K_y and K_z. That is because, in an infinite honeycomb lattice, a change in the sign of a certain K_γ coupling constant is equivalent to a gauge transformation which does not affect the set $\{w_p\}$ or, in a different perspective, to a unitary transformation to the Hamiltonian.[23]

Another remarkable property follows from the fact that, because W_p does not commute with the spin operators σ_i^γ, a state with a definite set of $\{w_p\}$ eigenvalues cannot exhibit long-range magnetic order. This is one of the reasons why the ground state of the system consists of a $\mathbb{Z}_2$ quantum spin liquid. In particular, the ground state of the B phase is called the *Kitaev spin liquid* (KSL).

It was later realized that the Kitaev model is exactly solvable in any tricoordinated lattice, regardless of the lattice geometry and its spatial dimension.[64] This launched an intense line of research, which seeks to explore how manipulating geometric ingredients can lead to qualitatively different quantum spin liquids. Put together with the discovery that similar forms of interaction also exist in orbital models,[20] these generalizations reassert the relevance of Kitaev physics and motivate continuing investigation of the properties of the original model as well as of its extensions.

2.1.2 Kitaev model in a magnetic field

Even though the Kitaev model has many intriguing properties already in its pure form, Eq. (2.1), much of the tremendous interest it continues to attract up to date follows from its exotic behavior under applied magnetic fields.[60] Let us then consider the effect of a uniform magnetic field $\mathbf{h} = (h_{x,}, h_y, h_z)$ on the system. More specifically, we shall verify if the field introduces a gap in the spectrum of the B phase, for, if that happens, quantized chiral edge modes are expected to arise by analogy with the quantum Hall effect. For simplicity, we assume that $K_\gamma = K$, $\forall\, \gamma$ from now on.

One can then construct an effective Hamiltonian $\mathcal{H}_{\text{eff}}$ acting on the ground-state sector by treating the Zeeman term

$$V = -\mathbf{h} \cdot \sum_i \boldsymbol{\sigma}_i \tag{2.9}$$

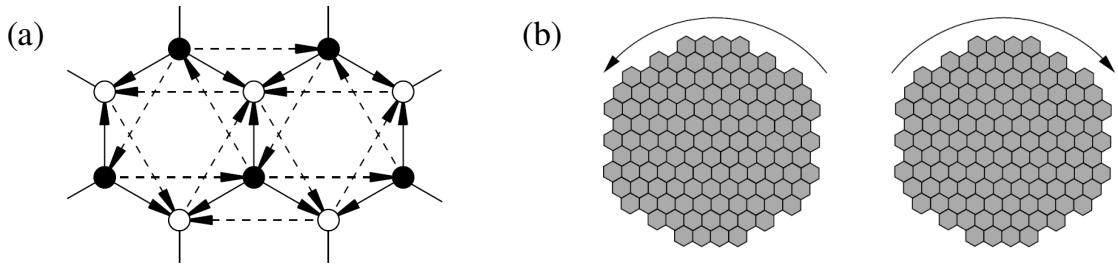

Figure 2 – (a) Connectivity diagram related to the effective Hamiltonian, Eq. (2.10). (b) Counterclockwise and clockwise chiral edge modes.

Source: KITAEV.[23]

as a perturbation to $\mathcal{H}_{\mathrm{K}}$. While the first nonzero contribution comes at second order of perturbation theory, the fact that it preserves time-reversal symmetry keeps it from opening a spectral gap.[23] On the basis of a qualitative argument, however, Kitaev was able to show that the third-order term necessarily breaks this symmetry and generates an effective hopping between next-nearest neighbors with amplitude η. We are thus left with

$$\mathcal{H}_{\mathrm{eff}} = -\frac{\mathrm{i}}{2}\left[K\sum_{ij}(\longleftarrow)_{ij}\,c_i c_j + \eta\sum_{ij}(\leftarrow\!\!-\!-)_{ij}\,c_i c_j\right], \qquad \eta \sim \frac{h_x h_y h_z}{K^2}. \tag{2.10}$$

Here, the arrows represent connectivity matrices between different sites: One must substitute $(\longleftarrow)_{ij}$ by 1 if there is a solid arrow from j to i in Fig. 2(a), by -1 if the arrow goes from i to j, and by 0 otherwise. The dashed arrow is defined similarly.

After applying a Fourier transform to diagonalize $\mathcal{H}_{\mathrm{eff}}$, one finds that the dispersion acquires a mass term proportional to $|\eta|$, and hence becomes gapped as long as the magnetic field couples to all three spin components. This new phase, called *gapped* KSL[‡], is regarded as an important toy model for potential applications in topological quantum computation because its effective excitations obey nonabelian anyonic statistics.[23,65] By means of the standard theory of topological insulators,[66] one can further verify that the spectral Chern number of the system is equal to the sign of η, so that gapless chiral edge modes appear for any field configuration with $\eta \neq 0$, see Fig. 2(b). Differently from the (electronic) quantum Hall effect, however, these edge modes consist of thermal rather than electric currents, since the carriers are the charge-neutral Majorana fermions. Moreover, the fact that each complex fermion corresponds to a pair of Majorana fermions with twice as many degrees of freedom gives rise a *half-integer thermal Hall effect*, in which the quantized thermal Hall conductivity is equal to $\kappa_{xy}/T = \frac{1}{2}\left[(\pi k_{\mathrm{B}}^2)\,/\,(6\hbar)\right]$.[23] For temperatures which are sufficiently small in comparison to the $\mathbb{Z}_2$ flux gap, this behavior remains robust and provides a unique signature of chiral Majorana edge modes.

‡ The term "gapped" is often omitted when context clarifies which of the Kitaev spin liquids is the object of the discussion.

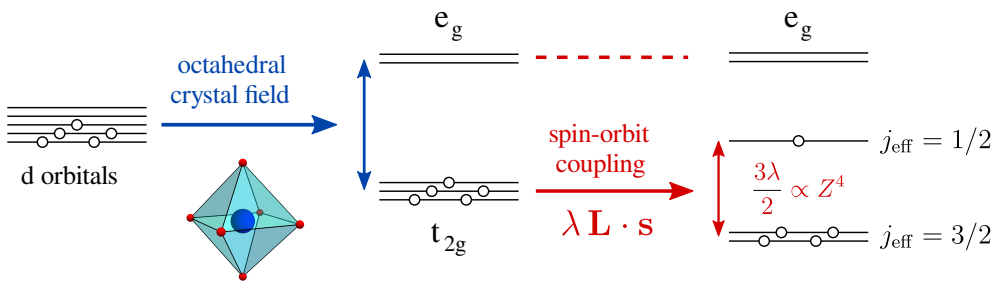

Figure 3 – Microscopic mechanism leading to the formation of $j_{\rm eff} = 1/2$ magnetic moments in d^5 transition ions. The red spheres at the vertices of the octahedron represent nonmagnetic A anions, whereas the blue sphere at the center is the magnetic D cation.

Source: By the author.

Over the past few years, much knowledge has been gained about the behavior of this system beyond the perturbative limit of $h \ll |K|$. It is now well established that a magnetic field introduces an asymmetry between the ferromagnetic ($K_\gamma = K < 0,\ \forall\ \gamma$) and antiferromagnetic ($K_\gamma = K > 0,\ \forall\ \gamma$) models. When $K < 0$, the gapped KSL undergoes a direct transition to the high-field polarized phase at relatively small fields ($h \approx 0.02\,|K|$).[4,67] On the other hand, it is found to survive up to considerably larger values of h when $K > 0$.[4,68] In this case, several numerical[4,68–73] and analytical studies[74,75] have converged to the conclusion that a new topological phase arises at intermediate magnitudes of [001] and [111] magnetic fields, and remains stable over a wide range of field directions[4] and also in the presence of small additional spin-spin interactions.[4,71] Current understanding suggests that this phase is a U(1) gapless spin liquid (GSL).[4,71–73] In Chapter 6, we shall discuss the stability of the GSL in the context of the so-called Heisenberg-Kitaev model.

2.2 Generalized Kitaev magnetism: Extended models and real materials

2.2.1 Microscopic origin of the spin-1/2 Kitaev exchange

The exact solution of Kitaev's honeycomb model sparked an intense search for materials that exhibit the Kitaev interaction, as well as for a physical mechanism capable of explaining its manifestation in solid-state systems. Besides the potential application in quantum computation,[23,65] these efforts were driven by fundamental purposes, such as the interest in synthesizing spin liquid materials, finding experimental proof for the existence of Majorana fermions and directly probing the gauge physics underlying the KSL.

Arguably, a few clues as to the correct path to pursue were already available at the time this quest was launched. It had long been known that strong electronic correlations in Mott insulators are not only responsible for generating electronic properties outside of the scope of usual band theory, but also give rise to interesting magnetic behavior. Ever since

the discovery of high-T_c superconductivity in cuprates,[76] compounds featuring transition metal cations with partially filled d orbitals became an extensively studied class of Mott insulators. In these systems, each cation D is usually surrounded by an octahedral cage of nonmagnetic anions A, and is thus subject to an effective electric field generated by the six anions located at the vertices of the octahedron. By breaking the spherical symmetry of the Coulomb potential, this *crystal field* splits the five d orbitals of the cation into a low-lying triplet, t_{2g}, and a higher-energy doublet, e_g, as represented in Fig. 3. The projection of the orbital angular momentum operator $\mathbf{L}$ onto each of these orbital subspaces shows that the e_g and t_{2g} states have effective angular momenta characterized by orbital quantum numbers $\ell = 0$ and $\ell = 1$, respectively.[77]

An important step toward discovering the origin of Kitaev interactions was to add strong spin-orbit coupling as an ingredient to this type of system.[14,19] While the e_g states remain unaffected, the t_{2g} orbitals couple to the electron spins $\mathbf{s}$ and have their degeneracy lifted, as illustrated on the right-hand side of Fig. 3. This results in a lower-energy quartet with effective angular momentum $j_{\text{eff}} = 3/2$, which is separated from a higher-energy $j_{\text{eff}} = 1/2$ doublet by a gap proportional to the spin-orbit coupling constant, λ. Therefore, when the on-site repulsion (Hubbard U) is much larger than the typical hopping amplitude t, D ions with d^5 filling have local $j_{\text{eff}} = 1/2$ magnetic moments as low-energy degrees of freedom.[16,78] Such *pseudospin* degrees of freedom are expected to be more stable in heavier transition ions ($4d^5$ or $5d^5$), because λ scales with the atomic number Z of the cation to the fourth power.[11] Furthermore, they essentially inherit the spatial anisotropy of the d orbitals via spin-orbit entanglement.[15,19] By considering the specific example of layered cobalt oxides, Khaliullin showed that this leads to effective spin-1/2 models with bond-dependent exchanges.[16]

Although this mechanism was known to generate bond-dependent "spin"-1/2 interactions at the time Kitaev published his seminal article, engineering a system with an appreciable Kitaev exchange still remained a challenge. The reason for such a difficulty is that the leading contributions ($\propto t^2/U$) to interactions are constrained by a hidden symmetry[79,80] which only allows the Kitaev exchange to emerge at subleading orders (at best $\propto J_{\text{H}}\, t^2/U^2$, where J_{H} is Hund's coupling).[19] This obstacle, however, was overcome in 2009 by Jackeli and Khaliullin.[17] While studying the case in which hopping only occurs between the t_{2g} orbitals of D cations via the intervening p-orbitals of the A anions, they realized that the form of the interactions depends sensitively on the geometric arrangement of neighboring octahedra. In particular, a configuration of idealized edge-sharing octahedra causes the two D-A-D hopping paths shown in Fig. 4(a) to interfere in such a way that all interactions vanish at order t^2/U. Remarkably, the same happens to all next-to-leading order contributions except a ferromagnetic (FM) Kitaev term, which arises as a dominant coupling. By uncovering this physical mechanism, Jackeli and Khaliullin were able to propose honeycomb iridates such as Na_2IrO_3 and Li_2IrO_3 ($D = Ir^{4+}$ and $A = O^{2-}$), in

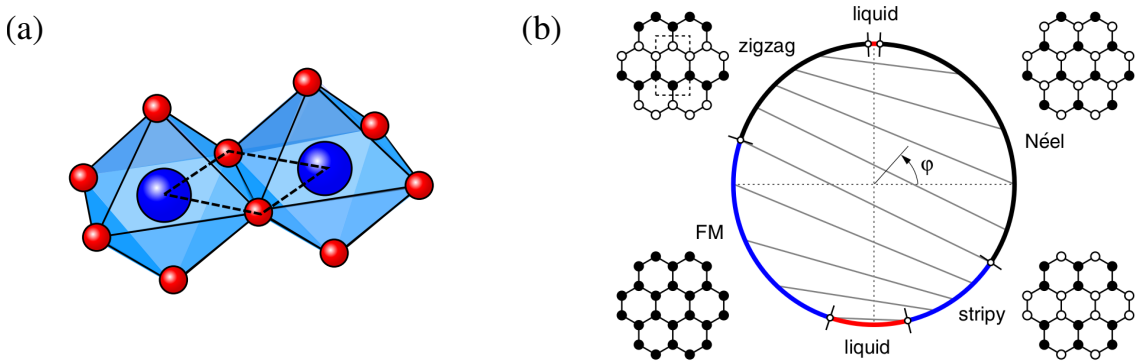

Figure 4 – (a) Geometry with edge-sharing octahedra which gives rise to spin-1/2 Kitaev interactions in Mott insulators. The large blue spheres represent the magnetic d^5 cations, whereas the smaller red spheres indicate nonmagnetic anions. Dashed lines mark two exchange paths between the transition elements which result in the destructive interference of the symmetric Heisenberg exchange. (b) Phase diagram of the Heisenberg-Kitaev model, Eq. (2.11), with $J = A\cos\varphi$ and $K = 2A\sin\varphi$. By varying φ, one finds that, in addition to the KSL, the model presents four ordered phases, identified as Néel, zigzag, FM and stripy. Black and white dots represent spins up and down, whereas the chords in the circle connect pairs of values of φ that are connected by the Klein transformation.

Source: (a) TREBST.[14] (b) CHALOUPKA; JACKELI; KHALIULLIN.[3]

which Ir^{4+} ions form stacked planes of honeycomb lattices, as the first material candidates to host Kitaev interactions.

2.2.2 The Heisenberg-Kitaev model

In the following years, Chaloupka, Jackeli and Khaliullin improved the analysis described in the previous subsection by considering additional exchange processes.[3,18] They argued that a minimal model to describe Kitaev materials should include a combination of nearest-neighbor Heisenberg and Kitaev exchanges, which can, in principle, take on different signs and relative magnitudes. Put together, these terms constitute the nearest-neighbor Heisenberg-Kitaev (HK) model:

$$\mathcal{H}_{\mathrm{HK}} = J\sum_{\langle ij\rangle}\mathbf{S}_i\cdot\mathbf{S}_j + K\sum_{\langle ij\rangle_\gamma} S_i^\gamma S_j^\gamma. \tag{2.11}$$

Differently from Hamiltonians comprised of pure Heisenberg interactions, the highest symmetry of $\mathcal{H}_{\mathrm{HK}}$ is of discrete rather than continuous nature. As the Kitaev interaction breaks SU(2) spin symmetry, it leaves the system with a residual C_3^* symmetry, which combines a $2\pi/3$ rotation around an arbitrary site of the lattice with a $2\pi/3$ rotation around the [111] axis in spin space. One can check that Eq. (2.11) is indeed invariant under these operations by noting that they correspond, respectively, to cyclic permutations in the three bonds of the lattice, $\{x, y, z\} \to \{y, z, x\}$, and in the spin components, $\{S_i^x, S_i^y, S_i^z\} \to \{S_i^y, S_i^z, S_i^x\}$.

Once the physical mechanism that generates the Kitaev exchange in real materials was understood, it became necessary to study the physical predictions of Eq. (2.11). Several methods were applied to this end, including exact diagonalization (ED),[3,18] tensor network approaches,[81] cluster mean-field theory,[82] and infinite density matrix renormalization group (iDMRG).[83] Despite differences with respect to the precise locations of the phase boundaries, all of these techniques lead to qualitatively equivalent phase diagrams. Fig. 4(b), in particular, shows the result of a 24-site ED simulation,[3] for which the exchange couplings are conveniently reparametrized as $J = A\cos\varphi$ and $K = 2A\sin\varphi$. There, we note that extended spin liquid phases appear around the Kitaev points, $\varphi = \pi/2$ and $\varphi = 3\pi/2$, whereas the usual FM and Néel orders arise near the Heisenberg limits $\varphi = \pi$ and $\varphi = 0$, respectively. However, the calculations revealed two other magnetically ordered phases, named stripy and zigzag. Although their existence might at first seem uncanny, it can be readily understood by means of the Klein transformation, which we describe in the next subsection.

2.2.3 The Klein transformation

In order to implement the Klein transformation, we begin by dividing the lattice into four sublattices which, as illustrated in Fig. 5, are themselves honeycomb lattices[§]; each of them has links twice as large as the original and is identified by one of the indices E, X, Y or Z. After accordingly assigning a label $a_i \in \{\mathrm{E}, \mathrm{X}, \mathrm{Y}, \mathrm{Z}\}$ to every site i, we can then apply a unitary transformation given by[3,16,84]

$$\mathbf{S}_i \longrightarrow \tilde{\mathbf{S}}_i = g\left[a_i\right]\mathbf{S}_i\,, \quad \text{with} \quad g\left[a_i\right] := \begin{cases} g\left[\mathrm{E}\right] = \mathrm{diag}\left(1,1,1\right) & \text{if } i \in \mathrm{E} \\ g\left[\mathrm{X}\right] = \mathrm{diag}\left(1,-1,-1\right) & \text{if } i \in \mathrm{X} \\ g\left[\mathrm{Y}\right] = \mathrm{diag}\left(-1,1,-1\right) & \text{if } i \in \mathrm{Y} \\ g\left[\mathrm{Z}\right] = \mathrm{diag}\left(-1,-1,1\right) & \text{if } i \in \mathrm{Z} \end{cases} \tag{2.12}$$

The spins in sublattice E are thus unaffected, whereas those belonging to the sublattices connected to E through a γ-bond undergo π rotations around S^γ axis of the Bloch sphere.

The reason why Eq. (2.12) is called a Klein transformation is that the matrices $\{g\left[\mathrm{E}\right], g\left[\mathrm{X}\right], g\left[\mathrm{Y}\right], g\left[\mathrm{Z}\right]\}$ form a representation of the Klein four-group, as one can see by checking that they reproduce the multiplication rules shown in Table 1. Further, the group structure establishes a formal correspondence between the sublattice labels $\{\mathrm{E}, \mathrm{X}, \mathrm{Y}, \mathrm{Z}\}$ and the bonds labels $\{x, y, z\}$: For any two nearest neighbor sites, i and j, separated by a γ-bond, the product $g\left[a_i\right] g\left[a_j\right]$ gives $g\left[\gamma\right]$[¶]. Indeed, consider the case where $a_i = \mathrm{X}$ and

§ Although frequently omitted, this is an important remark, since a division of the honeycomb lattice into four rectangular sublattices is also possible, but inappropriate for the Klein transformation.

¶ For convenience, we have committed a slight abuse of notation here. $g\left[x\right]$ is to be understood as $g\left[\mathrm{X}\right]$ and so on.

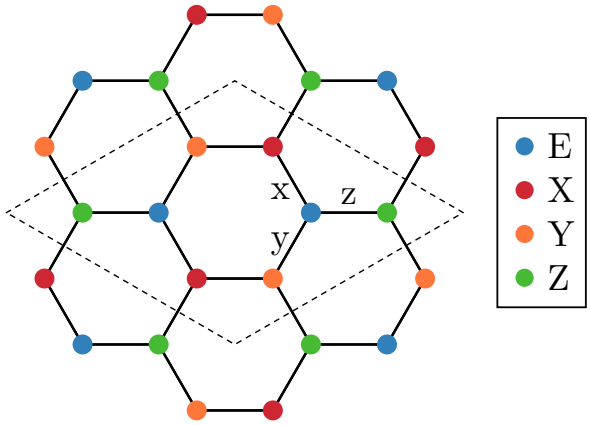

Figure 5 – Structure of the Klein transformation, Eq. (2.12), in real space. The honeycomb lattice is divided in four honeycomb sublattices distinguished by the labels E, X, Y and Z. Since the sublattices are not Bravais lattice, the unit cell of the transformation, which is delimited in dashed lines, includes eight instead of four sites.

Source: By the author.

$a_j = \mathrm{Z}$ as an example. Since the sublattices X and Z are connected by a y-bond (see Fig. 5), the result $g\,[X]\,g\,[Z] = g\,[Y]$ is consistent with our former statement.

Let us now apply the transformation to $\mathcal{H}_{\mathrm{HK}}$. The result is most easily obtained by analyzing the interaction $\mathcal{H}_{ij}^{(\gamma)}$ between two given sites, i and j, connected by a γ-bond:

$$\begin{aligned}\mathcal{H}_{ij}^{(\gamma)} &= J \sum_{\alpha=x,y,z} S_i^\alpha S_j^\alpha + K S_i^\gamma S_j^\gamma \\ &\longrightarrow J \sum_\alpha g\,[a_i]_{\alpha\alpha}\, g\,[a_j]_{\alpha\alpha}\, \tilde{S}_i^\alpha \tilde{S}_j^\alpha + K\; g\,[a_i]_{\gamma\gamma}\, g\,[a_j]_{\gamma\gamma}\, \tilde{S}_i^\gamma \tilde{S}_j^\gamma \\ &= J \sum_\alpha g\,[\gamma]_{\alpha\alpha}\, \tilde{S}_i^\alpha \tilde{S}_j^\alpha + K g\,[\gamma]_{\gamma\gamma}\, \tilde{S}_i^\gamma \tilde{S}_j^\gamma = -J \sum_\alpha \tilde{S}_i^\alpha \tilde{S}_j^\alpha + (2J+K)\, \tilde{S}_i^\gamma \tilde{S}_j^\gamma . \end{aligned} \tag{2.13}$$

We therefore conclude that the Klein transformation maps the HK Hamiltonian onto itself. The only difference between the original Hamiltonian, Eq. (2.11), and its transformed version comes from a renormalization of the exchange couplings, $\{J, K\} \to \left\{\tilde{J}, \tilde{K}\right\}$, which one can read off Eq. (2.13) as being

$$\begin{cases} \tilde{J} = -J \\ \tilde{K} = 2J + K \end{cases} \quad \Longrightarrow \quad \begin{cases} \cos\tilde{\varphi} = -\cos\varphi \\ \sin\tilde{\varphi} = \cos\varphi + \sin\varphi \end{cases} \tag{2.14}$$

With this, we have established a duality between the solutions of the original and transformed HK Hamiltonians, $\mathcal{H}_{\mathrm{HK}}$ and $\tilde{\mathcal{H}}_{\mathrm{HK}}$. Especially remarkable are the cases where $\tilde{K} = 0$, since they allow us to extract information about the ground state of $\mathcal{H}_{\mathrm{HK}}$ by inspecting the Heisenberg limits of $\tilde{\mathcal{H}}_{\mathrm{HK}}$. In terms of the parametrization employed in Fig. 4(b), these points of hidden SU(2) symmetry correspond to $\varphi = -\pi/4$ $\left(\tilde{J} < 0\right)$ and $\varphi = 3\pi/4$ $\left(\tilde{J} > 0\right)$. In the former case, we know that the exact ground states of $\tilde{\mathcal{H}}_{\mathrm{HK}}$ are

Table 1 – Multiplication table of the Klein four-group.

×	E	X	Y	Z
E	E	X	Y	Z
X	X	E	Z	Y
Y	Y	Z	E	X
Z	Z	Y	X	E

Source: By the author.

ferromagnetic (FM) configurations of spins aligned along arbitrary directions of the $\tilde{\mathbf{S}}$ Bloch sphere. By applying the inverse Klein transformation, we thus obtain a continuous ground-state manifold of $\mathcal{H}_{\mathrm{HK}}$ at $\varphi = -\pi/4$. Analogously, when $\varphi = 3\pi/4$, the inverse Klein transformation maps the different antiferromagnetic (AF) Néel configurations onto a continuous manifold of degenerate states. However, in contrast to the previous case, these are not fluctuation-free, for the Néel state is not an eigenstate of the Heisenberg Hamiltonian.

The origin of the stripy and zigzag phases can be understood as a direct consequence of this duality. By applying the (inverse) Klein transformation to a FM state along the z axis, one finds that the spins in the X and Y sublattices are flipped, whereas those in the E and Z sublattices remain intact. The result is therefore the collinear stripy phase illustrated in Fig. 4(b), with stripes of similar spins running parallel to the z-bonds. Due to the C_3^* symmetry of the Hamiltonian, two different patterns of this same phase are obtained by transforming FM states along the x- a y-axes. The resulting configurations have stripes of similar spins running parallel to the x- and y-bonds, respectively. Similarly, the Klein transformation maps Néel states oriented along the x-, y- and z- axes to different patterns of the zigzag phase shown in Fig. 4(b). Each of these patterns exhibits chains of similar spins running perpendicularly to one of the three bonds.

While the stripy and zigzag states are collinear, the manifold generated by the Klein transformation at the *Klein points* $\varphi = -\pi/4$ and $\varphi = 3\pi/4$ also includes a multitude of noncoplanar and noncollinear spin states, which are obtained by transforming FM or Néel configurations aligned with any direction other than the x-, y- or z-axes. Typically, these exotic states exhibit multiple Bragg peaks in their first Brillouin zone and, for this reason, are dubbed multi-$\mathbf{Q}$ states. They do not appear in the phase diagram of Fig. 4(b) because quantum fluctuations induced by the smallest deviation from the Klein points select the stripy and zigzag orders. We will, nonetheless, encounter two particular examples of such of multi-$\mathbf{Q}$ phases in Chapter 4.

Finally, we mention that the Klein duality is generally spoiled upon the inclusion of different types of spin interactions. A few exceptions do apply,[84] however, including the case

where the Hamiltonian includes a Heisenberg interaction between third nearest-neighbors, as these belong to the same sublattice (see Fig. 5). For future reference, we also note that a uniform magnetic field is mapped onto a staggered magnetic field by the Klein transformation, so that the duality is generally broken as well.

2.2.4 Beyond the Heisenberg-Kitaev model

Experimental studies conducted up to date show that, while a few materials display appreciable or even dominant Kitaev interactions, none are known to be satisfactorily described by the pure spin-1/2 nearest-neighbor HK Hamiltonian, Eq. (2.11). The present consensus is that this model is overly simplistic, for it neglects aspects such as possible modifications to the crystal field due to irregular octahedral cages and the spatial extension of d orbitals, which is expected to generate relevant interactions beyond nearest-neighbor pseudospins.[19]

More realistic spin models thus include additional interactions which are consistent with the symmetry of the crystal. In particular, the threefold rotational symmetry of the honeycomb lattice allows one to assign a label $\gamma \in \{x, y, z\}$ to the bond connecting any two sites, i and j, of the same honeycomb layer, even if they are not nearest neighbors. Assuming that this bond exhibits local C_{2h} symmetry, the generic interaction between the sites i and j reads[19,85]

$$\mathcal{H}_{ij}^{(\gamma)} = J_{ij}\mathbf{S}_i \cdot \mathbf{S}_j + K_{ij}S_i^\gamma S_j^\gamma + \Gamma_{ij}\left(S_i^\alpha S_j^\beta + S_i^\beta S_j^\alpha\right) + \Gamma'_{ij}\left(S_i^\gamma S_j^\alpha + S_i^\gamma S_j^\beta + S_i^\alpha S_j^\gamma + S_i^\beta S_j^\gamma\right), \tag{2.15}$$

where $\{\alpha, \beta, \gamma\}$ is a permutation of $\{x, y, z\}$. If trigonal distortions can be neglected, the Γ'_{ij} exchanges are expected to be small,[86] and the couplings J_{ij}, K_{ij} and Γ_{ij} have the same magnitude along bonds related by 120° lattice rotations.[60] Therefore, a realistic model restricted to nearest-neighbor interactions should include at least isotropic J, K and Γ couplings.

Although shall address the matter of modeling a real material in Chapter 5, our primary interest in this dissertation is to study the response of magnetically ordered phases to an external magnetic field. This will be quantified by means of a standard Zeeman term:

$$\mathcal{H}_{\mathrm{Z}} = -g\mu_{\mathrm{B}}\mu_0\,\mathbf{H} \cdot \sum_i \mathbf{S}_i. \tag{2.16}$$

Here, μ_{B} is the Bohr magneton, g is an isotropic (or partially isotropic) g-factor and $g\mu_{\mathrm{B}}\mathbf{S}$ corresponds to the effective magnetic moment of the $J_{\mathrm{eff}} = 1/2$ states in the crystal.

2.2.5 α-$RuCl_3$: A promising candidate

Currently, much of the attention in the field of Kitaev magnetism has been focused on the quantum magnet α-$RuCl_3$ ($D = Ru^{3+}$ and $A = Cl^-$). This compound has a

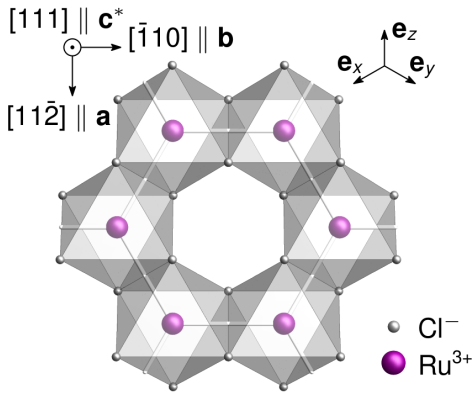

Figure 6 – Crystal structure of one layer of the Kitaev material α-$RuCl_3$. The Ru^{3+} ions form magnetic moments of and sit on the vertices of a honeycomb lattice. Each Ru^{3+} ion is surrounded by a octahedral cage of nonmagnetic Cl^- ions.

Source: JANSSEN; ANDRADE; VOJTA.[87]

layered structure of edge-sharing $RuCl_6$ octahedra in which the magnetic Ru^{3+} ions form honeycomb planes, as illustrated in Fig. 6. If trigonal distortions can be neglected, there are consequently three inequivalent directions, commonly denoted as a, b and c^*. The first two are in-plane directions chosen to be perpendicular and parallel to Ru–Ru bonds, respectively, whereas the last is normal to the honeycomb planes. In the cubic basis formed by the vectors $\mathbf{e_x}$, $\mathbf{e_y}$ and $\mathbf{e_z}$ which connect the Ru^{3+} cations to their nonmagnetic Cl^- neighbors, we have $\mathbf{a} \parallel [112]$, $\mathbf{b} \parallel \left[\bar{1}10\right]$ and $\mathbf{c}^* \parallel [111]$.

In the absence of a magnetic field and at temperatures below $T_N \sim 7$ K, α-$RuCl_3$ exhibits an in-plane zigzag order,[5,31] which is already an indication that Kitaev interactions play an important role in the material. The most interesting properties of α-$RuCl_3$, however, emerge in the presence of an external magnetic field. As depicted in Fig. 7(a), a field with a moderate in-plane component suppresses the zigzag order and drives the system into a paramagnetic state. While the precise nature of this state has been subject of recent debate,[36,42,44] several experiments suggest the existence of a quantum spin-liquid regime at intermediate fields.[41,44,46–51] Most prominently, the measurement of an approximately half-quantized thermal Hall conductivity,[44,51] see Fig. 7(b), has been associated with the same chiral Majorana edge modes described in Sec. 2.1.2, which are characteristic of the gapped KSL.[53,88]

In Chapter 5, we shall take up the task of modeling the magnetic properties of α-$RuCl_3$. A basic constraint on the generic interactions displayed in Eq. (2.15) is that they must generate a zigzag ground-state at zero field. In principle, this requirement can be fulfilled in three distinct scenarios:[87]

1. The first option is obtained within the pure nearest-neighbor HK model and combines a strong AF Kitaev term, $K > 0$, with a weak FM Heisenberg interaction, $J < 0$, as

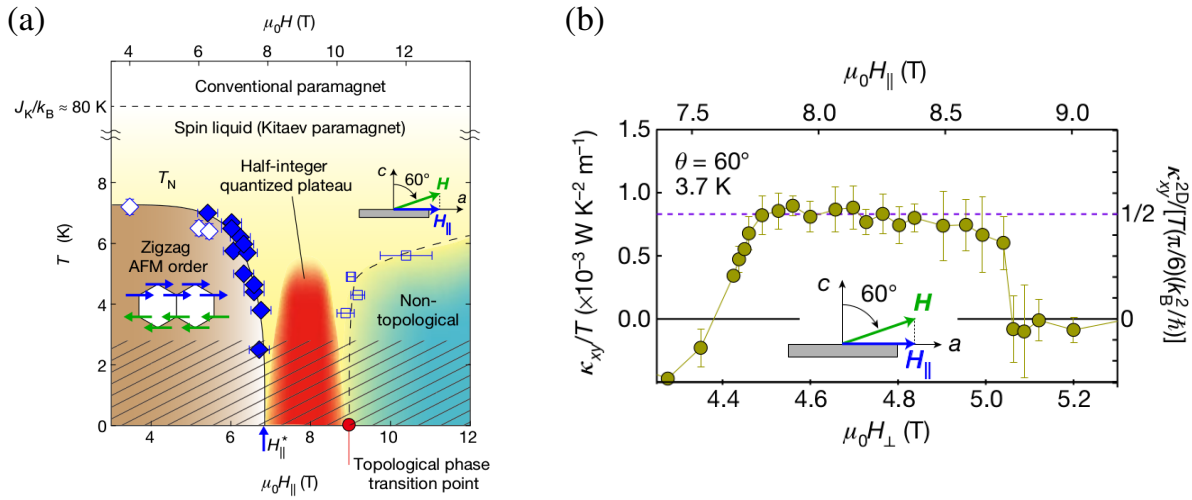

Figure 7 – (a) Proposed temperature-field phase diagram for α-$RuCl_3$, featuring a possible spin liquid phase at low temperatures and intermediate magnetic fields. The upper horizontal axis represents the magnitude of a magnetic field applied in a direction 60° away from the c^* axis, whereas the bottom horizontal axis gives the magnitude of the projection onto the in-plane a axis. (b) Experimental results showing an approximately half-quantized thermal Hall conductivity in a sample of α-$RuCl_3$ in a magnetic field.

Source: KASAHARA *et al.*[44]

expressed in the phase diagram of Fig. 4(a).

2. The second scenario requires a FM Kitaev interaction, $K < 0$, in addition to a sizeable $\Gamma > 0$ and/or $\Gamma' < 0$.

3. The final possibility also entails a FM Kitaev coupling, $K < 0$, but demands an appreciable AF third-nearest-neighbor Heisenberg interaction, $J_3 > 0$.

However, the majority of recent studies invested in determining parameter sets for spin-1/2 Kitaev materials have converged to the conclusion that the Kitaev coupling is *ferromagnetic*.[89] Consequently, a description of the magnetic properties of α-$RuCl_3$ in terms the pure HK model is insufficient. Here, we employ a minimal model which combines scenarios 2 and 3 by including nearest-neighbor Heisenberg J_1, Kitaev K_1, and off-diagonal Γ_1 interactions as well as a third-nearest-neighbor Heisenberg J_3 coupling:[89]

$$\mathcal{H}_{\mathrm{JK\Gamma J_3}} = \sum_{\langle ij \rangle} \left[J_1 \mathbf{S}_i \cdot \mathbf{S}_j + K_1 S_i^{\gamma} S_j^{\gamma} + \Gamma_1 \left(S_i^{\alpha} S_j^{\beta} + S_i^{\beta} S_j^{\alpha} \right) \right] + \sum_{\langle\langle\langle ij \rangle\rangle\rangle} J_3 \mathbf{S}_i \cdot \mathbf{S}_j \,, \tag{2.17}$$

where the x, y and z spin quantization axes point along the $\mathbf{e_x}$, $\mathbf{e_y}$ and $\mathbf{e_z}$ cubic axes of the $RuCl_6$ octahedra. As a two-dimensional model, Eq. (2.17) contains the implicit assumption that van der Waals interactions between different honeycomb planes are negligible. The values of the exchange couplings can be estimated from *ab initio* calculations;[89] however, previous studies[8,38,90] have found better agreement with experimental data by using a

slightly adapted parameter set:

$$(J_1, K_1, \Gamma_1, J_3) = A\,(-0.1, -1.0, +0.5, +0.1)\,, \tag{2.18}$$

with A being an adjustable global energy scale of the order of a few meV.

2.2.6 Higher-spin Kitaev models and materials

Recently, there have also been proposals of material candidates to host higher-spin analogs of the Kitaev interaction. The interest in these classes of compounds is fueled by the growing theoretical evidence that they may offer different routes to realize quantum spin liquids, and by an attempt to uncover novel magnetic phenomena resulting from strong spin-orbit coupling.

In this context, considerable effort has been devoted to the study of $S = 1$ Kitaev systems, which have been found to arise in materials with the same structure of edge-sharing octahedra depicted in Fig. 4(a).[22] However, the magnetic ions must be in a d^8 rather than a d^5 electronic configuration, such that each e_g orbital represented in Fig. 3 is half filled. If, in addition, the system presents strong Hund's coupling between the e_g electrons of the D cations and strong spin-orbit coupling for electrons occupying the p orbitals of the A anions, then it is expected to display dominant $S = 1$ Kitaev interactions.[22] Remarkably, such interactions are predicted to be *antiferromagnetic*, in contrast to the case of $S = 1/2$. This particular feature has been the reason for excitement, given the growing evidence that the gapless spin-liquid phase which a magnetic field induces in the AF $S = 1/2$ Kitaev model is also present for spin-1 Kitaev interactions[91–93]

So far, the most prominent candidate spin-1 Kitaev materials have been the layered antimonates $X_3Ni_2SbO_6$ ($X = \mathrm{Li}, \mathrm{Na}$).[57] Similarly to α-$RuCl_3$, they exhibit a zigzag ground state at low temperatures and zero magnetic field.[57,94] Nevertheless, they might be closer to a condition of dominant Kitaev interactions, as specific heat measurements show an entropy plateau of $1/2 \ln 3$ well above the Néel temperature,[57] in resemblance to the behavior of a pure $S = 1$ Kitaev model.[95,96] Furthermore, the antimonates have drawn attention for undergoing metamagnetic transitions towards field-induced intermediate ordered phases. Although the lower transition was initially interpreted in terms of a spin-flop mechanism,[57] recent magnetostriction experiments on $Na_3Ni_2SbO_6$ suggest a picture of an anisotropy-governed competition between different AF phases.[58]

In parallel, different Cr-based monolayers have been proposed as candidate $S = 3/2$ Kitaev systems.[22,56,97] They are generated by a microscopic mechanism similar to their spin-1 analogs, except for the fact that the electronic distribution of the magnetic Cr^{3+} ions ends in $3d^3$, so that the t_{2g} triplet is only partially filled. These compounds show a FM ground state,[98,99] but may potentially be driven to other magnetic or paramagnetic states by epitaxial strain.[97]

3 FUNDAMENTALS OF LINEAR SPIN-WAVE THEORY

In this chapter, we present a general framework to study the effects of quantum fluctuations on an arbitrary magnetic phase. This entails the fundamentals of spin-wave theory, a tool which we apply in Chapters 4 and 5. Here, we will be primarily concerned in describing the so-called linear spin-wave regime, although we shall later deal with improved levels of approximation.

3.1 Setting up the spin-wave Hamiltonian

The starting point of a spin-wave calculation is to take the classical limit of the Hamiltonian of interest by treating spins as commuting vectors, and thus determine the classical ground state of the system at given values of the magnetic coupling constants. While this is usually straightforward in unfrustrated spin systems, more refined minimization techniques, such as the Luttinger-Tisza method[100] or a classical Monte Carlo simulation, are often required when frustration is present. After obtaining these preliminary results, one must parametrize the classical ground state in the laboratory reference frame, i.e. in the spin coordinate system that defines the original form of the Hamiltonian. On general grounds, each magnetic phase is characterized by a magnetic unit cell composed of N_s spins, so that a particular parametrization specifies a total of N_s pairs of angles. By labeling the different sites in the magnetic unit cell with the subindex $\mu \in \{1, \ldots, N_\mathrm{s}\}$, we then attribute to each spin an azimuthal and a polar angle, denoted here by ϕ_μ and θ_μ, respectively.

Next, we rotate the spin coordinate system so that the transformed Hamiltonian bears a ferromagnetic ground state. This involves a set of N_s rotations which map the laboratory $\{\hat{\mathbf{x}}, \hat{\mathbf{y}}, \hat{\mathbf{z}}\}$ basis onto local $\{\hat{\mathbf{e}}_{\mu 1}, \hat{\mathbf{e}}_{\mu 2}, \hat{\mathbf{e}}_{\mu 3}\}$ bases which have $\hat{\mathbf{e}}_{\mu 3}$ pointing along the classical spin direction in magnetic sublattice μ. Here, we represent such rotations as

$$\begin{pmatrix} S^x_{i\mu} \\ S^y_{i\mu} \\ S^z_{i\mu} \end{pmatrix} = \mathbb{R}\left(\phi_\mu, \theta_\mu\right) \begin{pmatrix} S^1_{i\mu} \\ S^2_{i\mu} \\ S^3_{i\mu} \end{pmatrix}, \tag{3.1}$$

where i runs from 1 to N_c, the total number of magnetic unit cells in the lattice. When dealing with noncoplanar states induced by a magnetic field $\mathbf{h}$, it is useful to carry out this procedure in three steps represented by the decomposition

$$\mathbb{R}\left(\phi_\mu, \theta_\mu\right) = \mathbb{R}_1^\mathrm{T} \mathbb{R}_2^\mathrm{T}\left(\phi_\mu\right) \mathbb{R}_3^\mathrm{T}\left(\theta_\mu\right). \tag{3.2}$$

The matrix $\mathbb{R}_1$ consists of a global rotation of the original $\{\hat{\mathbf{x}}, \hat{\mathbf{y}}, \hat{\mathbf{z}}\}$ basis into a new reference frame $\left\{\hat{\mathbf{e}}^0_1, \hat{\mathbf{e}}^0_2, \hat{\mathbf{e}}^0_3\right\}$, which is defined so that the unit vector $\hat{\mathbf{e}}^0_3 \parallel \mathbf{h}$. The two

remaining unit vectors may be chosen somewhat arbitrarily within the plane perpendicular to $\hat{\mathbf{e}}_3^0$.* The second step is encoded in the matrix $\mathbb{R}_2(\phi_\mu)$, which rotates the $\left\{\hat{\mathbf{e}}_1^0, \hat{\mathbf{e}}_2^0, \hat{\mathbf{e}}_3^0\right\}$ about the $\hat{\mathbf{e}}_3^0$ axis to give $\left\{\hat{\mathbf{e}}_{1\mu}^0, \hat{\mathbf{e}}_{2\mu}^0, \hat{\mathbf{e}}_{3\mu}^0\right\}$. The rotation angle ϕ_μ is selected in such a way that the orientation of the classical spin on the sublattice μ lies on the plane generated by the $\hat{\mathbf{e}}_{1\mu}^0$ and $\hat{\mathbf{e}}_{3\mu}^0 \equiv \hat{\mathbf{e}}_3^0$ vectors. Finally, one maps $\left\{\hat{\mathbf{e}}_{1\mu}^0, \hat{\mathbf{e}}_{2\mu}^0, \hat{\mathbf{e}}_{3\mu}^0\right\}$ onto the target $\{\hat{\mathbf{e}}_{1\mu}, \hat{\mathbf{e}}_{2\mu}, \hat{\mathbf{e}}_{3\mu}\}$ basis by performing a rotation $\mathbb{R}_3(\theta_\mu)$ around $\hat{\mathbf{e}}_{2\mu}^0$.

Once the proper rotations are determined, we use Eq. (3.1) to rewrite the Hamiltonian in the new spin coordinate system and express the spin-S operators in terms of bosonic modes by means of the Holstein-Primakoff (HP) transformation[101,102]

$$\begin{cases} S_{i\mu}^3 = S - a_{i\mu}^\dagger a_{i\mu}, \\ S_{i\mu}^- = a_{i\mu}^\dagger \sqrt{2S - a_{i\mu}^\dagger a_{i\mu}} = \sqrt{2S}\left(a_{i\mu}^\dagger - \frac{a_{i\mu}^\dagger a_{i\mu}^\dagger a_{i\mu}}{4S} + \cdots\right), \\ S_{i\mu}^+ = \sqrt{2S - a_{i\mu}^\dagger a_{i\mu}}\; a_{i\mu} = \sqrt{2S}\left(a_{i\mu} - \frac{a_{i\mu}^\dagger a_{i\mu} a_{i\mu}}{4S} + \cdots\right), \end{cases} \tag{3.3}$$

where $a_{i\mu}^\dagger$ and $a_{i\mu}$ are creation and annihilation operators satisfying the commutation relations $\left[a_{i\mu}, a_{j\nu}^\dagger\right] = \delta_{ij}\delta_{\mu\nu}$ and $[a_{i\mu}, a_{j\nu}] = \left[a_{i\mu}^\dagger, a_{j\nu}^\dagger\right] = 0$. By expanding the spin ladder operators in powers of $a_{i\mu}^\dagger a_{i\mu}/2S$, one can then rewrite the Hamiltonian as a power series in $1/\sqrt{S}$,

$$\mathcal{H} = \sum_{n=0}^{\infty} S^{2-\frac{n}{2}} \mathcal{H}_n \,. \tag{3.4}$$

Each term in Eq. (3.4) is labeled according to its order n in bosonic operators.

3.2 Linear spin-wave theory

In the linear spin-wave (LSW) regime, interactions between magnons are neglected, so that only the terms up to order $n = 2$ in Eq. (3.4) are retained. This approximation is therefore expected to be reliable when $\left\langle a_{i\mu}^\dagger a_{i\mu}\right\rangle \ll 2S$, i.e., when the fluctuations around the classical reference state are small to the spin size. Because the expansion is performed around a configuration that minimizes $\mathcal{H}_0$, the linear term $\mathcal{H}_1$ vanishes, and we end up with a simple quadratic Hamiltonian.

After performing a Fourier transform and choosing, for convenience, a first Brillouin zone (BZ) which is symmetric about the origin of reciprocal space, we can write the LSW Hamiltonian as[103]

$$\mathcal{H}_{\mathrm{LSW}} = \sum_{n=0}^{2} S^{2-\frac{n}{2}} \mathcal{H}_n = S^2 E_{\mathrm{gs},0} + \frac{S}{2}\sum_{\mathbf{k}} \left(\alpha_{\mathbf{k}}^\dagger \mathbb{M}_{\mathbf{k}} \alpha_{\mathbf{k}} - \mathrm{Tr}\mathbb{A}_{\mathbf{k}}\right). \tag{3.5}$$

Here, $\alpha_{\mathbf{k}} = \left(a_{\mathbf{k}1}, \ldots, a_{\mathbf{k}N_\mathrm{s}}, a_{-\mathbf{k}1}^\dagger, \ldots, a_{-\mathbf{k}N_\mathrm{s}}^\dagger\right)^\mathrm{T}$ and $S^2 E_{\mathrm{gs},0} \equiv S^2 \mathcal{H}_0$ is the classical ground-state energy. In these terms, one can express the bosonic commutation relations between

* Note that this is the only step required when performing the expansion around a fully polarized state.

the $\left\{a_{\mathbf{k}\mu}, a^{\dagger}_{\mathbf{k}\mu}\right\}$ operators as

$$\left[\alpha_{\mathbf{k}\mu}, \alpha^{\dagger}_{\mathbf{q}\nu}\right] = \delta_{\mathbf{kq}}\sigma_{3,\mu\nu} \tag{3.6}$$

with

$$\sigma_3 := \begin{pmatrix} \mathbb{1}_{N_\mathrm{s}} & 0_{N_\mathrm{s}} \\ 0_{N_\mathrm{s}} & -\mathbb{1}_{N_\mathrm{s}} \end{pmatrix}. \tag{3.7}$$

being a $2N_\mathrm{s}\times 2N_\mathrm{s}$ generalization of the diagonalization Pauli matrix. $\mathbb{M}_{\mathbf{k}}$ is also a $2N_\mathrm{s}\times 2N_\mathrm{s}$ matrix which can generically be written in terms of two $N_\mathrm{s}\times N_\mathrm{s}$ submatrices, $\mathbb{A}_{\mathbf{k}}$ and $\mathbb{B}_{\mathbf{k}}$, as

$$\mathbb{M}_{\mathbf{k}} = \begin{pmatrix} \mathbb{A}_{\mathbf{k}} & \mathbb{B}_{\mathbf{k}} \\ \mathbb{B}^{\dagger}_{\mathbf{k}} & \mathbb{A}^{\mathrm{T}}_{-\mathbf{k}} \end{pmatrix}. \tag{3.8}$$

Since the Hamiltonian is Hermitian, one immediately sees that $\mathbb{A}_{\mathbf{k}} = \mathbb{A}^{\dagger}_{\mathbf{k}}$. On the other hand, the requirement that the first BZ be symmetric with respect to the origin of reciprocal space implies that

$$\begin{aligned}
\mathcal{H}_2 &= \frac{1}{2}\sum_{\mathbf{k}}\left[a^{\dagger}_{\mathbf{k}\mu}\left(\mathbb{A}_{\mathbf{k},\mu\nu}a_{\mathbf{k}\nu} + \mathbb{B}_{\mathbf{k},\mu\nu}a^{\dagger}_{-\mathbf{k}\nu}\right) + a_{-\mathbf{k}\mu}\left(\mathbb{B}^{*}_{\mathbf{k},\nu\mu}a_{\mathbf{k}\nu} + \mathbb{A}_{-\mathbf{k},\nu\mu}a^{\dagger}_{-\mathbf{k}\nu}\right) - \mathrm{Tr}\mathbb{A}_{\mathbf{k}}\right] \\
&= \frac{1}{2}\sum_{\mathbf{k}}\left[a^{\dagger}_{\mathbf{k}\mu}\left(\mathbb{A}_{\mathbf{k},\mu\nu}a_{\mathbf{k}\nu} + \mathbb{B}_{-\mathbf{k},\nu\mu}a^{\dagger}_{-\mathbf{k}\nu}\right) + a_{-\mathbf{k}\mu}\left(\mathbb{B}^{*}_{-\mathbf{k},\mu\nu}a_{\mathbf{k}\nu} + \mathbb{A}_{-\mathbf{k},\nu\mu}a^{\dagger}_{-\mathbf{k}\nu}\right) - \mathrm{Tr}\mathbb{A}_{\mathbf{k}}\right] \\
&= \frac{1}{2}\sum_{\mathbf{k}}\left[\alpha^{\dagger}_{\mathbf{k}}\begin{pmatrix} \mathbb{A}_{\mathbf{k}} & \mathbb{B}^{\mathrm{T}}_{-\mathbf{k}} \\ \mathbb{B}^{*}_{-\mathbf{k}} & \mathbb{A}^{\mathrm{T}}_{-\mathbf{k}} \end{pmatrix}\alpha_{\mathbf{k}} - \mathrm{Tr}\mathbb{A}_{\mathbf{k}}\right],
\end{aligned} \tag{3.9}$$

where the equality between the first and second lines follows from simultaneously inverting $\mathbf{k}$ and exchanging the indices μ and ν in the terms involving the $\mathbb{B}_{\mathbf{k}}$ matrix. A direct comparison between Eq. (3.9) and its original form, Eqs. (3.5) and (3.8), then shows that $\mathbb{B}_{\mathbf{k}} = \mathbb{B}^{\mathrm{T}}_{-\mathbf{k}}$. Therefore, given the matrix

$$\sigma_1 := \begin{pmatrix} 0_{N_\mathrm{s}} & \mathbb{1}_{N_\mathrm{s}} \\ \mathbb{1}_{N_\mathrm{s}} & 0_{N_\mathrm{s}} \end{pmatrix}, \tag{3.10}$$

we conclude that $\mathbb{M}_{\mathbf{k}}$ is such that

$$\sigma_1\mathbb{M}_{\mathbf{k}}\sigma_1 = \begin{pmatrix} \mathbb{A}^{\mathrm{T}}_{-\mathbf{k}} & \mathbb{B}^{\dagger}_{\mathbf{k}} \\ \mathbb{B}_{\mathbf{k}} & \mathbb{A}_{\mathbf{k}} \end{pmatrix} = \begin{pmatrix} \mathbb{A}^{*}_{-\mathbf{k}} & \mathbb{B}^{*}_{-\mathbf{k}} \\ \mathbb{B}^{\mathrm{T}}_{-\mathbf{k}} & \mathbb{A}_{\mathbf{k}} \end{pmatrix} = \mathbb{M}^{*}_{-\mathbf{k}}. \tag{3.11}$$

3.2.1 Diagonalization of quadratic bosonic Hamiltonians in reciprocal space

Once the full quadratic Hamiltonian, Eq. (3.9), is determined, we are left with the task of diagonalizing it. To this end, consider the homogeneous transformation

$$\beta_{\mathbf{k}} = \mathbb{T}_{\mathbf{k}}\alpha_{\mathbf{k}}, \qquad \text{with} \qquad \beta_{\mathbf{k}} = \left(b_{\mathbf{k}1}, \ldots, b_{\mathbf{k}N_\mathrm{s}}, b^{\dagger}_{-\mathbf{k}1}, \ldots, b^{\dagger}_{-\mathbf{k}N_\mathrm{s}}\right)^{\mathrm{T}}. \tag{3.12}$$

By demanding that

$$\sigma_1\beta_{-\mathbf{k}} = \left(b^{\dagger}_{\mathbf{k}1}, \ldots, b^{\dagger}_{\mathbf{k}N_\mathrm{s}}, b_{-\mathbf{k}1}, \ldots, b_{-\mathbf{k}N_\mathrm{s}}\right)^{\mathrm{T}} \overset{!}{=} \left(\beta^{\dagger}_{\mathbf{k}}\right)^{\mathrm{T}}, \tag{3.13}$$

one can verify that the most general form for $\mathbb{T}_{\mathbf{k}}$ is

$$\mathbb{T}_{\mathbf{k}} = \begin{pmatrix} \mathbb{X}_{\mathbf{k}}^{*} & -\mathbb{Y}_{\mathbf{k}}^{*} \\ -\mathbb{Y}_{-\mathbf{k}} & \mathbb{X}_{-\mathbf{k}} \end{pmatrix}, \tag{3.14}$$

with both $\mathbb{X}_{\mathbf{k}}$ and $\mathbb{Y}_{\mathbf{k}}$ being $N_{\mathrm{s}} \times N_{\mathrm{s}}$ matrices. Furthermore, we must require that the new operators $\left\{b_{\mathbf{k}\mu}, b_{\mathbf{k}\mu}^{\dagger}\right\}$ obey the bosonic algebra, i.e. that the transformation be canonical. Explicitly,

$$\left[\beta_{\mathbf{k}\mu}, \beta_{\mathbf{q}\nu}^{\dagger}\right] = \left[\mathbb{T}_{\mathbf{k},\mu\lambda}\alpha_{\mathbf{k}\lambda}, \mathbb{T}_{\mathbf{q},\nu\eta}^{*}\alpha_{\mathbf{q}\eta}^{\dagger}\right] = \delta_{\mathbf{kq}}\mathbb{T}_{\mathbf{k},\mu\lambda}\sigma_{3,\lambda\eta}\mathbb{T}_{\mathbf{q},\nu\eta}^{*} \overset{!}{=} \delta_{\mathbf{kq}}\sigma_{3,\mu\nu} \tag{3.15}$$

implies that

$$\mathbb{T}_{\mathbf{k}}^{-1} = \sigma_3\mathbb{T}_{\mathbf{k}}^{\dagger}\sigma_3 = \begin{pmatrix} \mathbb{X}_{\mathbf{k}}^{\mathrm{T}} & \mathbb{Y}_{-\mathbf{k}}^{\dagger} \\ \mathbb{Y}_{\mathbf{k}}^{\mathrm{T}} & \mathbb{X}_{-\mathbf{k}}^{\dagger} \end{pmatrix}. \tag{3.16}$$

In light of the pseudo-unitarity condition, Eq. (3.16), we rewrite the LSW Hamiltonian, Eq. (3.5), as

$$\mathcal{H}_{\mathrm{LSW}} = S^2 E_{\mathrm{gs},0} - \frac{S}{2}\sum_{\mathbf{k}} \mathrm{Tr}\mathbb{A}_{\mathbf{k}} + \frac{S}{2}\sum_{\mathbf{k}} \beta_{\mathbf{k}}^{\dagger}\,\sigma_3\,\mathbb{T}_{\mathbf{k}}\,\sigma_3\,\mathbb{M}_{\mathbf{k}}\,\mathbb{T}_{\mathbf{k}}^{-1}\beta_{\mathbf{k}}. \tag{3.17}$$

The problem of diagonalizing $\mathcal{H}_{\mathrm{LSW}}$ is thus solved by determining a matrix $\mathbb{T}_{\mathbf{k}}$ such that

$$\Omega_{\mathbf{k}} := \mathbb{T}_{\mathbf{k}}\,\sigma_3\,\mathbb{M}_{\mathbf{k}}\,\mathbb{T}_{\mathbf{k}}^{-1}. \tag{3.18}$$

is diagonal. A transformation which, in addition to satisfying Eqs. (3.12) and (3.16), renders Eq. (3.18) diagonal is called a *Bogoliubov transformation*.

Seeing that $\mathbb{T}_{\mathbf{k}}$ is related to the right eigenvectors of the non-Hermitian matrix $\sigma_3\mathbb{M}_{\mathbf{k}}$, we shall study the eigenvalue equation

$$\sigma_3\mathbb{M}_{\mathbf{k}}V_{\mathbf{k}\mu} = \epsilon_{\mathbf{k}\mu}V_{\mathbf{k}\mu}. \tag{3.19}$$

We will state and prove some of the main properties regarding the spectrum and eigenvectors of $\sigma_3\mathbb{M}_{\mathbf{k}}$.[103,104] These provide all the information one needs to calculate physical observables within LSWT.

Property 1. *If $V_{\boldsymbol{k}\mu}$ is a right eigenvector of $\sigma_3\mathbb{M}_{\boldsymbol{k}}$ that has $\epsilon_{\boldsymbol{k}\mu}$ as its eigenvalue, then*

$$\overline{V}_{\boldsymbol{k}\mu} := V_{\boldsymbol{k}\mu}^{\dagger}\sigma_3 \tag{3.20}$$

is a left eigenvector corresponding to the eigenvalue $\epsilon_{\boldsymbol{k}\mu}^{*}$.

Proof. By applying $\overline{V}_{\mathbf{k}\mu}$ to the left of $\sigma_3\mathbb{M}_{\mathbf{k}}$, one finds

$$\overline{V}_{\mathbf{k}\mu}\sigma_3\mathbb{M}_{\mathbf{k}} = V_{\mathbf{k}\mu}^{\dagger}\mathbb{M}_{\mathbf{k}} = \left(\mathbb{M}_{\mathbf{k}}^{\dagger}V_{\mathbf{k}\mu}\right)^{\dagger} = \left(\mathbb{M}_{\mathbf{k}}V_{\mathbf{k}\mu}\right)^{\dagger}, \tag{3.21}$$

Eq. (3.19) in turn gives $\mathbb{M}_{\mathbf{k}}V_{\mathbf{k}\mu} = \epsilon_{\mathbf{k}\mu}\sigma_3V_{\mathbf{k}\mu}$. When substituted into Eq. (3.21), this yields

$$\overline{V}_{\mathbf{k}\mu}\sigma_3\mathbb{M}_{\mathbf{k}} = \left(\epsilon_{\mathbf{k}\mu}\sigma_3V_{\mathbf{k}\mu}\right)^{\dagger} = \epsilon_{\mathbf{k}\mu}^{*}V_{\mathbf{k}\mu}^{\dagger}\sigma_3 \implies \overline{V}_{\mathbf{k}\mu}\sigma_3\mathbb{M}_{\mathbf{k}} = \epsilon_{\mathbf{k}\mu}^{*}\overline{V}_{\mathbf{k}\mu}. \tag{3.22}$$

■

Property 2. *If $V_{\boldsymbol{k}\mu}$ is a right eigenvector of $\sigma_3\mathbb{M}_{\boldsymbol{k}}$ that has $\epsilon_{\boldsymbol{k}\mu}$ as its eigenvalue, then*

$$W_{\boldsymbol{k}\mu} := \sigma_1 V^*_{-\boldsymbol{k}\mu} \tag{3.23}$$

is also a right eigenvector of $\sigma_3\mathbb{M}_{\boldsymbol{k}}$, corresponding, however, to the eigenvalue $-\epsilon^*_{-\boldsymbol{k}\mu}$.

Proof. First, note that, as higher-dimensional generalizations of Pauli matrices, σ_3 and σ_1 anticommute, $\{\sigma_1, \sigma_3\} = 0$. By using this property and Eq. (3.11), one can rewrite the complex conjugate of Eq. (3.19) as

$$\epsilon^*_{-\mathbf{k}\mu} V^*_{-\mathbf{k}\mu} = \sigma_3 \mathbb{M}^*_{-\mathbf{k}} V^*_{-\mathbf{k}\mu} = \sigma_3\sigma_1 \mathbb{M}_{\mathbf{k}} \sigma_1 V^*_{-\mathbf{k}\mu} = -\sigma_1\sigma_3 \mathbb{M}_{\mathbf{k}} \sigma_1 V^*_{-\mathbf{k}\mu}. \tag{3.24}$$

Multiplying both sides of Eq. (3.24) by σ_1 then leads us to

$$\sigma_3 \mathbb{M}_{\mathbf{k}} W_{\mathbf{k}\mu} = -\epsilon^*_{-\mathbf{k}\mu} W_{\mathbf{k}\mu}. \tag{3.25}$$

■

Property 3. *Let $V_{\boldsymbol{k}\mu}$ and $\overline{V}_{\boldsymbol{k}\nu} = V^\dagger_{\boldsymbol{k}\nu}\sigma_3$ be a right and a left eigenvector of $\sigma_3\mathbb{M}_{\boldsymbol{k}}$ with eigenvalues $\epsilon_{\boldsymbol{k}\mu}$ and $\epsilon^*_{\boldsymbol{k}\nu}$, respectively. If $\epsilon_{\boldsymbol{k}\mu} \neq \epsilon^*_{\boldsymbol{k}\nu}$, then $\overline{V}_{\boldsymbol{k}\nu}$ and $V_{\boldsymbol{k}\mu}$ are orthogonal, i.e. $\overline{V}_{\boldsymbol{k}\nu} V_{\boldsymbol{k}\mu} = 0$.*

Proof. By hypothesis, $\sigma_3\mathbb{M}_{\mathbf{k}} V_{\mathbf{k}\mu} = \epsilon_{\mathbf{k}\mu} V_{\mathbf{k}\mu}$. After multiplying this equation by $\overline{V}_{\mathbf{k}\nu}$ from the left, one uses the fact that $\overline{V}_{\mathbf{k}\nu}\sigma_3\mathbb{M}_{\mathbf{k}} = \overline{V}_{\mathbf{k}\nu}\epsilon^*_{\mathbf{k}\nu}$ to find

$$\overline{V}_{\mathbf{k}\nu}\sigma_3\mathbb{M}_{\mathbf{k}} V_{\mathbf{k}\mu} = \epsilon_{\mathbf{k}\mu}\overline{V}_{\mathbf{k}\nu} V_{\mathbf{k}\mu} \implies (\epsilon_{\mathbf{k}\mu} - \epsilon^*_{\mathbf{k}\nu})\,\overline{V}_{\mathbf{k}\nu} V_{\mathbf{k}\mu} = 0, \tag{3.26}$$

from which the stated property follows. ■

Now let us consider how the previous properties apply when the Bogoliubov matrix, $\sigma_3\mathbb{M}_{\mathbf{k}}$, has a single zero mode at $\mathbf{k} = \mathbf{Q}$. If we denote the corresponding eigenvector by $V_{\mathbf{Q}\lambda}$, then $\sigma_3\mathbb{M}_{\mathbf{Q}}\, V_{\mathbf{Q}\lambda} = \mathbb{M}_{\mathbf{Q}}\, V_{\mathbf{Q}\lambda} = 0$ implies that $V_{\mathbf{Q}\lambda}$ is also an eigenvector of $\mathbb{M}_{\mathbf{Q}}$. Further, the fact that systems of interest typically display inversion symmetry guarantees that another zero mode exists at the opposite momentum: $\sigma_3\mathbb{M}_{\mathbf{Q}}\, V_{-\mathbf{Q}\lambda} = \mathbb{M}_{\mathbf{Q}}\, V_{-\mathbf{Q}\lambda} = 0$. From Prop. 2, we thus see that $W_{\mathbf{Q}\lambda} := \sigma_1 V^*_{-\mathbf{Q}\lambda}$ fulfills $\sigma_3\mathbb{M}_{\mathbf{Q}}\, W_{\mathbf{Q}\lambda} = \mathbb{M}_{\mathbf{Q}}\, W_{\mathbf{Q}\lambda} = 0$. The key difference with respect to pairs of eigenvectors of $\sigma_3\mathbb{M}_{\mathbf{k}}$ with nonzero eigenvalue is that Prop. 3 does not guarantee that $V_{\mathbf{Q}\lambda}$ and $W_{\mathbf{Q}\lambda}$ are orthogonal. This will be important later on.

Property 4. *Eigenvectors belonging to pure imaginary eigenvalues have zero norm with respect to the metric σ_3.*

Proof. The norm of a vector $V_{\mathbf{k}\mu}$ with respect to the metric σ_3 is defined as $\overline{V}_{\mathbf{k}\mu} V_{\mathbf{k}\mu} = V^\dagger_{\mathbf{k}\mu}\sigma_3 V_{\mathbf{k}\mu}$. If $V_{\mathbf{k}\mu}$ is a right eigenvector of $\sigma_3\mathbb{M}_{\mathbf{k}}$ which has $\epsilon_{\mathbf{k}\mu}$ as an eigenvalue, Prop. 1 implies that $\overline{V}_{\mathbf{k}\mu}$ is a left eigenvector of $\sigma_3\mathbb{M}_{\mathbf{k}}$ corresponding to the eigenvalue $\epsilon^*_{\mathbf{k}\mu}$. Since we have assumed that $\epsilon_{\mathbf{k}\mu}$ is not a real number, $\epsilon_{\mathbf{k}\mu} \neq \epsilon^*_{\mathbf{k}\mu}$ and it thus follows from Prop. 3 that $\overline{V}_{\mathbf{k}\mu} V_{\mathbf{k}\mu} = 0$. ■

Property 5. *If $\mathbb{M}_{\boldsymbol{k}}$ is a positive semidefinite matrix, then the eigenvalues of $\sigma_3\mathbb{M}_{\boldsymbol{k}}$ are all real and the eigenvectors belonging to positive and negative eigenvalues have, respectively, positive and negative norms with respect to the metric σ_3.*

Proof. First, we recall that a Hermitian matrix is said to be positive semidefinite if $v_{\mathbf{k}}^\dagger M_{\mathbf{k}} v_{\mathbf{k}} \geq 0$ for every column vector $v_{\mathbf{k}}$ of $2N_s$ complex numbers. Keeping this in mind, we multiply Eq. (3.19) by $\overline{V}_{\mathbf{k}\mu} = V_{\mathbf{k}\mu}^\dagger \sigma_3$ from the left to obtain

$$V_{\mathbf{k}\mu}^\dagger \mathbb{M}_{\mathbf{k}} V_{\mathbf{k}\mu} = \epsilon_{\mathbf{k}\mu} V_{\mathbf{k}\mu}^\dagger \sigma_3 V_{\mathbf{k}\mu}. \tag{3.27}$$

We then note that the left-hand side of Eq. (3.27) is a real nonnegative number, which can only be zero if $\epsilon_{\mathbf{k}\mu} = 0$. Because the proposition only involves cases in which $\epsilon_{\mathbf{k}\mu} \neq 0$, the left-hand side of Eq. (3.27) is therefore positive. From this, we can draw two conclusions. First, $\epsilon_{\mathbf{k}\mu}$ must be a real number, otherwise $V_{\mathbf{k}\mu}^\dagger \sigma_3 V_{\mathbf{k}\mu}$ would be zero on account of Prop. 4 and Eq. (3.27) would be violated. Second, since the right-hand side must be positive, $\epsilon_{\mathbf{k}\mu}$ and $V_{\mathbf{k}\mu}^\dagger \sigma_3 V_{\mathbf{k}\mu}$ necessarily have the same sign. This completes the proof. ■

As long as we select the correct classical reference state for a spin-wave expansion, $\mathbb{M}_{\mathbf{k}}$ will be positive semidefinite for every $\mathbf{k}$ and the spectrum of $\sigma_3\mathbb{M}_{\mathbf{k}}$ will be real. Prop. 2 then establishes a one-to-one correspondence between eigenvectors associated with eigenvalues of opposite signs. We therefore conclude that $\sigma_3\mathbb{M}_{\mathbf{k}}$ has an equal number of positive and negative eigenvalues. Based on this fact, we can reserve the symbol $V_{\mathbf{k}\mu}$ for the right eigenvectors of $\sigma_3\mathbb{M}_{\mathbf{k}}$ with nonnegative eigenvalues. If we further neglect zero modes for the time being, Prop. 5 allows us to normalize $V_{\mathbf{k}\mu}$ and $W_{\mathbf{k}\mu}$ to $+1$ and -1, respectively. Put together with the orthogonality condition, Prop. 3, this leads to

$$\begin{cases} \sigma_3\mathbb{M}_{\mathbf{k}} V_{\mathbf{k}\mu} = \epsilon_{\mathbf{k}\mu} V_{\mathbf{k}\mu} \\ \sigma_3\mathbb{M}_{\mathbf{k}} W_{\mathbf{k}\mu} = -\epsilon_{-\mathbf{k}\mu} W_{\mathbf{k}\mu} \\ \epsilon_{\mathbf{k}\mu} > 0 \end{cases} \implies \begin{cases} V_{\mathbf{k}\mu}^\dagger \sigma_3 V_{\mathbf{k}\nu} = \delta_{\mu\nu} \\ W_{\mathbf{k}\mu}^\dagger \sigma_3 W_{\mathbf{k}\nu} = -\delta_{\mu\nu} \\ V_{\mathbf{k}\mu}^\dagger \sigma_3 W_{\mathbf{k}\nu} = 0 \end{cases} \tag{3.28}$$

Note that we have also assumed that possibly degenerate eigenvectors are made orthogonal. This can be enforced by means of a Gram-Schmidt orthogonalization or, more ideally, by alternative schemes such as the algorithm described in WESSEL, MILAT[105] or a procedure based on the Cholesky decomposition.[106,107]

Now consider the linear equation

$$c\, V_{\mathbf{k}\mu} + d\, W_{\mathbf{k}\mu} = 0, \quad \text{with } c, d \in \mathbb{C}\,. \tag{3.29}$$

By acting on the left of Eq. (3.29) with $V_{\mathbf{k}\mu}^\dagger \sigma_3$ and $W_{\mathbf{k}\mu}^\dagger \sigma_3$, one arrives at

$$\begin{cases} V_{\mathbf{k}\mu}^\dagger \sigma_3 \left(c\, V_{\mathbf{k}\mu} + d\, W_{\mathbf{k}\mu}\right) = 0 \\ W_{\mathbf{k}\mu}^\dagger \sigma_3 \left(c\, V_{\mathbf{k}\mu} + d\, W_{\mathbf{k}\mu}\right) = 0 \end{cases} \tag{3.30}$$

From Eq. (3.28), it becomes clear that, if $V_{\mathbf{k}\mu}$ and $W_{\mathbf{k}\mu}$ have nonzero eigenvalues, then they are necessarily linearly independent. Indeed, the first and second equations in the linear system above imply that $c = 0$ and $d = 0$, respectively. However, this same conclusion does not hold when $V_{\mathbf{k}\mu}$ and $W_{\mathbf{k}\mu}$ are eigenvectors of $\sigma_3\mathbb{M}_{\mathbf{k}}$ with zero eigenvalues. In this case, we must distinguish between two different types of zero modes:

- Type I: $V_{\mathbf{k}\mu}$ and $W_{\mathbf{k}\mu}$ are linearly dependent and cannot be chosen so as to satisfy the orthonormality relations in Eq. (3.28). In particular, Eq. (3.30) requires that $V^\dagger_{\mathbf{k}\mu}\sigma_3 V_{\mathbf{k}\mu} = 0$. The linear dependence further implies that $\sigma_3\mathbb{M}_{\mathbf{k}}$ does not have $2N_\mathrm{s}$ linearly independent eigenvectors and is therefore non-diagonalizable. While blocks of $\sigma_3\mathbb{M}_{\mathbf{k}}$ can be diagonalized, the zero mode eigenspace can only be reduced to a Jordan block.[103]

- Type II: $V_{\mathbf{k}\mu}$ and $W_{\mathbf{k}\mu}$ are linearly independent. Under this circumstance, it is possible to choose eigenvectors $V_{\mathbf{k}\mu}$ and $W_{\mathbf{k}\mu}$ which satisfy the orthonormality relations in Eq. (3.28).

As justified in Appendix A, a deeper discussion on subtleties arising from type I zero modes is unnecessary for the purposes of this dissertation. We thus refer the interested reader to BLAIZOT; RIPKA[104] and the supplemental material of RAU; MCCLARTY; MOESSNER.[103]

Property 6. *If $\mathbb{M}_{\boldsymbol{k}}$ is a positive semidefinite matrix which does not present type-I zero modes, then all eigenvectors $V_{\boldsymbol{k}\mu}$ and $W_{\boldsymbol{k}\mu}$ of $\sigma_3\mathbb{M}_{\boldsymbol{k}}$ are linearly independent and obey the completeness relation*

$$\sum_{\mu=1}^{N_\mathrm{s}} \left(V_{\boldsymbol{k}\mu}V^\dagger_{\boldsymbol{k}\mu}\sigma_3 - W_{\boldsymbol{k}\mu}W^\dagger_{\boldsymbol{k}\mu}\sigma_3\right) = \mathbb{1}. \tag{3.31}$$

Proof. Let us begin by multiplying the equation

$$\sum_{\mu=1}^{N_\mathrm{s}} \left(c_\mu V_{\mathbf{k}\mu} + d_\mu W_{\mathbf{k}\mu}\right) = 0 \tag{3.32}$$

by $V^\dagger_{\mathbf{k}\nu}\sigma_3$ from the left. As a result of the orthonormality relations, Eq. (3.28), we find that $c_\nu = 0$, $\forall\, \nu$. A similar procedure involving $W^\dagger_{\mathbf{k}\nu}\sigma_3$ gives $d_\nu = 0$, $\forall\, \nu$. Since Eq. (3.32) can only be satisfied when $c_\nu = d_\nu = 0$, $\forall\, \nu$, we conclude that all eigenvectors $V_{\mathbf{k}\mu}$ and $W_{\mathbf{k}\mu}$ are linearly independent. By noting, in addition, that the number of eigenvectors involved in the sum in Eq. (3.31) is equal to the dimension of $\mathbb{M}_{\mathbf{k}}$, we find that the set $\{V_{\mathbf{k}\mu}, W_{\mathbf{k}\mu} |\, \mu = 1, \ldots, N_\mathrm{s}\}$ is complete. ■

Therefore, provided that the Bogoliubov matrix, $\sigma_3\mathbb{M}_{\mathbf{k}}$, does not present type-I zero modes, it is diagonalizable. In this case, each column of the inverse transformation

matrix $\mathbb{T}_{\mathbf{k}}^{-1}$ is given by one of the eigenvectors obeying Eq. (3.28):

$$\begin{cases} \mathbb{X}_{\mathbf{k},\mu\nu} = V_{\mathbf{k}\mu,\nu} \\ \mathbb{Y}_{\mathbf{k},\mu\nu} = V_{\mathbf{k}\mu,N_{\mathrm{s}}+\nu} \end{cases} \tag{3.33}$$

The diagonal matrix defined in Eq. (3.18) then acquires the form

$$\Omega_{\mathbf{k}} := \mathrm{diag}\left(\epsilon_{\mathbf{k}1}, \ldots, \epsilon_{\mathbf{k}N_{\mathrm{s}}}, -\epsilon_{-\mathbf{k}1}, \ldots, -\epsilon_{-\mathbf{k}N_{\mathrm{s}}}\right), \tag{3.34}$$

which leads to the following simplification:

$$\beta_{\mathbf{k}}^{\dagger}\sigma_3\Omega_{\mathbf{k}}\beta_{\mathbf{k}} = \sum_{\mu=1}^{2N_{\mathrm{s}}} \beta_{\mathbf{k}\mu}^{\dagger}\left(\sigma_3\Omega_{\mathbf{k}}\right)_{\mu\mu}\beta_{\mathbf{k}\mu} = \sum_{\mu=1}^{N_{\mathrm{s}}}\left(\epsilon_{\mathbf{k}\mu}b_{\mathbf{k}\mu}^{\dagger}b_{\mathbf{k}\mu} + \epsilon_{-\mathbf{k}\mu}b_{-\mathbf{k}\mu}b_{-\mathbf{k}\mu}^{\dagger}\right). \tag{3.35}$$

By using bosonic commutation relations and once again exploiting the symmetry of the first BZ with respect to the origin of reciprocal space, we finally arrive at the explicit diagonal form

$$\mathcal{H}_{\mathrm{LSW}} = S^2E_{\mathrm{gs},0} + SE_{\mathrm{gs},1} + S\sum_{\mathbf{k}}\sum_{\mu=1}^{N_{\mathrm{s}}}\epsilon_{\mathbf{k}\mu}b_{\mathbf{k}\mu}^{\dagger}b_{\mathbf{k}\mu}, \tag{3.36}$$

where

$$E_{\mathrm{gs},1} = \frac{1}{2}\sum_{\mathbf{k}}\left(\sum_{\mu}\epsilon_{\mathbf{k}\mu} - \mathrm{Tr}\mathbb{A}_{\mathbf{k}}\right) \tag{3.37}$$

is the next-to-leading order (NLO) contribution in $1/S$ to the ground-state energy,

$$E_{\mathrm{gs}}\left(\frac{1}{S}\right) = S^2\sum_{n=0}^{\infty}\left(\frac{1}{S}\right)^n E_{\mathrm{gs},n}. \tag{3.38}$$

The spin-1 excitations which are created by the $b_{\mathbf{k}\mu}$ operators are called *magnons*.

As a final note, we mention that, in the absence of a magnetic field, the term $\mathrm{Tr}\mathbb{A}_{\mathbf{k}}$ equals $SE_{\mathrm{gs},0}$, such that it combines with the leading term $S^2E_{\mathrm{gs},0}$ into $S\left(S+1\right)E_{\mathrm{gs},0}$. This, however, does not occur for $h \neq 0$.

4 HEISENBERG-KITAEV MODEL IN A MAGNETIC FIELD: 1/S EXPANSION

As discussed in Chapter 2, the physics of Kitaev's spin-1/2 honeycomb model and its extensions have attracted an enormous amount of interest over the past years. Much of the recent enthusiasm in this field has been sparked by the discovery that exotic behavior can be induced by applying a magnetic field in specific directions of the quantum magnet α-$RuCl_3$ (Sec. 2.2.5). In parallel, the search for other magnets with strong spin-orbit coupling has resulted in proposals of material candidates to host higher-spin analogs of the Kitaev interaction (Sec. 2.2.6). Remarkably, all of these materials display nontrivial responses to magnetic fields, such as strongly anisotropic magnetization processes and novel field-induced states, due to the lack of spin-rotational symmetry. In this context, the nearest-neighbor Heisenberg-Kitaev model, which was discussed in Secs. 2.2.2 and 2.2.3, has emerged as a minimal model to capture the main physical aspects of Kitaev materials. However, a systematic theoretical study of the effects of a magnetic field beyond the classical limit, i.e., for different spin sizes S, is currently lacking.

In this chapter, we aim to fill this gap by employing an expansion in 1/S to the Hamiltonian

$$\mathcal{H}'_{\mathrm{HK}} = \mathcal{H}_{\mathrm{HK}} + \mathcal{H}_{\mathrm{Z}} = J \sum_{\langle ij \rangle} \mathbf{S}_i \cdot \mathbf{S}_j + K \sum_{\langle ij \rangle_\gamma} S_i^\gamma S_j^\gamma - \mathbf{h} \cdot \sum_i \mathbf{S}_i. \tag{4.1}$$

For convenience, we absorb all constants that appear in the effective moment $g\mu_{\mathrm{B}}\mathbf{S}_i$ of each pseudospin into the field $\mathbf{h} := g\mu_{\mathrm{B}}\mu_0\mathbf{H}$. In addition, we shall constantly discuss our results in terms of the parametrization $J = A\cos\varphi$ and $K = 2A\sin\varphi$, which has also been used in Secs. 2.2.2 and 2.2.3.

Following the work of JANSSEN; ANDRADE; VOJTA,[1] our main focus here will be the stability of the ordered phases induced by magnetic fields applied along to different directions: [001] and [111]. After a brief review of the results obtained in the classical limit, we present an expanded version of CÔNSOLI *et al.*[37]

4.1 Classical phases and phase diagrams

As a preliminary step to our spin-wave calculations, consider the classical limit, $S \to \infty$, of Eq. (4.1). In an early study,[108] classical Monte Carlo simulations showed that the resulting phase diagram for $h = 0$ is in fact fairly similar to the $S = 1/2$ version depicted in Fig. 4(b). Although the regions covered by the Kitaev spin liquid shrink to isolated points as $S \to \infty$, both cases present the same four ordered phases in roughly comparable intervals of φ.

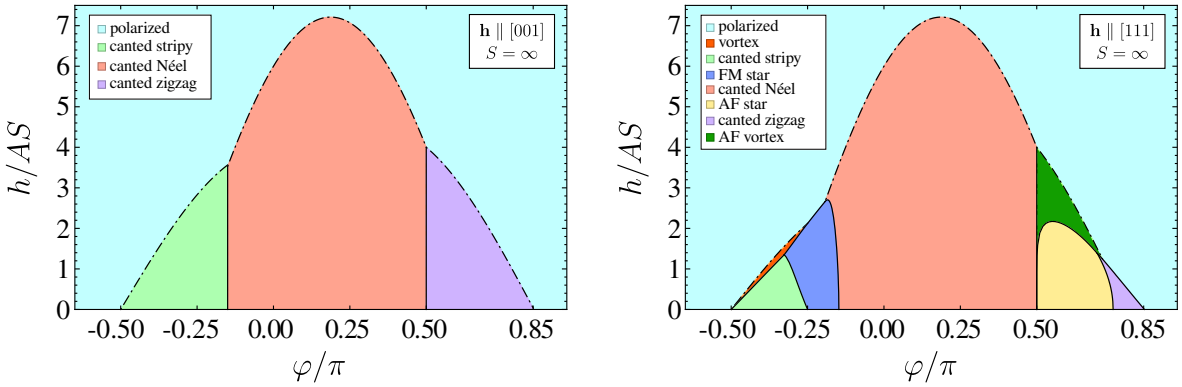

Figure 8 – Classical phase diagrams of the HK model in a [001] and [111] magnetic field. The latter is simplified by a limitation to phases with at most 8 sites per magnetic unit cell. In terms of a $1/S$ expansion, the classical limit formally corresponds to $S \to \infty$. Continuous and first-order phase transitions are represented by dot-dashed and solid lines, respectively.

Source: Adapted from JANSSEN; ANDRADE; VOJTA.[1].

The extension of this analysis to nonzero magnetic fields was carried out by JANSSEN; ANDRADE; VOJTA.[1] In a case study of two distinct field directions, $\mathbf{h} \parallel [001]$ and [111], the authors therein demonstrated that the anisotropic character of the response induced by the Kitaev interaction is striking. While the former field configuration produces but simple canted versions of the zero-field phases, the latter gives rise to an extremely rich phase diagram: Besides the canted stripy, canted zigzag and canted Néel, six novel field-induced phases were identified. In our spin-wave analysis, however, we neglect the existence of two of these additional phases, which have at least 18 sites per magnetic unit cell and cover only small slivers of the classical phase diagram.[1] As we shall see below, this simplifying assumption is made reasonable by the fact that large-unit-cell states are typically destabilized by quantum fluctuations, and hence are expected to be entirely suppressed at the small values of S we are primarily interested in. With this remark in place, Fig. 8 depicts the classical phase diagrams for $\mathbf{h} \parallel [001]$ and [111]. The parametrizations of the listed phases are given in Table 2, whereas representative illustrations of several states stabilized by a [111] field are shown in Fig. 9.

In the following subsections, we describe each of the classical phases appearing in Fig. 8. We also discuss the reason behind the stark difference between both phase diagrams.

4.1.1 Canted Néel

The simplest ordered phase to appear in the diagrams of Fig. 8 is the canted Néel. In the limit of $S \to \infty$, it has the same response to both $\mathbf{h} \parallel [001]$ and [111]: Upon increasing the magnitude of the field from infinitesimal values, the state evolves continuously from a collinear Néel configuration perpendicular to $\mathbf{h}$ toward a fully polarized state, which is

reached at a *critical field* $h = h_{c0}(\varphi)$. Crucially, the fact that the spins can initiate canting from the plane perpendicular to $\mathbf{h}$ renders *uniform* canting energetically favorable.[60] In other words, all canting angles, θ_μ, have the same dependence with respect to h.

However, the simplicity of this behavior is in itself intriguing, for, by showing no fundamental difference in its response to either field direction, the canted Néel seems oblivious to the anisotropic nature of the Kitaev term. To understand this feature, consider the classical HK Hamiltonian applied to a canted Néel state. By noting that all nearest neighbors of an arbitrary spin have the same configuration, one can readily verify that the Kitaev term adds up to an effective Heisenberg interaction, and hence preserves SU(2) spin symmetry in the limit $S \to \infty$. This explains why, regardless of the direction of $\mathbf{h}$, spins cant uniformly in the classical canted Néel phase. On the other hand, the absence of this *accidental* symmetry in a quantum system gives us reason to expect drastic changes upon the inclusion of quantum fluctuations. We will return to this topic in Sec. 4.9.3.

4.1.2 Canted stripy and canted zigzag

Because the accidental symmetry described above only holds for phases with two sites per magnetic unit cell, signs of broken spin-rotational symmetry should emerge already in the classical stripy and zigzag states. This expectation is indeed confirmed by the minimization of the classical energy, which yields a discrete rather than a continuous set of degenerate ground states in the regions covered by the classical zigzag and stripy phases. The degeneracy seen here is a consequence of the residual C_3^* symmetry of the HK Hamiltonian discussed in Secs. 2.2.2 and 2.2.3, and entails three different patterns of each phase whereby the spins lie parallel to the x, y or z axis.

Thus, when a magnetic field is applied along the [001] direction, the stripy and zigzag states initiate uniform canting from either the x or y axis, which are perpendicular to $\mathbf{h}$. Evidently, this renders the z-patterns of both phases unfavorable and reduces the threefold degeneracy observed at zero field to a twofold degeneracy in the canted phases, as the [001] field breaks the C_3^* symmetry of the Hamiltonian. From an experimental perspective, this implies that neutron-scattering experiments should not find Bragg peaks with the same threefold* rotational symmetry observed in absence of a magnetic field.[1] Similarly to the case of the canted Néel, the canted stripy and canted zigzag evolve continuously to the polarized phase, so that the system undergoes a continuous phase transition at the a critical field $h_{c0}(\varphi)$.

The scenario changes drastically when a field is applied along the [111] direction. Although the C_3^* symmetry is preserved in this case, none of the three degenerate patterns of the stripy or zigzag phases lie in the plane perpendicular to $\mathbf{h}$, so that uniform canting

* Actually sixfold, since each pattern produces a pair of Bragg peaks related by inversion symmetry.

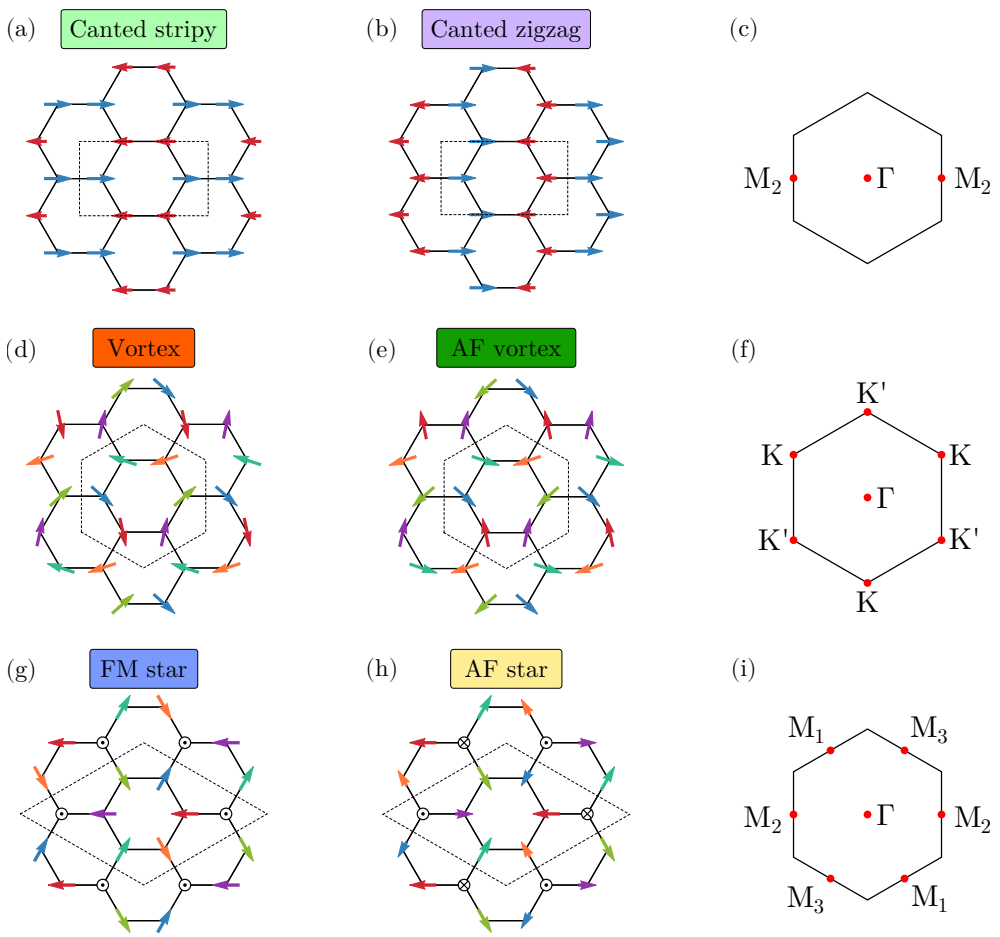

Figure 9 – Left and center panels: Projection of the classical parametrization of ordered phases which arise in a [111] field onto the honeycomb plane. The respective magnetic unit cells are shown in dashed lines. Unequal lengths of the projected spins in the canted zigzag, canted stripy and AF star configurations reflect the occurrence of nonuniform canting. Right panel: Position in the first Brillouin zone of the Bragg peaks related to each pair of magnetic orders. Note that all of the phases present a Bragg peak at the Γ point, because the latter is associated with the growth of the magnetization with increasing h.

Source: By the author.

is prohibited. As the field increases, the inhomogeneously canted versions of the stripy and zigzag states become energetically unfavorable in comparison to other, more intricate, orderings which allow canting mechanisms with larger magnetic susceptibilities.[1,60] This competition induces the metamagnetic transitions to different ordered phases shown in Fig. 8, and thus explains the conspicuous differences between the phase diagrams. By same logic, one expects novel field-induced classical orders to arise for any field direction away from the x, y and z cubic axes.

4.1.3 Vortex and AF vortex

Two of the novel phases induced by a [111] magnetic field are called vortex and AF vortex. While each of them is stabilized in the vicinity of one of the Kitaev points, $\varphi = \pm\pi/2$, both have six sites per magnetic units cell and exhibit uniform canting. Moreover, their spin structure factors reveal Bragg peaks at the Γ, K and K' points of the first Brillouin zone (BZ),[1] see Fig. 9(f). Since the last two points are not connected by primitive vectors of the reciprocal lattice, these are multi-$\mathbf{Q}$ phases. It is thus the combination of different ordering wave vectors that give rise to the chiral magnetic orders displayed in Figs. 9(d,e).

Another interesting feature is that both of these phases display an accidental U(1) degeneracy. As expressed in Table 2, their classical energies remain invariant when the spins of the two crystallographic sublattices of the honeycomb lattice are rotated around the [111] direction by opposite angles, ξ and $-\xi$. However, we will see in Sec. 4.9.4 that this accidental degeneracy is lifted in a quantum system.

4.1.4 FM star and AF star

Two other novel phases to appear in a [111] field are called FM star and AF star. As expressed in Table 2 and depicted in Figs. 9(g,h), they both have the distinctive feature that the spins in two of their eight magnetic sublattices remain locked to the [111] direction. Calculations of their classical spin structure factors further show that the FM star and AF star are multi-$\mathbf{Q}$ phases with Bragg peaks at the Γ, M_1, M_2 and M_3 points of the first BZ,[1] a trait which is also made clear by the LSW spectra we present in Sec. 4.3.2.

From Fig. 8, one can see that, differently from the vortex phases, the FM star and AF star reach down to infinitesimal fields. This is remarkable feature, because it means that, for certain intervals of φ, an infinitesimal [111] magnetic field is sufficient to drive a phase transition from the stripy and zigzag. A clue as to the reason for such a curious behavior lies in the fact that each of the star phases stem from a Klein point, $(\varphi, h) = (-\pi/4, 0)$ or $(3\pi/4, 0)$. In light of the discussion in Sec. 2.2.3, this suggests that the zero-field FM star and AF star are members of the hidden-SU(2) ground-state manifold with the largest magnetic susceptibility in a [111] field. One can indeed check that this is

Table 2 – Parametrizations of the classical phases of the HK model in [001] and [111] magnetic fields. ϕ_i and θ_i represent the azimuthal and polar angles with respect to the auxiliary coordinate system $\{\hat{e}_1^0, \hat{e}_2^0, \hat{e}_3^0\}$ defined in Sec. 3.2. The vector $\mathbf{R}_i$ is measured in units of the lattice constant and given in a cartesian coordinate system with its origin at the center of an arbitrary hexagon of the honeycomb lattice.

Phase	i	$\mathbf{R}_i$	ϕ_i	θ_i
Polarized	1	$(1,0)$	0	0
	2	$\left(\cos\frac{\pi}{3}, \sin\frac{\pi}{3}\right)$	0	0
Canted Néel	1	$(1,0)$	0	θ
	2	$\left(\cos\frac{\pi}{3}, \sin\frac{\pi}{3}\right)$	π	θ
Canted zigzag	1	$(1,0)$	π	θ
	2	$\left(\cos\frac{\pi}{3}, \sin\frac{\pi}{3}\right)$	π	θ
	3	$\left(\cos\frac{2\pi}{3}, \sin\frac{2\pi}{3}\right)$	0	θ'
	4	$(-1,0)$	0	θ'
Canted stripy	1	$(1,0)$	π	θ
	2	$\left(\cos\frac{\pi}{3}, \sin\frac{\pi}{3}\right)$	0	θ'
	3	$\left(\cos\frac{2\pi}{3}, \sin\frac{2\pi}{3}\right)$	0	θ'
	4	$(-1,0)$	π	θ
FM star	1	$(1,0)$	π	θ
	2	$\left(\cos\frac{\pi}{3}, \sin\frac{\pi}{3}\right)$	$\frac{\pi}{3}$	θ
	3	$\left(\cos\frac{2\pi}{3}, \sin\frac{2\pi}{3}\right)$	$\frac{5\pi}{3}$	θ
	4	$(-1,0)$	π	θ
	5	$\left(\cos\frac{4\pi}{3}, \sin\frac{4\pi}{3}\right)$	$\frac{\pi}{3}$	θ
	6	$\left(\cos\frac{5\pi}{3}, \sin\frac{5\pi}{3}\right)$	$\frac{5\pi}{3}$	θ
	7	$2\left(\cos\frac{2\pi}{3}, \sin\frac{2\pi}{3}\right)$	0	0
	8	$(2,0)$	0	0

Phase	i	$\mathbf{R}_i$	ϕ_i	θ_i
Vortex	1	$(1,0)$	$\frac{5\pi}{3}-\xi$	θ
	2	$\left(\cos\frac{\pi}{3}, \sin\frac{\pi}{3}\right)$	$\frac{5\pi}{3}+\xi$	θ
	3	$\left(\cos\frac{2\pi}{3}, \sin\frac{2\pi}{3}\right)$	$\frac{\pi}{3}-\xi$	θ
	4	$(-1,0)$	$\frac{\pi}{3}+\xi$	θ
	5	$\left(\cos\frac{4\pi}{3}, \sin\frac{4\pi}{3}\right)$	$\pi-\xi$	θ
	6	$\left(\cos\frac{5\pi}{3}, \sin\frac{5\pi}{3}\right)$	$\pi+\xi$	θ
AF vortex	1	$(1,0)$	$\frac{2\pi}{3}-\xi$	θ
	2	$\left(\cos\frac{\pi}{3}, \sin\frac{\pi}{3}\right)$	$\frac{5\pi}{3}+\xi$	θ
	3	$\left(\cos\frac{2\pi}{3}, \sin\frac{2\pi}{3}\right)$	$\frac{4\pi}{3}-\xi$	θ
	4	$(-1,0)$	$\frac{\pi}{3}+\xi$	θ
	5	$\left(\cos\frac{4\pi}{3}, \sin\frac{4\pi}{3}\right)$	$-\xi$	θ
	6	$\left(\cos\frac{5\pi}{3}, \sin\frac{5\pi}{3}\right)$	$\pi+\xi$	θ
AF star	1	$(1,0)$	0	θ
	2	$\left(\cos\frac{\pi}{3}, \sin\frac{\pi}{3}\right)$	$\frac{\pi}{3}$	θ'
	3	$\left(\cos\frac{2\pi}{3}, \sin\frac{2\pi}{3}\right)$	$\frac{2\pi}{3}$	θ
	4	$(-1,0)$	π	θ'
	5	$\left(\cos\frac{4\pi}{3}, \sin\frac{4\pi}{3}\right)$	$\frac{4\pi}{3}$	θ
	6	$\left(\cos\frac{5\pi}{3}, \sin\frac{5\pi}{3}\right)$	$\frac{5\pi}{3}$	θ'
	7	$2\left(\cos\frac{2\pi}{3}, \sin\frac{2\pi}{3}\right)$	0	0
	8	$(2,0)$	0	π

Source: Adapted from JANSSEN; ANDRADE; VOJTA.[1]

the case by applying the Klein transformation to FM and Néel states ordered along the [111] direction; the results are precisely the zero-field FM star and AF star, respectively. As the E sublattice remains invariant under the Klein transformation (see Eq. (2.12)), this explains why a pair of spins in the magnetic unit cells of the star phases remain locked to the [111] direction.

4.2 Generic spin-wave Hamiltonian for the ordered phases

Now that we have introduced the classical phases of the model, let us gear the formalism presented in Sec. 3.2 to treat the HK Hamiltonian in a magnetic field. For convenience, we begin by breaking Eq. (4.1) into different parts

$$\mathcal{H}'_{\mathrm{HK}} = \sum_{\gamma=x,y,z} \mathcal{H}^{(\gamma)} + \mathcal{H}_{\mathrm{Z}} = \sum_{n=0}^{\infty} S^{2-\frac{n}{2}} \mathcal{H}_n. \tag{4.2}$$

If we identify the nearest neighbor of site μ in unit cell i along a γ-bond by the subindices $j\nu_\gamma$, we can write the spin-spin interaction terms as

$$\mathcal{H}^{(\gamma)} = {\sum_{i\mu}}' \left(J\mathbf{S}_{i\mu} \cdot \mathbf{S}_{j\nu_\gamma} + K\, S^{\gamma}_{i\mu} S^{\gamma}_{j\nu_\gamma} \right) = {\sum_{i\mu}}' \sum_{m,n=1}^{3} \gamma^{\mu}_{mn} S^{m}_{i\mu} S^{n}_{j\nu_\gamma}, \tag{4.3}$$

with

$$\gamma^{\mu}_{mn} = J \sum_{\ell=1}^{3} \mathbb{R}_{\ell m}\left(\phi_\mu, \theta_\mu\right) \mathbb{R}_{\ell n}\left(\phi_{\nu_\gamma}, \theta_{\nu_\gamma}\right) + K\, \mathbb{R}_{\gamma m}\left(\phi_\mu, \theta_\mu\right) \mathbb{R}_{\gamma n}\left(\phi_{\nu_\gamma}, \theta_{\nu_\gamma}\right). \tag{4.4}$$

The primed sum in Eq. (4.3) indicates that the sum over μ only runs over half of the N_{s} sites in the magnetic unit cell, all of which belong to the same crystallographic sublattice of the honeycomb lattice. Further, notice that we have also used the letter γ to indicate entries of the $\mathbb{B}$ matrices. Whenever this happens, one must understand that an implicit association $\{x, y, z\} \to \{1, 2, 3\}$ is being made. The Zeeman term in turn can be expressed as

$$\mathcal{H}_{\mathrm{Z}} = -h\, \hat{\mathbf{e}}^0_3 \cdot \sum_{i\mu} \mathbf{S}_{i\mu} = -h \sum_{i\mu\nu} r^{\mu}_{\nu} S^{\nu}_{i\mu}. \tag{4.5}$$

Because the coefficients $r^{\mu}_{\nu}\left(\theta_\mu\right)$ are constructed from the rotation matrix $\mathbb{R}_3\left(\theta_\mu\right)$, it follows that $r^{\mu}_{2} = 0$.

This construction allows one to write any n-boson term of the spin-wave Hamiltonian in a compact manner. Here, however, we shall restrict our analysis to $n \leq 3$. Since the spin coordinate system is now compatible with the classical ground state, we can use the

HP transformation, Eq. (3.3), to find

$$\mathcal{H}_0 = \frac{N_c}{2}\sum_{\mu}\left(\sum_{\gamma}\gamma_{33}^{\mu} - \frac{2h}{S}r_3^{\mu}\right) \tag{4.6}$$

$$\mathcal{H}_1 = \frac{1}{\sqrt{2}}\sum_{i\mu\gamma}{}'\left[\left(\gamma_{13}^{\mu}+\mathrm{i}\gamma_{23}^{\mu}\right)a_{i\mu}^{\dagger} + \left(\gamma_{31}^{\mu}+\mathrm{i}\gamma_{32}^{\mu}\right)a_{j\nu_\gamma}^{\dagger}\right] + \frac{h/S}{\sqrt{2}}\sum_{i\mu} r_1^{\mu}a_{i\mu}^{\dagger} + \text{h.c.} \tag{4.7}$$

$$\begin{aligned}\mathcal{H}_2 = {} & \frac{1}{2}\sum_{i\mu\gamma}{}'\left\{\left[\gamma_{11}^{\mu}+\gamma_{22}^{\mu}-\mathrm{i}\left(\gamma_{12}^{\mu}-\gamma_{21}^{\mu}\right)\right]a_{i\mu}^{\dagger}a_{j\nu_\gamma} + \left[\gamma_{11}^{\mu}-\gamma_{22}^{\mu}+\mathrm{i}\left(\gamma_{12}^{\mu}+\gamma_{21}^{\mu}\right)\right]a_{i\mu}^{\dagger}a_{j\nu_\gamma}^{\dagger}\right\} \\ & - \frac{1}{2}\sum_{i\mu}\left(\sum_{\gamma}\gamma_{33}^{\mu} - \frac{h}{S}r_3^{\mu}\right)a_{i\mu}^{\dagger}a_{i\mu} + \text{h.c.}\end{aligned} \tag{4.8}$$

$$\begin{aligned}\mathcal{H}_3 = {} & -\frac{1}{4\sqrt{2}}\sum_{i\mu\gamma}{}'\left\{\left(\gamma_{13}^{\mu}-\mathrm{i}\gamma_{23}^{\mu}\right)a_{i\mu}^{\dagger}a_{i\mu}a_{i\mu} + 4a_{i\mu}^{\dagger}a_{j\nu_\gamma}^{\dagger}\left[\left(\gamma_{13}^{\mu}+\mathrm{i}\gamma_{23}^{\mu}\right)a_{j\nu_\gamma} + \left(\gamma_{31}^{\mu}+\mathrm{i}\gamma_{32}^{\mu}\right)a_{i\mu}\right]\right. \\ & \left. + \left(\gamma_{31}^{\mu}-\mathrm{i}\gamma_{32}^{\mu}\right)a_{j\nu_\gamma}^{\dagger}a_{j\nu_\gamma}a_{j\nu_\gamma}\right\} - \frac{h/S}{4\sqrt{2}}\sum_{i\mu} r_1^{\mu}a_{i\mu}^{\dagger}a_{i\mu}a_{i\mu} + \text{h.c.}\end{aligned} \tag{4.9}$$

The fact that we expand around a state that minimizes the ground-state energy ensures that $\mathcal{H}_1(\boldsymbol{\phi},\boldsymbol{\theta}) = 0$, which in turn allows us to simplify Eq. (4.9) considerably. The result reads

$$\mathcal{H}_3 = -\frac{1}{\sqrt{2}}\sum_{i\mu\gamma}{}'\left[\left(\gamma_{13}^{\mu}+\mathrm{i}\gamma_{23}^{\mu}\right)a_{i\mu}^{\dagger}a_{j\nu_\gamma}^{\dagger}a_{j\nu_\gamma} + \left(\gamma_{31}^{\mu}+\mathrm{i}\gamma_{32}^{\mu}\right)a_{j\nu_\gamma}^{\dagger}a_{i\mu}^{\dagger}a_{i\mu}\right] + \text{h.c.}. \tag{4.10}$$

4.3 Linear spin-wave theory for the ordered phases

4.3.1 Linear spin-wave Hamiltonians

Here, we are specifically interested in the contributions of orders $n = 0$ and $n = 2$ of the spin-wave Hamiltonian. After a Fourier transform, the quadratic term, Eq. (4.8) becomes

$$\begin{aligned}\mathcal{H}_2 = {} & \frac{1}{2}\sum_{\mathbf{k}\mu\gamma}{}'e^{\mathrm{i}\mathbf{k}\cdot\boldsymbol{\delta}_\gamma}\left\{\left[\gamma_{11}^{\mu}+\gamma_{22}^{\mu}-\mathrm{i}\left(\gamma_{12}^{\mu}-\gamma_{21}^{\mu}\right)\right]a_{\mathbf{k}\mu}^{\dagger}a_{\mathbf{k}\nu_\gamma} + \left[\gamma_{11}^{\mu}-\gamma_{22}^{\mu}+\mathrm{i}\left(\gamma_{12}^{\mu}+\gamma_{21}^{\mu}\right)\right]a_{\mathbf{k}\mu}^{\dagger}a_{-\mathbf{k}\nu_\gamma}^{\dagger}\right\} \\ & - \frac{1}{2}\sum_{\mathbf{k}\mu}\left(\sum_{\gamma}\gamma_{33}^{\mu} - \frac{h}{S}r_3^{\mu}\right)a_{\mathbf{k}\mu}^{\dagger}a_{\mathbf{k}\mu} + \text{h.c.}\end{aligned} \tag{4.11}$$

Here, $\boldsymbol{\delta}_\gamma$ denotes the vector which connects a site in the honeycomb lattice to its nearest neighbor along a γ-bond. In units of the lattice constant, a possible set of choices is $\boldsymbol{\delta}_x = \left(-1/2, \sqrt{3}/2\right)$, $\boldsymbol{\delta}_y = \left(-1/2, -\sqrt{3}/2\right)$ and $\boldsymbol{\delta}_z = (1, 0)$.

The final step required to determine the linear spin-wave Hamiltonian is to cast Eq. (4.11) into the form shown in Eqs. (3.5) and (3.8), with $\mathbb{A}_{\mathbf{k}} = \mathbb{A}_{\mathbf{k}}^{\dagger}$ and $\mathbb{B}_{\mathbf{k}} = \mathbb{B}_{-\mathbf{k}}^{\mathrm{T}}$. To fulfill these conditions, the diagonal terms must be symmetrized in the following way:

$$\sum_{\mathbf{k}} a_{\mathbf{k}\mu}^{\dagger}a_{\mathbf{k}\mu} = \frac{1}{2}\sum_{\mathbf{k}}\left(a_{\mathbf{k}\mu}^{\dagger}a_{\mathbf{k}\mu} + a_{\mathbf{k}\mu}a_{\mathbf{k}\mu}^{\dagger} - 1\right) = -\frac{N_c}{2} + \frac{1}{2}\sum_{\mathbf{k}}\left(a_{\mathbf{k}\mu}^{\dagger}a_{\mathbf{k}\mu} + a_{-\mathbf{k}\mu}a_{-\mathbf{k}\mu}^{\dagger}\right). \tag{4.12}$$

A first BZ which is symmetric with respect to the origin of reciprocal space guarantees the validity of the last equality in Eq. (4.12). The off-diagonal terms are treated similarly; however, since they involve different bosonic modes, we simply find

$$\begin{aligned}\sum_{\mathbf{k}} e^{\mathrm{i}\mathbf{k}\cdot\boldsymbol{\delta}_\gamma} a^\dagger_{\mathbf{k}\mu} a_{\mathbf{k}\nu_\gamma} &= \frac{1}{2}\sum_{\mathbf{k}} \left(e^{\mathrm{i}\mathbf{k}\cdot\boldsymbol{\delta}_\gamma} a^\dagger_{\mathbf{k}\mu} a_{\mathbf{k}\nu_\gamma} + e^{-\mathrm{i}\mathbf{k}\cdot\boldsymbol{\delta}_\gamma} a_{-\mathbf{k}\nu_\gamma} a^\dagger_{-\mathbf{k}\mu}\right),\\ \sum_{\mathbf{k}} e^{\mathrm{i}\mathbf{k}\cdot\boldsymbol{\delta}_\gamma} a^\dagger_{\mathbf{k}\mu} a^\dagger_{-\mathbf{k}\nu_\gamma} &= \frac{1}{2}\sum_{\mathbf{k}} \left(e^{\mathrm{i}\mathbf{k}\cdot\boldsymbol{\delta}_\gamma} a^\dagger_{\mathbf{k}\mu} a^\dagger_{-\mathbf{k}\nu_\gamma} + e^{-\mathrm{i}\mathbf{k}\cdot\boldsymbol{\delta}_\gamma} a^\dagger_{\mathbf{k}\nu_\gamma} a^\dagger_{-\mathbf{k}\mu}\right).\end{aligned} \tag{4.13}$$

Thus, we finally obtain the spin-wave Hamiltonian by substituting the expressions above into Eq. (4.11).

$$\mathbb{A}_{\mathbf{k},\mu\nu} = \delta_{\mu\nu}\left(\sum_\gamma \gamma^\mu_{33} - \frac{h}{S} r^\mu_3\right) + \frac{(1-\delta_{\mu\nu})}{2} e^{i\mathbf{k}\cdot\boldsymbol{\delta}_\gamma}\left[\gamma^\mu_{11} + \gamma^\mu_{22} - \mathrm{i}\left(\gamma^\mu_{12} - \gamma^\mu_{21}\right)\right], \tag{4.14}$$

$$\mathbb{B}_{\mathbf{k},\mu\nu} = \frac{(1-\delta_{\mu\nu})}{2}\left[\gamma^\mu_{11} - \gamma^\mu_{22} + \mathrm{i}\left(\gamma^\mu_{12} + \gamma^\mu_{21}\right)\right]. \tag{4.15}$$

Moreover, one readily verifies that the symmetrization procedure generates the (partial) zero-point energy correction

$$\frac{SN_c}{2}\sum_\mu\left(\sum_\gamma \gamma^\mu_{33} - \frac{h}{S} r^\mu_3\right) = \frac{S}{2}\sum_{\mathbf{k}} \mathrm{Tr}\mathbb{A}_{\mathbf{k}}, \tag{4.16}$$

which is in therefore in accordance with Eq. (3.5). Note that Eq. (4.16) is momentum-independent because we have assigned a different bosonic species to each magnetic sublattice. This contribution is to be added to the classical ground-state energy

$$E_{\mathrm{gs},0} = S^2\mathcal{H}_0 = \frac{N_c S^2}{2}\sum_\mu\left(\sum_\gamma \gamma^\mu_{33} - \frac{2h}{S} r^\mu_3\right) \tag{4.17}$$

As mentioned in Sec. 3.2, Eq. (4.16) is not proportional to (4.17) unless $h = 0$.

4.3.2 Linear spin-wave spectra

By using the parametrizations in Table 2 as inputs to Eqs. (4.4), (4.14), (4.15) and (3.8), one can assemble the LSW matrix, $\mathbb{M}_{\mathbf{k}}$, for all ordered phases shown in the classical phase diagrams of Fig. 8. According to the theory introduced in Sec. 3.2.1, the leading-order magnon spectrum is then given by the positive eigenvalues of the modified matrix $\sigma_3\mathbb{M}_{\mathbf{k}}$. In the following, we present and discuss the results of implementing this procedure.

Fig. 10 illustrate how the LSW spectrum evolves upon increasing the magnitude of $\mathbf{h} \parallel [001]$ for three different values of φ, one for each of the ordered phases that arise in this field direction. The plots shown for the canted zigzag and canted stripy combine the spectra of two degenerate patterns of each phase, see Sec. 4.1.2. The dispersion remains gapless up to $h_{\mathrm{c}0}$ in all three phases, reflecting an accidental continuous degeneracy related

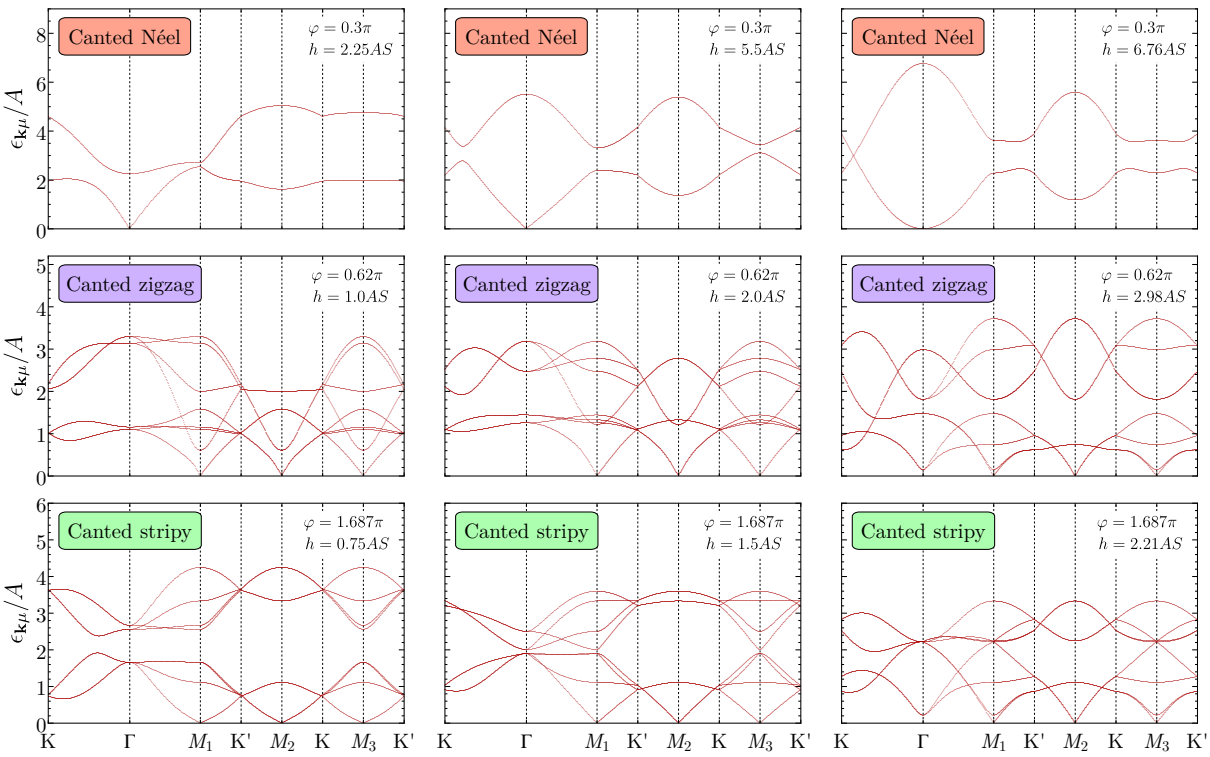

Figure 10 – Linear spin-wave spectra in the ordered phases in a $\mathbf{h} \parallel [001]$ magnetic field for increasing values of h along lines of constant φ. The right column of the panel represents data immediately below the classical critical field, h_{c0}. The corresponding path along high-symmetry lines of the Brillouin zone is shown in Fig. 11. The plots related to the canted zigzag and canted stripy superimpose the spectra of two degenerate patterns of each phase.

Source: By the author.

to rotations of the magnetic orders around $\mathbf{h}$. Such *pseudo-Goldstone modes* acquire a gap due to quantum fluctuations,[103] as an ObD mechanism selects states which present canting in either the xz or yz plane. In the canted Néel, the low-energy portion of the dispersion gradually changes from a linear to a quadratic shape as the field increases, whereas the opposite trend takes place in the canted stripy. Moreover, as $h \to h_{c0}^{-}$, one can identify band crossings in each case which also appear in the LSW spectra of the high-field polarized phase. In the canted zigzag and canted stripy, a second band is lowered down to the M_1 and M_3 points as we approach h_{c0}, while the gap closes at the Γ point as well.

Turning to the case of a [111] field, depicted in Fig. 11, we see that only three of the ordered phases remain gapless for $h > 0$. These, however, are but other examples of pseudo-Goldstone modes, as they correspond precisely the canted Néel, vortex and AF vortex, in which accidental continuous degeneracies are lifted by ObD effects, as discussed in Secs. 4.9.3 and 4.9.4. The spectra of the vortex phases were computed with respect to the state that minimizes the zero-point energy within LSWT, see Sec. 4.9.4. The plots corresponding to the canted zigzag and canted stripy now combine the spectra of three

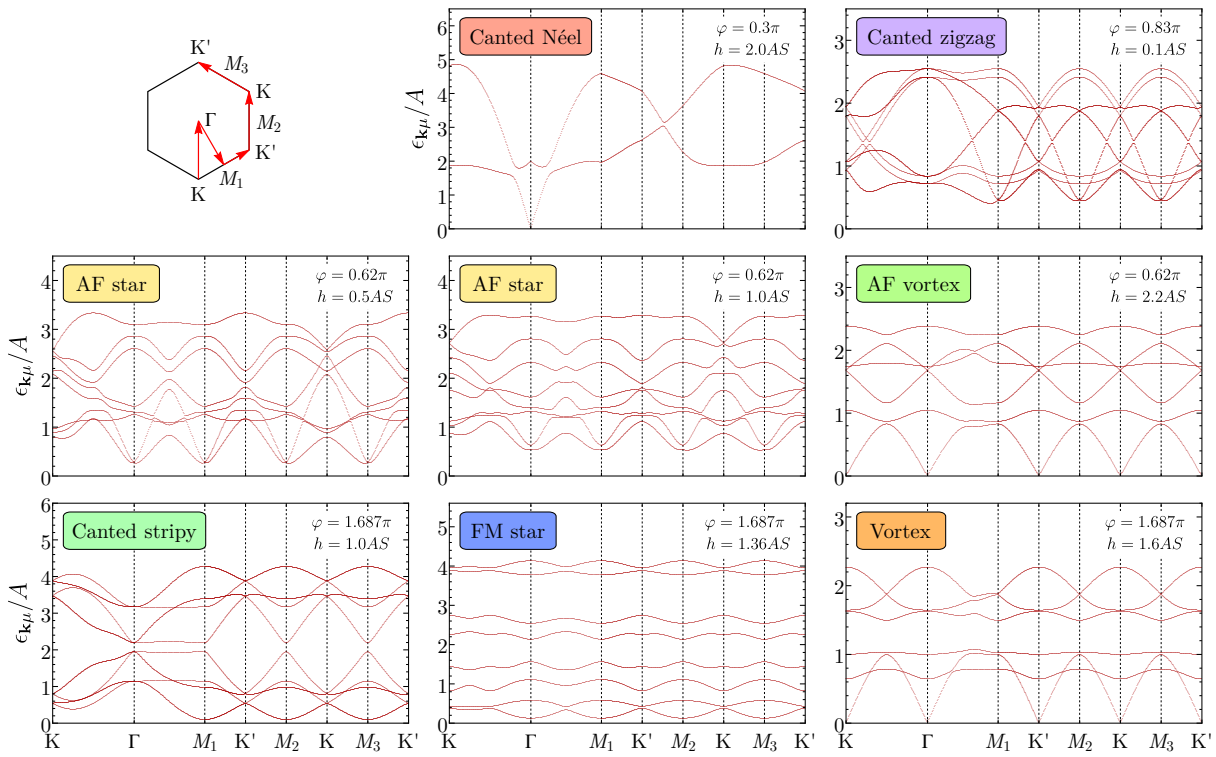

Figure 11 – Linear spin-wave spectra in several of the ordered phases in a [111] magnetic field. The corresponding path along high-symmetry lines of the Brillouin zone is shown on the top left corner of the figure. The plots related to the canted zigzag and canted stripy superimpose the spectra of three degenerate patterns of each phase. The only spectra that remain gapless under the application of a magnetic field are those of the canted Néel and vortex phases.

Source: By the author.

degenerate patterns.

4.3.3 Quantum corrections to the magnetization

The theory presented in Sec. 3.2.1 provides the means to calculate the NLO contribution in $1/S$ to the $T = 0$ magnetization per site,

$$m_h = -\frac{1}{N}\frac{\partial E_{gs}}{\partial h} = -\frac{S^2}{N}\frac{\partial}{\partial h}\left[E_{\mathrm{gs},0} + \frac{E_{\mathrm{gs},1}}{S} + \mathcal{O}\left(\frac{1}{S^2}\right)\right], \tag{4.18}$$

where $N = N_{\mathrm{s}}N_{\mathrm{c}}$ denotes the total number of sites. With Eq. (4.18) in hands, let us consider a few results for $\mathbf{h} \parallel [001]$. As discussed in Sec. 4.1, the classical ground state in this setting is characterized by spins canting uniformly toward the [001] direction from $h = 0$ up to the classical critical field, $h_{\mathrm{c0}}(\varphi)$. At this point, all spins become parallel to $\mathbf{h}$ and the classical ordered phase gives way to a fully polarized phase. Consequently, the magnetization increases linearly with the field at leading order in $1/S$, reaching its saturation at h_{c0}.

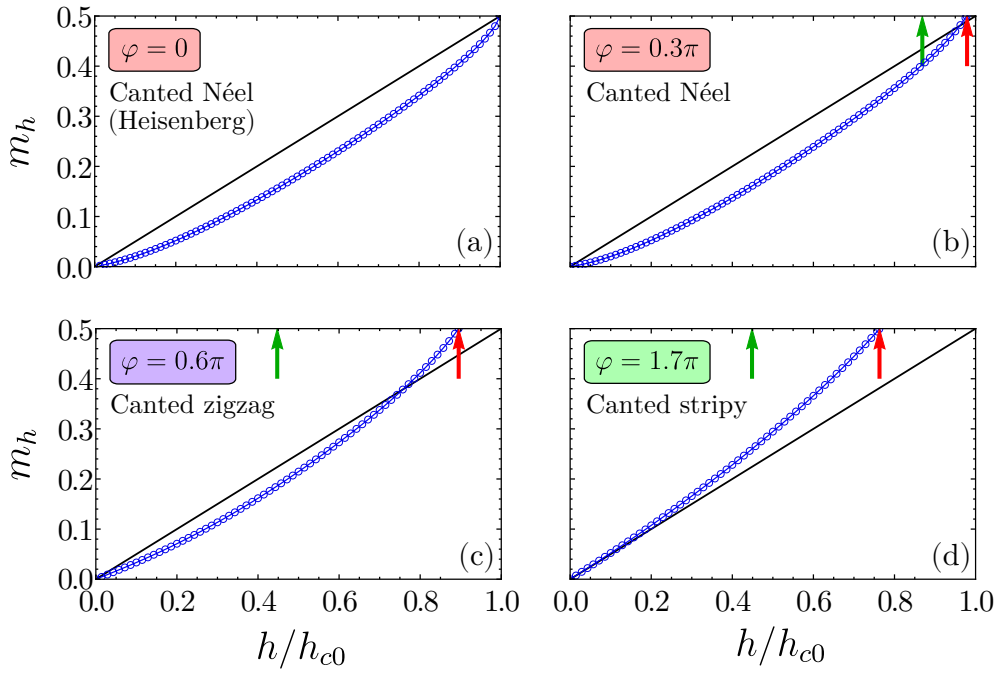

Figure 12 – Magnetization m_h in units of S as a function of h in a magnetic field $\mathbf{h} \parallel [001]$, at leading (black) and next-to-leading (blue) order in $1/S$ for $S = 1/2$ and different values of φ. To aid the comparison, the horizontal axes have been rescaled by the respective classical critical field h_{c0}. Red arrows highlight an unphysical saturation of the magnetization, suggesting that, except in the Heisenberg limit (a), phase transitions occur below the classical critical field. Green arrows indicate the positions of the corrected critical fields according to Secs. 4.4 and 4.6

Source: By the author.

However, such a simple picture changes shape as soon as quantum fluctuations are taken into account. A previous study on the square-lattice Heisenberg antiferromagnet showed that higher-order terms in $1/S$ lower the magnetization up to h_{c0}, where both classical and quantum curves saturate at their maximum value $m_h = S$.[109] The authors therein explained such a behavior by considering the integral version of Eq. (4.18):

$$E_{\text{gs}}\left(0, \frac{1}{S}\right) - E_{\text{gs}}\left(h_{c0}, \frac{1}{S}\right) = N \int_0^{h_{c0}} m_h dh, \tag{4.19}$$

with $E_{\text{gs}} = E_{\text{gs}}(h, 1/S)$. Since the polarized state is an eigenstate of the Hamiltonian of a Heisenberg antiferromagnet in a magnetic field, quantum fluctuations vanish for $h \geq h_{c0}$ and $E_{gs}(h_{c0}, 1/S)$ coincides with its classical value. On the other hand, it is a well-known fact that higher-order corrections in $1/S$ reduce the ground-state energy at zero field.[110,111] Therefore, by comparing different orders in $1/S$ from both sides of Eq. (4.19) and ruling out the possibility of a negative magnetic susceptibility, one concludes that quantum fluctuations should indeed lower the magnetization in the open interval $(0, h_{c0})$.

When applying our calculations to the SU(2) symmetric AF Heisenberg point, $\varphi = 0$, we obtained a magnetization curve which agrees with the argument presented

in the last paragraph, see Fig. 12(a). A markedly different behavior, however, emerges upon considering $K \neq 0$. As illustrated in Figs. 12 (b)-(d), the quantum correction to m_h becomes positive at sufficiently high fields, causing the NLO curves to cross their classical counterparts and saturate below h_{c0}. Yet, because the polarized state is not an eigenstate of the full HK Hamiltonian, Eq. (4.1), quantum fluctuations take place even for $h \geq h_{c0}$ and prevent the magnetization from saturating at *any* finite field.[1,87] Hence, the high-field portions of the NLO magnetization curves are guaranteed to be unphysical. Although we have presented results for $S = 1/2$ in Figs. 12, such an inconsistency applies for all finite values of S. Moreover, we found that it persists for $\mathbf{h} \parallel [111]$, hinting that it should also be present for other field directions.

Based on this evidence, we claim that our results point toward the occurrence of a phase transition below h_{c0} and call for a redefinition of the critical field, h_c. In the next sections, we show how one can find in nonlinear spin-wave theory the tools to solve this issue.

4.4 Quantum corrections to the direction of magnetic moments

In LSWT, the angles $\{\boldsymbol{\phi}, \boldsymbol{\theta}\}$ that parametrize the directions of the spins in the ordered phases are determined via the minimization of the classical Hamiltonian $\mathcal{H}_0(\boldsymbol{\phi}, \boldsymbol{\theta})$. Consequently, the linear term $\mathcal{H}_1(\boldsymbol{\phi}, \boldsymbol{\theta})$ vanishes. Nevertheless, in dealing with noncollinear magnetic orders such as the canted phases discussed in Sec. 4.3.3, additional single-boson contributions stem from the cubic term, $\mathcal{H}_3$, and lead to a renormalization of the parametrization angles, $\{\boldsymbol{\phi}, \boldsymbol{\theta}\} \to \left\{\tilde{\boldsymbol{\phi}}, \tilde{\boldsymbol{\theta}}\right\}$, which affects physical observables already at NLO order in $1/S$.[109,112] In the following, we provide an outline of this procedure and connect it to the results presented in Sec. 4.3.3.

We begin by writing $\mathcal{H}_3$ in normal order with respect to the Bogoliubov quasiparticles $\left\{b^\dagger_{\mathbf{k}\mu}, b_{\mathbf{k}\mu}\right\}$:

$$\mathcal{H}_3 = \,:\mathcal{H}_3: + \mathcal{H}_3^{(1)}, \tag{4.20}$$

such that all creation operators $b^\dagger_{\mathbf{k}\mu}$ are placed to the left of annihilation operators $b_{\mathbf{k}\mu}$ in $:\mathcal{H}_3:$. Because $:\mathcal{H}_3:$ only yields corrections beyond NLO in $1/S$,[90,103,113,114] it will not be considered here. Instead, we apply a mean-field treatment by including only the residual single-boson term, $\mathcal{H}_3^{(1)}$.[109] The new parametrization angles, $\left\{\tilde{\boldsymbol{\phi}}, \tilde{\boldsymbol{\theta}}\right\}$, are then determined by rendering the complete linear term zero,

$$S^{3/2}\mathcal{H}_1\left(\tilde{\boldsymbol{\phi}}, \tilde{\boldsymbol{\theta}}\right) + S^{1/2}\mathcal{H}_3^{(1)}\left(\tilde{\boldsymbol{\phi}}, \tilde{\boldsymbol{\theta}}\right) = 0. \tag{4.21}$$

In the same spirit of Eq. (3.4), one can expand the new angles around their classical

values, $\{\boldsymbol{\phi}, \boldsymbol{\theta}\}$, in a power series in $1/S$:

$$\tilde{\phi}_\mu = \sum_{n=0}^{\infty} \left(\frac{1}{S}\right)^n \tilde{\phi}_{\mu n} \equiv \phi_\mu + \frac{1}{S}\delta\phi_\mu + \mathcal{O}\left(\frac{1}{S^2}\right), \tag{4.22}$$

$$\tilde{\theta}_\mu = \sum_{n=0}^{\infty} \left(\frac{1}{S}\right)^n \tilde{\theta}_{\mu n} \equiv \theta_\mu + \frac{1}{S}\delta\theta_\mu + \mathcal{O}\left(\frac{1}{S^2}\right), \tag{4.23}$$

where $\tilde{\phi}_{\mu 0} \equiv \phi_\mu$, $\tilde{\theta}_{\mu 0} \equiv \theta_\mu$, $\tilde{\phi}_{\mu 1} \equiv \delta\phi_\mu$, $\tilde{\theta}_{\mu 1} \equiv \delta\theta_\mu$ and $\mu = 1, \ldots, N_\mathrm{s}$. After further expanding Eq. (4.21) up to order $S^{1/2}$, we encounter a system of linear equations which can be solved for $\delta\phi_\mu$ and $\delta\theta_\mu$. Their precise expressions, together with a detailed derivation of the linear system for the HK Hamiltonian in a magnetic field, Eq. (4.1), are given in Appendix B.

With the values of $\{\delta\phi_\mu, \delta\theta_\mu\}$, we can compute the magnetization curves from the relation

$$\begin{aligned} m_h &= \frac{1}{N}\sum_{i\mu} \frac{\mathbf{h}}{h} \cdot \langle \mathbf{S}_{i\mu} \rangle \\ &= S\sum_\mu \cos\theta_\mu - \sum_\mu \left(\sin\theta_\mu \delta\theta_\mu + \frac{\cos\theta_\mu}{N} \sum_{\mathbf{k}} \left\langle a^\dagger_{\mathbf{k}\mu} a_{\mathbf{k}\mu} \right\rangle \right) + \mathcal{O}\left(\frac{1}{S}\right), \end{aligned} \tag{4.24}$$

where the expectation values are calculated with respect to the vacuum of the Bogoliubov quasiparticles. By employing Eqs. (3.12), (3.16) and (3.33), we see that

$$\begin{aligned} \sum_{\mathbf{k}} \left\langle a^\dagger_{\mathbf{k}\mu} a_{\mathbf{k}\mu} \right\rangle &= \sum_{\mathbf{k}\lambda} \left\langle \left(\mathbb{X}^*_{\mathbf{k},\lambda\mu} b^\dagger_{\mathbf{k}\lambda} + \mathbb{Y}_{-\mathbf{k},\lambda\mu} b_{-\mathbf{k}\lambda} \right) \left(\mathbb{X}_{\mathbf{k},\lambda\mu} b_{\mathbf{k}\lambda} + \mathbb{Y}^*_{-\mathbf{k},\lambda\mu} b^\dagger_{-\mathbf{k}\lambda} \right) \right\rangle \\ &= \sum_{\mathbf{k}\lambda} \left| \mathbb{Y}_{-\mathbf{k},\lambda\mu} \right|^2 \left\langle b_{-\mathbf{k}\lambda} b^\dagger_{-\mathbf{k}\lambda} \right\rangle = \sum_{\mathbf{k}\lambda} \left| V_{\mathbf{k}\lambda, N_\mathrm{s}+\mu} \right|^2 . \end{aligned} \tag{4.25}$$

Although Eqs. (4.18) and (4.24) are derived from different definitions and even require different levels of calculation within SWT, they must produce identical results, as both consistently include all contributions up to NLO order in $1/S$.[109,112] We have used this nontrivial crosscheck to corroborate all of our calculations which involve corrections to canting angles.

Notably, Eq. (4.24) provides a new way to interpret the plots in Fig. 12. While the second term in parenthesis always leads to a reduction in the magnetization, the first term can be either positive or negative, depending on the sign of $\delta\theta_\mu$. Therefore, an increase in the magnetization can be understood as a consequence of a decrease in the canting angles ($\delta\theta_\mu < 0$), which expresses a tendency for a premature alignment of the spins along the direction of the magnetic field. This supports our claim that the critical field is reduced to a value $h_\mathrm{c} \leq h_{\mathrm{c}0}$ upon the inclusion of quantum fluctuations for the values of φ considered thus far.

Finally, even though the equivalence between Eqs. (4.18) and (4.24) might convey the impression that calculating the corrected parametrization angles is in effect useless, we shall see that this is not the case. Because we are dealing with a semiclassical approximation, the parametrization angles carry special significance and will turn out to be key quantities in the determination of the new values for the critical field.

4.5 Quantum corrections to continuous transition lines: Ordered side

We can now turn to the goal of constructing a consistent $1/S$ expansion for h_c, which will ultimately enable us to investigate the effect of quantum fluctuations on the phase diagram of the model for arbitrary values of S. To start with, we must address the question of what exactly defines the critical field. While this is simply a matter of energy level crossings for first-order phase transitions, the answer is not at all obvious in the case of continuous phase transitions. Thus, let us focus on the latter case for a moment. If we were to base ourselves solely on properties of the ordered phases and on the results for $\varphi = 0$, any of the following, apparently equivalent, defining conditions would seem to fit: (i) the saturation of the magnetization; (ii) the vanishing of quantum fluctuations; (iii) $\cos\tilde{\theta}_\mu\left(h_\mathrm{c}\right) \stackrel{!}{=} 1$ for all spins in the magnetic unit cell, $\mu = 1, \ldots, N_\mathrm{s}$. However, our discussion in Sec. 4.3.3 allows us to rule the first two out immediately, since neither of these properties characterize the polarized phase in the presence of the Kitaev term.

Hence, we move on to the last criterion, which is most intimately connected to a semiclassical picture. In terms of the notation introduced in Sec. 4.4, the condition $\cos\tilde{\theta}_\mu\left(h_\mathrm{c}\right) \stackrel{!}{=} 1$ can be written as

$$1 - \frac{1}{S}\tan\theta_\mu(h_\mathrm{c})\,\delta\theta_\mu(h_\mathrm{c}) + \mathcal{O}\Big(\frac{1}{S^2}\Big) \stackrel{!}{=} \frac{1}{\cos\theta_\mu(h_\mathrm{c})}\,. \tag{4.26}$$

Eq. (4.26) can simplified by noting that all ordered phases which undergo continuous field-induced phase transitions in this study entail uniform canting at the classical level, and are thus characterized by the equation $\cos\theta_\mu \equiv \cos\theta = h/h_{\mathrm{c}0}$ for all μ. With this, we arrive at

$$\frac{1/h_\mathrm{c}}{1/h_{\mathrm{c}0}} = 1 - \frac{1}{S}\tan\theta\,\delta\theta\left(h_{\mathrm{c}0}\right) + \mathcal{O}\left(\frac{1}{S^2}\right), \tag{4.27}$$

which gives a consistent $1/S$ expansion not for h_c, but for $1/h_\mathrm{c}$, provided that the products $\tan\theta\left(h\right)\,\delta\theta_\mu\left(h\right)$ are analytic at $h_{\mathrm{c}0}$ and converge to the same value, $\tan\theta\,\delta\theta\left(h_{\mathrm{c}0}\right)$, for all μ as $h \to h_{\mathrm{c}0}^-$.

At a first glance, it might seem that Eq. (4.27) implies that the NLO contribution to $1/h_\mathrm{c}$ is zero, since $\tan\theta\left(h_{\mathrm{c}0}\right) = 0$. This is indeed what happens for a pure Heisenberg interactions. Nevertheless, as proven analytically for $\mathbf{h} \parallel [001]$ in Appendix B, $\delta\theta\left(h_{\mathrm{c}0}\right)$ actually diverges upon the inclusion of the smallest Kitaev exchange. In fact, it does so in such a way that, except at the Kitaev points $\varphi = \pm\pi/2$, the product $\tan\theta\left(h_{\mathrm{c}0}\right)\,\delta\theta\left(h_{\mathrm{c}0}\right)$ is unique and finite for almost all φ, thus meeting the requirements for the validity of Eq. (4.27). This is further illustrated in Figs. 14 and 17.

Another important observation here is that Eq. (4.27) follows directly from the condition $\cos\tilde{\theta}_\mu\left(h_\mathrm{c}\right) \stackrel{!}{=} 1$, without the need to postulate the existence of a $1/S$ expansion for any specific function of h_c. In this way, $1/h_\mathrm{c}$ emerges as a natural quantity to be considered in this framework. In general, there is of course a one-to-one correspondence

between the expansions of $1/h_c$ and h_c, which can be used to deduce the coefficients of one expansion from those of the other. However, as in any asymptotic series, when explicitly evaluating the truncated series at finite values of S, the numerical values obtained depend on whether one considers the inverse of the expansion of $1/h_c$ or the expansion of h_c itself. In fact, as we shall see below, the results obtained by evaluating the expansion of $1/h_c$ for small values of S turn out to be more consistent with the physical expectation. When computing explicit corrections to the critical field, we therefore evaluate Eq. (4.27) directly, without further solving for h_c.

Finally, we emphasize that, even after assuming that the classical magnetic order is characterized by uniform canting, our formalism allows the corrections to the canting angle to vary between different magnetic sublattices for $h < h_{c0}$. Such a distinction will prove to be important later on, when we deal with a particular manifestation of quantum order-by-disorder in Sec. 4.9.3.

4.6 Quantum corrections to continuous transition lines: Disordered side

As an alternative to the procedure described in Sec. 4.5, one can construct a consistent $1/S$ expansion for $1/h_c$ by applying SWT to the high-field polarized phase. The occurrence of a continuous transition to a symmetry-broken ordered phase is then signaled by the closure of the excitation gap, which expresses the condensation of magnons in the system. Parenthetically, we note that the transition between the high-field polarized phase and a topological $\mathbb{Z}_2$ spin liquid would involve the closure of a vison (flux) gap instead, but this is beyond the scope of a $1/S$ expansion.

While the classical phase boundaries are obtained within LSWT, NLO contributions generally require one to consider both cubic and quartic terms of spin-wave Hamiltonian, Eq. (3.4). Nevertheless, because the classical reference state for the polarized phase is collinear, the cubic part of the spin-wave Hamiltonian is identically zero (see Appendix C for further details), so that we can focus solely on the quartic terms.

Once more, we begin by writing $\mathcal{H}_4$ in normal order,

$$\mathcal{H}_4 = :\mathcal{H}_4: + :\mathcal{H}_4^{(2)}: + \mathcal{H}_4^{(0)}. \tag{4.28}$$

Here, $:\mathcal{H}_4^{(2)}:$ and $\mathcal{H}_4^{(0)}$ represent the (also normal-ordered) quadratic and zero-order contributions which result as a byproduct of bosonic commutation relations. Since $\mathcal{H}_4^{(0)}$ consists of a momentum-independent shift in the ground-state energy and $:\mathcal{H}_4:$ describes magnon decay processes, which only yield corrections beyond NLO in $1/S$,[90,103,113,114] they can both be neglected. At NLO, the $1/S$ expansion is therefore equivalent to a Hartree-Fock approximation in this phase. The quantum corrections to the magnon spectrum thus follow entirely from

$$\mathcal{H}_4^{(2)} = \frac{1}{2}\sum_{\mathbf{k}} \beta_{\mathbf{k}}^\dagger \Sigma_{\mathbf{k}} \beta_{\mathbf{k}}, \tag{4.29}$$

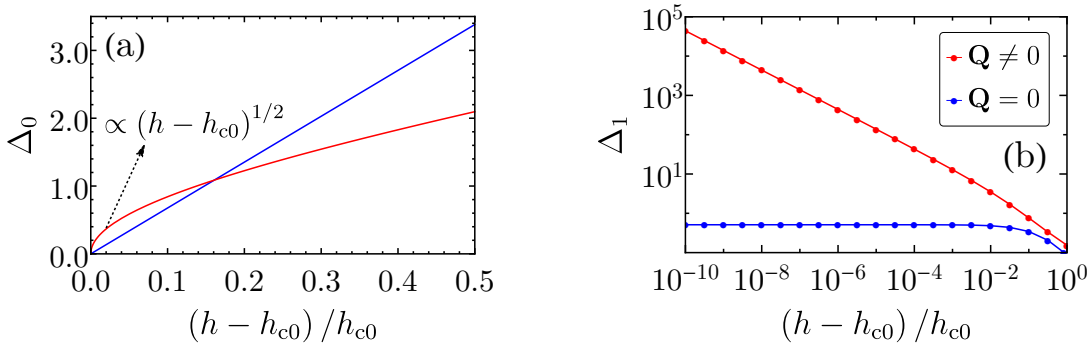

Figure 13 – (a) Leading-order and (b) NLO contributions to the magnon gap of the polarized phase. Although the data were extracted for $\varphi = 0.3\pi$ (blue) and $\varphi = 0.7\pi$ (red) with $\mathbf{h} \parallel [001]$, they represent common qualitative features observed whenever $\mathbf{Q} = \mathbf{0}$ and $\mathbf{Q} \neq \mathbf{0}$, respectively. These incompatible behaviors justify the need for different expansions for $1/h_c$.

Source: By the author.

which differs from $:\mathcal{H}_4^{(2)}:$ by momentum-independent terms. Further details on the calculation of the static self-energy, $\Sigma_{\mathbf{k}}$, and explicit results for $\mathbf{h} \parallel [001]$ are given in Appendix C. After adding Eq. (4.29) to $\mathcal{H}_2$, we arrive at

$$\mathcal{H}_2 + \mathcal{H}_4^{(2)} = \frac{1}{2}\sum_{\mathbf{k}} \beta_{\mathbf{k}}^{\dagger} \left(S\sigma_3\Omega_{\mathbf{k}} + \Sigma_{\mathbf{k}}\right)\beta_{\mathbf{k}}. \tag{4.30}$$

where $\Omega_{\mathbf{k}}$ is given by Eq. (3.18).

The corrected spectrum, $E_{\mathbf{k}\mu}$, is then determined by applying non-degenerate perturbation theory to Eq. (4.30). Because we have expressed the perturbation in terms of the bosons which diagonalize the (unperturbed) LSW Hamiltonian, the result is simply

$$E_{\mathbf{k}\mu} = S\epsilon_{\mathbf{k}\mu} + \Sigma_{\mathbf{k}}^{\mu\mu}. \tag{4.31}$$

Note that only the diagonal elements of $\Sigma_{\mathbf{k}}$ enter the spectrum. Together with the fact that $\Sigma_{\mathbf{k}}$ is Hermitian, this guarantees that $E_{\mathbf{k}\mu}$ is real. For explicit results in the case of $\mathbf{h} \parallel [001]$, see Appendix C.

With this, one can use Eq. (4.31) to read off the first two terms in the $1/S$ expansion of the spin-wave gap

$$\Delta\left(\varphi, \frac{1}{h}, \frac{1}{S}\right) = S\sum_{n=0}^{\infty}\left(\frac{1}{S}\right)^n \Delta_n\left(\varphi, \frac{1}{h}\right). \tag{4.32}$$

By attributing the index $\mu = 1$ to the lower band of the spectrum and denoting the instability wave vector, i.e., the wave vector at which the gap closes at leading order, by $\mathbf{Q} = \mathbf{Q}(\varphi)$, we find that $\Delta_0 \equiv \epsilon_{\mathbf{Q}1}$ and $\Delta_1 \equiv \Sigma_{\mathbf{Q}}^{11}$ for h above, but not too far from, the classical critical field h_{c0}.

Now we are in the position to construct another $1/S$ expansion for $1/h_\mathrm{c}$, based on the criterion $\Delta \to 0$ as $h \to h_\mathrm{c}$. There is but one final caveat to bear in mind: The expansion of a physical observable in the vicinity of a quantum phase transition is well-defined only if the observable itself is analytic at this transition.[115,116] Fig. 13(a) illustrates two different behaviors for the evolution of the gap Δ as a function of the reduced magnetic field $t \equiv (h - h_{\mathrm{c}0})/h_{\mathrm{c}0}$: Above the Néel phase, the gap closes at wave vector $\mathbf{Q} = \mathbf{0}$ and follows $\Delta_0 \propto t$. In contrast, in those cases where the gap closes at $\mathbf{Q} \neq \mathbf{0}$, we have $\Delta_0 \propto t^{1/2}$, so that Δ_0 is not analytic at $h_{\mathrm{c}0}$, but Δ_0^2 is. We thus introduce the notation

$$\frac{1/h_\mathrm{c}}{1/h_{\mathrm{c}0}} = 1 + \sum_{n=1}^{\infty} \left(\frac{1}{S}\right)^n c_n \tag{4.33}$$

and, in the case $\Delta_0 \propto t$, employ the condition

$$\begin{aligned}
\Delta\left(\frac{1}{h_c}\right) \overset{!}{=} 0 \implies & \Delta_0\left(\frac{1}{h_c}\right) + \frac{1}{S}\Delta_1\left(\frac{1}{h_c}\right) + \mathcal{O}\left(\frac{1}{S^2}\right) \overset{!}{=} 0 \\
\implies & \Delta_0\left(\frac{1}{h_{\mathrm{c}0}}\right) + \frac{1}{S}\left[\Delta_1\left(\frac{1}{h_{\mathrm{c}0}}\right) + \left.\frac{\partial\Delta_0}{\partial\,(1/h)}\right|_{\frac{1}{h_{\mathrm{c}0}}} \frac{c_1}{h_{\mathrm{c}0}}\right] + \mathcal{O}\left(\frac{1}{S^2}\right) = 0 \\
\implies & \Delta_0\left(\frac{1}{h_{\mathrm{c}0}}\right) + \frac{1}{S}\left[\Delta_1\left(\frac{1}{h_{\mathrm{c}0}}\right) - \left.\frac{\partial\Delta_0}{\partial h}\right|_{h_{\mathrm{c}0}} h_{\mathrm{c}0}\, c_1\right] + \mathcal{O}\left(\frac{1}{S^2}\right) = 0
\end{aligned} \tag{4.34}$$

to arrive at

$$\frac{1/h_\mathrm{c}}{1/h_{\mathrm{c}0}} = 1 + \left.\frac{1}{S\,h_{\mathrm{c}0}}\frac{\Delta_1}{(\partial\Delta_0/\partial h)}\right|_{h=h_{\mathrm{c}0}} + \mathcal{O}\left(\frac{1}{S^2}\right), \quad \text{for } \mathbf{Q} = 0. \tag{4.35}$$

In the second case, $\Delta_0 \propto t^{1/2}$, we instead expand Δ^2 and use the condition $\Delta^2(1/h_\mathrm{c}) \overset{!}{=} 0$[115,116] to find

$$\frac{1/h_\mathrm{c}}{1/h_{\mathrm{c}0}} = 1 + \left.\frac{2}{S\,h_{\mathrm{c}0}}\frac{\Delta_0\Delta_1}{(\partial\Delta_0^2/\partial h)}\right|_{h=h_{\mathrm{c}0}} + \mathcal{O}\left(\frac{1}{S^2}\right), \quad \text{for } \mathbf{Q} \neq 0. \tag{4.36}$$

Interestingly, the NLO contribution to Eq. (4.36) results from the product of Δ_0, which vanishes at $h_{\mathrm{c}0}$, and Δ_1. Therefore, $1/h_\mathrm{c}$ will only have a correction of order $1/S$ if Δ_1 diverges as $t^{-1/2}$ at criticality. As displayed in Fig. 13(b), this is precisely what happens for $\mathbf{Q} \neq \mathbf{0}$. In contrast, when $\mathbf{Q} = \mathbf{0}$, Fig. 13(b) shows that Δ_1 converges at $h_{\mathrm{c}0}$, supporting the need to employ Eq. (4.35) in this case.

4.7 Quantum corrections to first-order transition lines

So far, we have tackled the issue of how phase boundaries related to continuous transitions change at NLO in $1/S$. We now aim to do the same for discontinuous transitions. In this case, quantum corrections to the phase boundaries follow from a direct comparison between the ground-state energies of competing phases. By noting that Eq. (3.37) gives the complete NLO term in Eq. (3.38) for an arbitrary magnetic order, we thus conclude

that LSWT is sufficient to study the displacement of first-order transition lines, in contrast to the case of continuous transitions.

Consider a point $(\varphi, 1/h) = (\varphi_{\mathrm{t}0}, 1/h_{\mathrm{t}0})$ in parameter space, lying on top of a classical first-order transition line. One way to evaluate the shift in the phase boundary is to compute the quantum correction to $1/h_{\mathrm{t}0}$ while keeping φ fixed. By demanding the equality of the ground-state energies of the phases above (a) and below (b) the transition, $E_{\mathrm{a}}(\varphi_{\mathrm{t}0}, 1/h_{\mathrm{t}}, 1/S) = E_{\mathrm{b}}(\varphi_{\mathrm{t}0}, 1/h_{\mathrm{t}}, 1/S)$, and assuming a $1/S$ expansion for $1/h_{\mathrm{t}}$, we find

$$\frac{1/h_{\mathrm{t}}}{1/h_{\mathrm{t}0}} = 1 + \frac{1}{S\, h_{\mathrm{t}0}} \left.\frac{E_{\mathrm{b}1} - E_{\mathrm{a}1}}{\frac{\partial}{\partial h}(E_{\mathrm{b}0} - E_{\mathrm{a}0})}\right|_{\frac{1}{h_{\mathrm{t}0}}} + \mathcal{O}\Big(\frac{1}{S^2}\Big)\,. \tag{4.37}$$

Conversely, one can also study the displacement of a phase boundary by tracking the change in $\varphi_{\mathrm{t}0}$ for a fixed value of h. The condition $E_{\mathrm{l}}(\varphi_{\mathrm{t}}, 1/h, 1/S) = E_{\mathrm{r}}(\varphi_{\mathrm{t}}, 1/h, 1/S)$, where the subindices denote the ground states to the left (l) and to the right (r) of the transition line, then yields

$$\frac{\varphi_{\mathrm{t}}}{\varphi_{\mathrm{t}0}} = 1 - \frac{1}{S} \left.\frac{E_{\mathrm{l}1} - E_{\mathrm{r}1}}{\frac{\partial}{\partial \varphi}(E_{\mathrm{l}0} - E_{\mathrm{r}0})}\right|_{\varphi_{\mathrm{t}0}} + \mathcal{O}\Big(\frac{1}{S^2}\Big)\,. \tag{4.38}$$

When computing first-order phase boundaries in the φ-h plane in the next sections, we shall alternate between Eqs. (4.37) and (4.38). In general, both schemes are fully equivalent order by order in the expansion. However, when evaluating the truncated series at particular small values of S, the numerical estimates for the phase boundaries can differ. We will use Eq. (4.37) when we wish to compare the displacement of a certain phase boundary with respect to the critical field above it. Eq. (4.38), in turn, will prove most useful in studying horizontal shifts in phase boundaries.

4.8 Results for $\mathbf{h} \parallel [001]$

In this section, we apply the theory presented above to extract concrete results for the HK model in a [001] field. In principle, the fact that we have developed consistent $1/S$ expansions enables us to evaluate phase diagrams for arbitrary values of S. We expect reliable results for large enough S and/or values of φ sufficiently away from the Kitaev limits $\varphi = \pm\pi/2$, where the $1/S$ expansion breaks down below $h_{\mathrm{c}0}$ due to a massive degeneracy of classical ground states.[59,117] In the following, we shall focus primarily on the cases $S = 1/2$, 1, 3/2, and 2. As discussed in Chapter 2, the first three cases might be of relevance for recent and future experiments.[56,57,60,118] The case $S = 2$ already turns out to be quite close to the classical limit $S \to \infty$ qualitatively.[1]

4.8.1 Critical field

Let us begin by discussing the changes in the critical field. In the previous section, we provided two alternatives to evaluate the expansion in Eq. (4.33) up to order $n = 1$. As

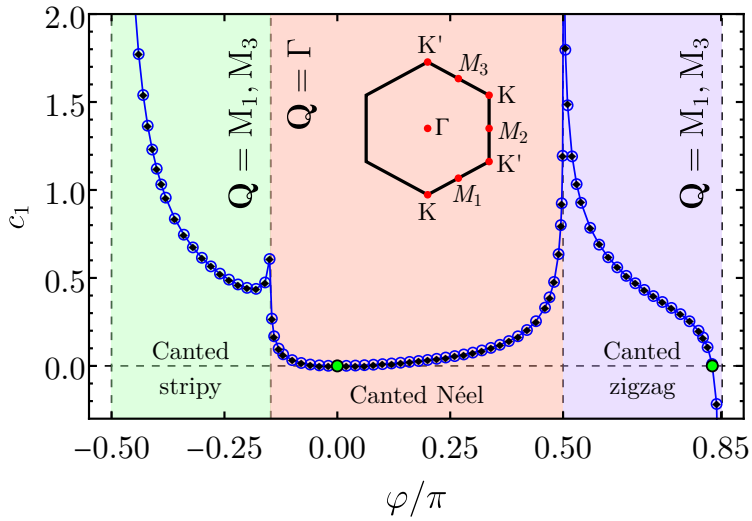

Figure 14 – $\mathcal{O}(1/S)$ coefficient c_1 in the expansion of the inverse of the critical field, Eq. (4.33), as function of φ in a $\mathbf{h} \parallel [001]$ magnetic field. Results obtained by using Eq. (4.27) in the ordered phases (blue open circles) are completely equivalent within our numerical precision to those that follow from applying Eq. (4.35) for instability wave vector $\mathbf{Q} = 0$ and Eq. (4.36) for $\mathbf{Q} \neq 0$ in the disordered phase (black diamonds). The inset shows the locations in the first Brillouin zone of the various instability wave vectors corresponding to different intervals of φ (M_1, M_3, and Γ) and different field directions (K, K′, and M_2). The blue line is a guide to the eye. Green dots at $\varphi = 0$ and $\varphi \approx 0.83\pi$ denote points where the leading-order correction to the critical field vanishes.

Source: By the author.

they were based on distinct physical observables and were derived from different classical reference states, the resulting expressions for c_1 involve apparently unrelated quantities. Yet, after applying both for a range of values of φ in the interval with nonzero $h_{\mathrm{c}0}$, we find that Eq. (4.27) and the combination of Eqs. (4.35) and (4.36) are in fact completely equivalent, as shown in Fig. 14. In addition to confirming the accuracy of our calculations, such an equivalence suggests that one of the methods can be dismissed in favor of the other, even when different field directions are studied. For our purposes, the expansion based on the corrected canting angles turns out to be more convenient, since the application of SWT to ordered phases is at any rate necessary to analyze first-order phase transitions.

Fig. 14 also shows that the corrections to the critical field are finite everywhere except at the Kitaev points, $\varphi = \pm\pi/2$. Nonetheless, we see that c_1 is, if not greater than, often comparable to 1. According to Eq. (4.27), this means that the condition $\tan\theta\,\delta\theta\,(h_{\mathrm{c}0}) \ll S$ seldom holds for small values of S, and hence that the applicability of a $1/S$ expansion for h_{c} is limited, as anticipated in Sec. 4.5.

In fact, a $1/S$ expansion for h_{c} only becomes reliable in the vicinity of two special values of φ for which $c_1 = 0$. One of these is naturally the Heisenberg point, $\varphi = 0$, where

quantum fluctuations vanish for $h \geq h_{c0}$. The other occurs near the edge of the canted zigzag phase, at $\varphi \approx 0.83\pi$. To the best of our knowledge, there is no special symmetry emerging at this point, so that its precise position should shift as higher orders in $1/S$ are considered. However, it marks a change in the sign of c_1, which indicates that the critical field *increases* in a small region to the right of $\varphi \sim 0.83\pi$.

Besides the continuous order-to-disorder phase transitions as functions of field, the classical phase diagram of the HK model in a [001] field has two discontinuous order-to-order transition lines as functions of the interaction parameter φ. Here, we consider only the transition between the canted Néel and stripy states for FM $K < 0$. As the classical boundary is a line of constant φ, we compute the NLO contribution using Eq. (4.38). For the small values of S considered here, we expect the other transition line near the AF Kitaev point at $\varphi = \pi/2$ to be superimposed by a quantum-spin-liquid phase,[68,91,93,97] which cannot be described within a semiclassical formalism such as SWT.[†]

4.8.2 Phase diagrams

The resulting phase diagrams for a field along the [001] direction are shown for different values of S in Fig. 15. There we can see that NLO contributions (solid and dot-dashed lines) lead to substantial quantitative modifications as compared to the classical phase boundaries (light dotted lines). We find pronounced reductions in the critical field in large parts of the phase diagram, especially in the central portion of the canted zigzag and near the triple point separating the canted stripy, canted Néel and polarized phases. Note that the determination of the corrections to the location of this triple point necessarily involves $1/S$ expansions of different observables, leading to the nonmonotonic behavior of the order-disorder transition line visible near $\varphi \approx -0.15\pi$.

Furthermore, the phase diagrams reflect the fact the canted Néel is more stable than the canted stripy by exhibiting a leftward shift in the boundary between both phases. This feature is also observed in numerical studies performed at $h = 0$ for both $S = 1/2$[3,81–83] and $S = 1$.[2] For comparison purposes, we reproduce the 24-site ED and iDMRG results from CHALOUPKA, JACKELI, KHALIULLIN[3] and DONG, SHENG,[2] respectively, as yellow dots in Figs. 15(d) and 15(c). At $h = 0$, our spin-wave calculations show the Néel-stripy transition occurring at $\varphi_t \approx -0.193\pi$ for $S = 1/2$, which is in good quantitative agreement with the ED result $\varphi_t^{\mathrm{ED}} \approx -0.189\pi$. Similar conclusions follow from comparing our estimation to the data obtained in other numerical studies for $S = 1/2$ and $S = 1$. In the latter case, our result $\varphi_t \approx -0.170\pi$ coincides with that from DONG, SHENG[2] up to the third decimal place.

[†] It is possible to estimate the boundary between the ordered phases and the Kitaev spin-liquid within LSWT by studying the vanishing of the ordered moment due to NLO contribution.[82] In this study, however, we focus solely on the boundary between ordered phases.

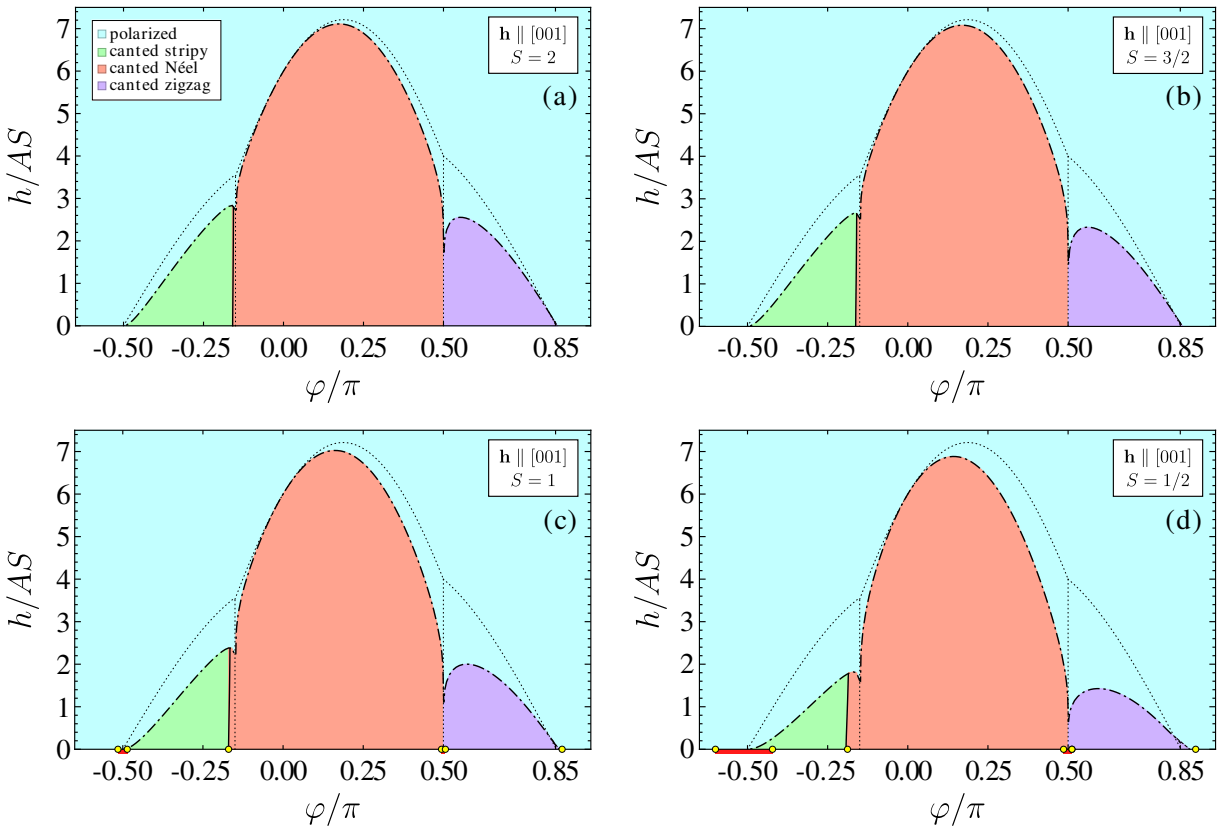

Figure 15 – Phase diagrams of the HK model in a magnetic field $\mathbf{h} \parallel [001]$, derived at NLO in $1/S$ for (a) $S = 2$, (b) $S = 3/2$, (c) $S = 1$, and (d) $S = 1/2$. Dot-dashed and solid lines mark continuous and first-order phase transitions, respectively, whereas the light dotted lines represent the classical phase boundaries, which formally correspond to the limit $S \to \infty$.[1] The yellow dots added to the $S = 1$ and $S = 1/2$ phase diagrams show the $h = 0$ boundaries according to (c) an iDMRG study[2] and (d) 24-site ED results.[3] In both cases, the red stripes below the horizontal axis indicate the domains of spin liquid phases. Note that the AF Kitaev spin liquid near $\varphi = \pi/2$ is expected to cover a sizable field range,[1,4] which is not contemplated by our semiclassical expansion.

Source: By the author.

Finally, we call attention to the rightmost portion of the canted zigzag, where the NLO contributions to $1/h_c$ indicate an increase in the critical field. The validity of the $1/h_c$ expansion there ends as soon as the classical domain of the canted zigzag vanishes. However, this does not imply that the phase boundary with the polarized phase drops abruptly to zero. By extrapolating the curve, one can estimate its intercept with the φ axis to be $\varphi_t \approx 0.880\pi$ for $S = 1/2$, which agrees well with the ED result $\varphi_t^{\mathrm{ED}} \approx 0.900\pi$.[3] In the case of $S = 1$, our calculations yield $\varphi_t = 0.862\pi$, which is once more in good quantitative agreement with the numerical result $\varphi_t^{\mathrm{iDMRG}} \approx 0.87\pi$.

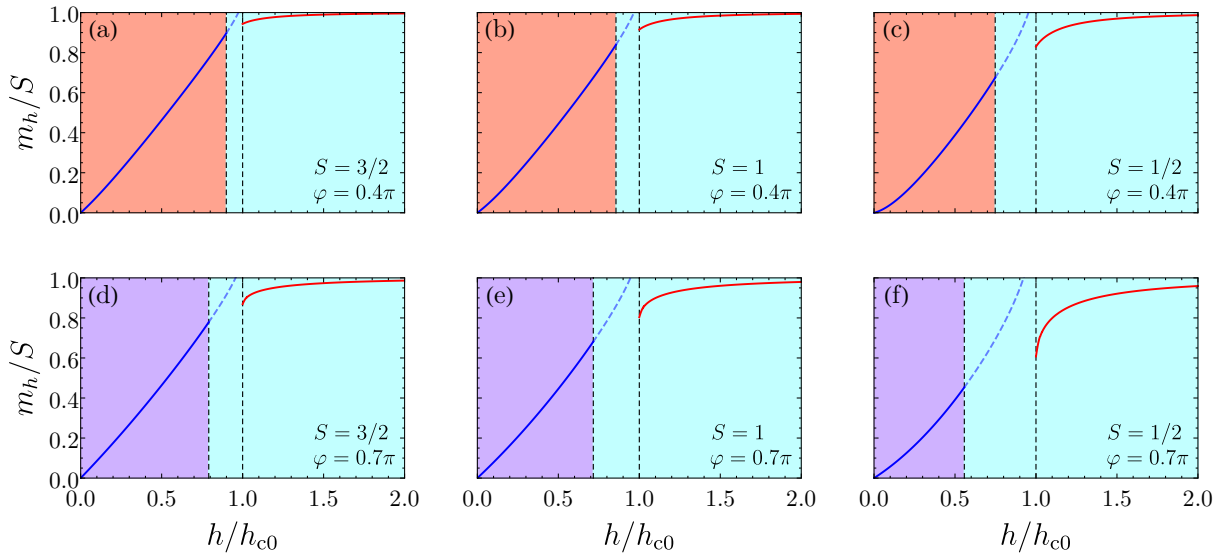

Figure 16 – Magnetization per site m_h in units of S as function of the rescaled field h/h_{c0} at NLO in $1/S$ and for a magnetic field $\mathbf{h} \parallel [001]$. Left panels: $\varphi = 0.4\pi$ above Néel phase for (a) $S = 3/2$, (b) $S = 1$, (c) $S = 1/2$. Right panels: $\varphi = 0.7\pi$ above zigzag phase for (d) $S = 3/2$, (e) $S = 1$, (f) $S = 1/2$. The vertical dashed lines mark the positions of the $1/S$-corrected and classical critical fields, h_c and h_{c0}, respectively. Red curves correspond to the partially polarized phase, whereas blue curves were obtained for the ordered phases below. The dashed portions of the blue curves should therefore be discarded, for they lie in the interval $[h_c, h_{c0}]$, which is now occupied by the partially polarized phase. Still, one cannot extend the red curve below h_{c0}, because the classical polarized state is unstable in this region.

Source: By the author.

4.8.3 Influence on observables: magnetization curves

We further investigate how the changes in the phase boundaries affect field-dependent observables at NLO in $1/S$. In Fig. 16, we combine NLO magnetization curves from above and below h_{c0} with the information on the corrections to $1/h_c$ for $S = 1/2$, 1 and 3/2. Figs. 16(a)-(c) show that the reduction in h_c at $\varphi = 0.4\pi$ eliminates the ill-behaved portion of the magnetization below h_{c0} (dashed lines) and allows one to smoothly interpolate between the polarized and ordered phase down to the smallest values of S. While this tendency remains true for most of the extent of the canted Néel, it breaks down near the Kitaev point, $\varphi = \pi/2$, or for values of φ lying within the range of other ordered phases. As an example, consider the case of $\varphi = 0.7\pi$, illustrated in Figs. 16(d)-(f), for which the canted zigzag appears at low fields. Here, the correction to the magnetization in the limit $h \to h_{c0}^{+}$ is much larger than that observed for $\varphi = 0.4\pi$. Thus, a reasonable interpolation between the low and high-field portions is not possible for small S, despite the substantial reduction in the critical field. One must therefore go beyond NLO in $1/S$ to obtain magnetization curves which are fully consistent in the vicinity of h_c for small values

of S. In fact, we can extend this conclusion to all values of φ covered by the canted zigzag and canted stripy phases, as previous LSW calculations indicate that $1/S$ corrections reduce the $S = 1/2$ magnetization in the limit $h \to h_{c0}^{+}$ by at least $\sim 40\%$ in this entire interval.[1]

4.9 Results for h ∥ [111]

In the previous section, we have seen that our approach provides a consistent way to gauge the stability of the the different ordered phases and capture nontrivial changes in the phase boundaries. We can now move on to the more intricate case of $\mathbf{h} \parallel [111]$. As discussed in Sec. 4.1, we shall restrict our analysis to ordered phases with at most 8 sites per magnetic unit cell. Such a simplification should represent an excellent approximation though, for it only modifies small slivers of the classical phase diagram[1] and incorporates an overall tendency for magnetic orders with large unit cells to be destroyed by quantum fluctuations. Furthermore, this does *not* affect the classical stability of any region of the phase diagram.[119]

4.9.1 Critical field

In Fig. 17, we present the NLO contributions to $1/h_c$ for all of the continuous phase transitions that appear in the semiclassical limit. As in the case of $\mathbf{h} \parallel [001]$, the corrections to the critical field are finite everywhere except at the Kitaev points. Moreover, the results for the canted Néel are roughly similar in both field directions. None of the remaining continuous transitions, however, have a direct counterpart in a [001] field; they involve the two vortex phases presented in Sec. 4.1.3, which emerge at intermediate fields for opposite signs of the Kitaev coupling. On the right-hand side of the diagram ($K > 0$), the AF vortex displays pronounced corrections to $1/h_{c0}$ even away from $\varphi = \pi/2$. On the left-hand side ($K < 0$), the corrections inside the vortex change sign at $\varphi \approx -0.47\pi$ before diverging to $-\infty$ at the FM Kitaev point. Hence, much like the behavior uncovered for the canted zigzag when $\mathbf{h} \parallel [001]$, the critical field should increase near the left end of the vortex phase for every S, which is qualitatively consistent with the early simulations of JIANG *et al.*[67] We note, however, that our semiclassical calculations do not capture the emergence of the Kitaev spin liquid near $\varphi \approx -0.5\pi$ for small values of S.

4.9.2 Phase diagrams

We now combine the results presented above with those extracted for first-order phase transitions to assemble phase diagrams for $S = 1/2$, 1, 3/2, and 2. Similarly to the previous case, we find a substantial reduction of the critical field between the ordered phases and the partially polarized phase upon the inclusion of $1/S$ corrections in large parts of the phase diagram.

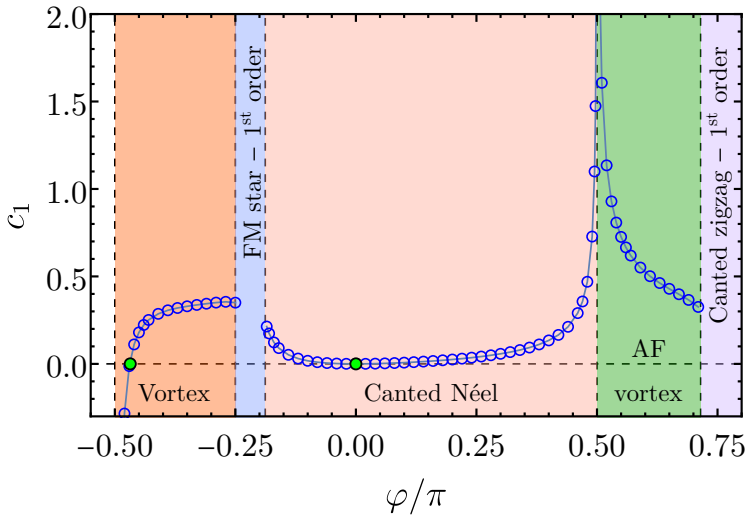

Figure 17 – $\mathcal{O}(1/S)$ coefficient c_1 in the expansion of the inverse of the critical field, Eq. (4.33), as a function of φ in a magnetic field $\mathbf{h} \parallel [111]$, obtained from the spin-wave calculation in the ordered phase [Eq. (4.27)]. The blue line is a guide to the eye. Green dots at $\varphi = 0$ and $\varphi \approx -0.47\pi$ denote points where the leading-order correction to the critical field vanishes. Gaps in the data correspond to intervals of φ in which the transition to the polarized phase is discontinuous.

Source: By the author.

In particular, note that the critical field, represented by dot-dashed lines in Fig. 18, falls below the lower classical boundaries of both vortex phases for nearly their entire extent when $S \leq 1$. While this casts doubt on the stability of such magnetic orders, a conclusive statement requires one to additionally compute shifts in the lower boundaries in a consistent fashion. To this end, we have applied Eq. (4.37), since it presents an expansion of the same quantity, $1/h$, as Eq. (4.27). Then, if the lower boundary is not restored to a position below the corrected critical field, we shall interpret that the polarized phase suppresses the (AF) vortex completely at the corresponding value of φ. Following these premises, we found that NLO contributions to the boundary between the AF vortex and the AF star are not sufficient to override the corrected critical field at any φ unless $S \geq 3/2$. Therefore, the AF vortex vanishes completely for $S \leq 1$ and the polarized phase reaches down to the AF star. On the left-hand side of the diagrams, the sign change of c_1 at $\varphi \approx -0.47\pi$, see Fig. 17, implies that a finite portion of the vortex phase remains stable at NLO in $1/S$. However, because the phase becomes more concentrated around the FM Kitaev point, higher-order corrections in $1/S$ or nonperturbative approaches are necessary to validate its stability for small values of S.

Also by using Eq. (4.37), we verify that the boundary between the FM star and the polarized phase is shifted down and stays connected to the line inherited from the classical boundary between the FM star and the vortex phase. By employing Eq. (4.38) in

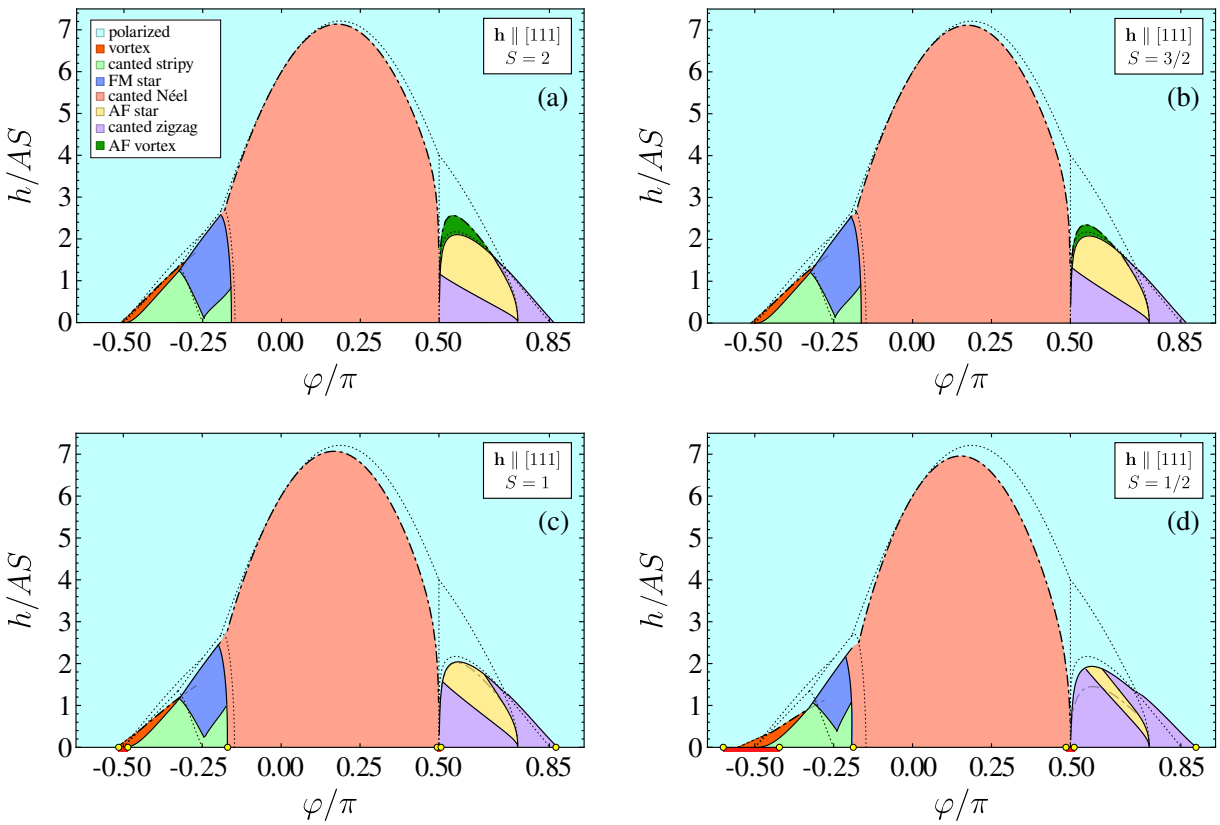

Figure 18 – Phase diagrams of the HK model in a $\mathbf{h} \parallel [111]$ magnetic field, derived at NLO in $1/S$ for (a) $S = 2$, (b) $S = 3/2$, (c) $S = 1$, and (d) $S = 1/2$. Dot-dashed and solid lines mark continuous and first-order phase transitions, respectively, whereas light dotted lines represent the classical phase boundaries, which formally correspond to the limit $S \to \infty$.[1] Note that the dot-dashed lines representing the critical fields fall below the lower classical boundaries of the vortex and AF vortex phases for small S and an increasing range of φ values, leading to a complete disappearance of the AF vortex phase and a strong suppression of the vortex order for $S \leq 1$. The yellow dots added to the $S = 1$ and $S = 1/2$ phase diagrams show the $h = 0$ boundaries according to (c) an iDMRG study[2] and (d) 24-site ED results.[3] In both cases, the red stripes below the horizontal axis indicate the domains of spin liquid phases. Note that the AF Kitaev spin liquid near $\varphi = \pi/2$ is expected to cover a sizable field range,[1,4] which is not contemplated by our semiclassical expansion.

Source: By the author.

turn, we find that the FM star is suppressed by its neighboring ordered phases as well. From its right side, the whole boundary with the canted Néel undergoes a leftward shift. A similar trend is seen from its left side: Except near the transition to the polarized phase, the whole boundary with the canted stripy is displaced to the right. Intriguingly, this displacement increases as one follows the classical phase boundary down to the FM Klein point, $(\varphi, h) = (-\pi/4, 0)$. Nevertheless, one can argue that the FM star cannot reach down to $h = 0$ for any $\varphi \neq -\pi/4$. Indeed, by performing LSW calculations at $h = 0$, we have determined that an ObD mechanism selects the stripy over the FM star everywhere except at the FM Klein point. Therefore, a finite domain of the canted stripy should exist beneath the FM star for every $\varphi \neq -\pi/4$. The extent of such a domain cannot be determined along the lines of Sec. 4.7 though, for $1/h_t$ diverges when $S \to \infty$. As an alternative, we estimate the transition line by expanding the equality $E_{\mathrm{a}}(\varphi, h_{\mathrm{t}}, 1/S) \overset{!}{=} E_{\mathrm{b}}(\varphi, h_{\mathrm{t}}, 1/S)$ around $(h_{\mathrm{t}}, 1/S) = (0, 0)$. Here, the indices correspond to the FM star and canted stripy phases above (a) and below (b), respectively, the transition line. Solving for h_{t}, we obtain

$$h_{\mathrm{t}}(\varphi) = \sqrt{\frac{2}{S}} \sqrt{\left. \frac{E_{\mathrm{a1}} - E_{\mathrm{b1}}}{\frac{\partial^2}{\partial h^2}\left(E_{\mathrm{b0}} - E_{\mathrm{a0}}\right)} \right|_{h=0}} + \mathcal{O}\left(\frac{1}{S}\right), \tag{4.39}$$

which gives the lower boundary of the FM star for $\varphi > -\pi/4$.

On to the opposite side of the diagrams, NLO contributions in $1/S$ computed via Eq. (4.38) favor the canted zigzag over the AF star by moving the boundary between the two to the left. However, the correction to the boundary now vanishes as one approaches the AF Klein point, $(\varphi, h) = (3\pi/4, 0)$. On the other hand, by applying the same scheme as in Eq. (4.39), we find a large suppression of the AF star from below, which is especially drastic for $S = 1/2$. Put together, these results show that the region of stability of the AF star diminishes considerably upon lowering S.

Finally, we turn to the transition between the canted zigzag and the polarized phase. Differently from the case of $\mathbf{h} \parallel [001]$, we observe a rightward displacement of the boundary for all h. This result underlines that the canted zigzag order is particularly stable in a [111] field, as reflected by the large domain it occupies in the diagrams with small values of S, see Fig. 18. Another interesting aspect is that, because we have worked with Eq. (4.38), the corrected phase boundary reaches down to $h = 0$ without the need of an extrapolation. We thus find that the transition between the zigzag and the ferromagnet takes place at $\varphi_{\mathrm{t}} \approx 0.899\pi$ for $S = 1/2$, which is in remarkable agreement with the ED result $\varphi_{\mathrm{t}}^{\mathrm{ED}} \approx 0.900\pi$.[3] For $S = 1$, our estimation $\varphi_{\mathrm{t}} \approx 0.877\pi$ also agrees well with the infinite density renormalization group result $\varphi^{\mathrm{iDMRG}} \approx 0.87\pi$.[2]

In summary, we find a strong suppression at NLO in $1/S$ of the various large-unit-cell and multi-$\mathbf{Q}$ classical phases that arise in the presence of a [111] magnetic field. This generally agrees with the numerical results for $S = 1/2$ and small clusters.[4,67,71,120]

Having addressed the changes in the phase diagram, we now comment on a few extra insights that can be gained by calculating corrections to the classical parametrization angles. We shall see that these corrections have an interesting relation with order-by-disorder effects.

4.9.3 Noncommutativity of the limits $h \to 0$ and $S \to \infty$ in the canted Néel phase

In the previous subsection, we showed that an interesting competition between ObD and field-selection effects is generally at work at low fields. Up to now, we have seen that this can lead to shifts in phase boundaries, as in the transitions between the canted stripy and FM star, and between the canted zigzag and AF star. Yet, it can also produce intriguing responses within the same phase when one considers the evolution of the directions of the ordered moments with the magnetic field. This occurs in the canted Néel, as we discuss below.

Recall that, in Sec. 4.1.1, we have argued that the Néel phase exhibits an accidental SU(2) spin symmetry, which essentially guarantees that the state responds to an arbitrarily oriented magnetic field by performing uniform canting in the classical limit. Quantum corrections, however, lift the SU(2) degeneracy at zero field, and are expected to favor states whose ordered moments lie along the cubic axes in spin-space by virtue of an ObD mechanism.[121,122] Except for specific field directions, the set of states selected by quantum fluctuations will have no overlap with that selected by the field. This leads, in general, to a competition between the fluctuation effects, most relevant at small fields, and field-selection effects, which dominate at high fields.

In Fig. 19(a), we show the quantum corrections to the canting angles in the canted Néel phase in a [111] field for a representative value of φ. On the one hand, we see a divergence of the corrections as $h \to h_{\mathrm{c0}}^{-}$, which we now know is related to the reduction of h_{c}. On the other hand, the plot exhibits two features that distinguish the canted Néel order in a [111] field from all other magnetic orders considered here, including its counterpart in a [001] field. First, NLO corrections in $1/S$ impose a fundamental change to the classical parametrization by rendering the canting nonuniform for every $h < h_{\mathrm{c0}}$. Second, both $\delta\theta_1$ and $\delta\theta_2$ strongly diverge as $h \to 0$. No traces of this low-field divergence, however, appear in observables such as the magnetization, see Fig. 19(b).

As hinted above, the key to understanding such an odd behavior lies in the breaking of the classical SU(2) spin symmetry: An ObD mechanism locks the zero-field Néel order to one of the xyz axes.[122] Since none of the selected states lie on the ab plane, uniform canting in [111] field cannot be reconciled with the presence of quantum fluctuations. This explains not only the difference between $\delta\theta_1$ and $\delta\theta_2$ in Fig. 19(a), but also their divergence at low-fields. Indeed, if it were not so, the corrections would be suppressed at large but finite S. This, however, would be inconsistent with the expectation that the competition

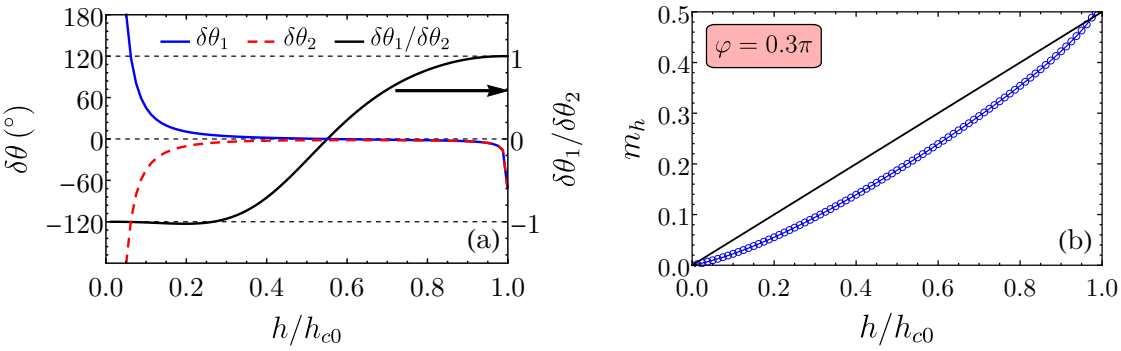

Figure 19 – SWT results for the $\varphi = 0.3\pi$ and $\mathbf{h} \parallel [111]$. (a) Corrections to the classical canting angle for spins in the two sublattices of the canted Néel phase. Although the individual angles diverge in the opposing limits of $h \to 0$ and $h \to h_{c0}$, the ratio of $\delta\theta_1$ to $\delta\theta_2$ shows that the spins tend, respectively, to an antiparallel and a parallel state. (b) Magnetization curves in leading (black) and NLO (blue with markers) order for $S = 1/2$. Note that the divergence of $\delta\theta_1$ and $\delta\theta_2$ as $h \to 0$ does not manifest itself in the magnetization.

Source: By the author.

between fluctuation and field-selection effects should persist for all finite S and sufficiently small fields.

By tracking the ratio of $\delta\theta_1$ to $\delta\theta_2$ rather than their individual values, we can find further information hidden in the low-field divergence. As shown by the black curve in Fig. 19(a), $\delta\theta_1/\delta\theta_2$ converges to -1 as $h \to 0$. Given that $\theta_1 = \theta_2 = \pi/2$ at $h = 0$, this implies that the system still approaches an antiparallel state as $h \to 0$. Therefore, while the $1/S$ expansion fails to connect high- and low-field parametrizations at NLO, it suggests that, for an infinitesimal field, the system orders in a collinear Néel state lying outside of the plane perpendicular to the field axis, in agreement with the outcome of the order-by-disorder mechanism.

Ultimately, one can interpret these results as a sign of noncommutativity of the limits $h \to 0$ and $S \to \infty$ in a [111] field. After all, the classical parametrizations are obtained by taking $S \to \infty$ before $h \to 0$, and are thus completely oblivious to the ObD mechanism which takes place at $h = 0$.

4.9.4 Order-by-disorder in noncollinear phases: Vortex phases

Finally, we comment on the calculations performed in the vortex and AF vortex phases in further detail to illustrate how an order-by-disorder mechanism acts on noncollinear states at higher orders in $1/S$. As described in Sec. 4.1.3, both of these phases display an accidental U(1) symmetry which manifests itself as a free angle, ξ, in their classical parametrizations: $\phi_\mu = \phi_\mu(\xi)$. This means that the leading-order term in the $1/S$ expansion of the azimuthal angles, Eq. (4.22), is not fully fixed by the minimization of the classical

ground-state energy, because, unlike higher-order terms in the spin-wave Hamiltonian, $\mathcal{H}_0 = E_{\mathrm{gs},0}$ does not depend on ξ. The appropriate value of ξ is thus determined by minimizing the contribution of quantum fluctuations to the zero-point energy.

Following the usual prescription of order-by-disorder analyses, we have employed LSWT to compute the NLO contribution to the ground-state energy, Eq. (3.37), as a function of ξ. Fig. 20 shows that the results pertaining to the vortex (AF vortex) are well fitted by a cosine function with a period of $2\pi/3$ ($\pi/3$) and a minimum at $\xi^* = 0$ ($\xi^* = \pi/6$). When these values of ξ are substituted back into the classical parametrizations, they generate 120° orders whose projections onto the ab plane are parallel or perpendicular to the bonds of the lattice.[123] Therefore, the states selected by the leading-order quantum fluctuations are not only noncollinear, but also noncoplanar. We emphasize that, even in cases such as these, the NLO contribution to the ground-state energy follows entirely from LSWT. Indeed, suppose we have computed the $1/S$ corrections, $\delta\phi_\mu$ and $\delta\theta_\mu$, to the parametrization angles. The leading-order contributions of such terms to Eq. (3.38) are then determined by expanding $E_{\mathrm{gs},0}$ and $E_{\mathrm{gs},1}$ around $\{\phi_\mu(\xi^*), \theta_\mu\}$. However, because this set of angles minimizes the classical energy, the NLO term from $E_{\mathrm{gs},0}$ is zero, and Eq. (3.38) only receives contributions beyond those given by LSWT at $\mathcal{O}(S^0)$.[109,112]

Yet, in calculating corrections to the critical field, we have taken the analysis one step further: By using the 120° orders selected within LSWT as reference states [‡] , we have implemented the scheme described in Sec. 4.4 to compute $\delta\phi_\mu$ and $\delta\theta_\mu$. While the corrections to the polar angles, $\delta\theta_\mu$, always turn out to be determinate, we find that the deviations to the azimuthal angles, $\delta\phi_\mu$, cannot be expressed independently in any of the two phases. Instead, they are all given in terms of one of the unknowns, say $\xi' \equiv \delta\phi_1$. In the vortex phase, we have $\delta\phi_\mu = \pm\xi'$, where the upper (lower) sign applies to odd (even) μ, corresponding to the two crystallographic sublattices of the honeycomb lattice. Remarkably, the structure of $\delta\phi_\mu$ in this state is completely analogous to the continuous degeneracy appearing in the classical parametrization,[1] i.e., ξ is simply substituted by ξ'/S in Eq. (4.22). By contrast, the angle corrections in the AF vortex phase introduce an asymmetry between the two crystallographic sublattices, since $\delta\phi_\mu = \xi'$ $[\delta\phi_\mu = -(\xi' + \delta\xi')]$ for odd (even) μ, with $\delta\xi' = \delta\xi'(\varphi, h)$. As ξ' appears in a role similar to the one played by ξ at the level of LSWT, it is to be determined by the minimization of $E_{\mathrm{gs},2}$.

To summarize, for noncollinear states, corrections to the spin angles arising from the cubic terms in the spin-wave Hamiltonian are finite, but do not contribute to the ground-state energy at NLO in the $1/S$ expansion. An accidental continuous degeneracy

‡ We have also attempted to calculate corrections to the parametrization angles by using references states constructed from generic values of ξ, which do not necessarily minimize $E_{\mathrm{gs},1}$. However, for the set of values of ξ we considered, the solution of the linear system that determines $\delta\phi_\mu$ and $\delta\theta_\mu$ was only possible when $\xi = \xi^* \mod 2\pi/3$ and $\xi = \xi^* \mod \pi/3$ in the vortex and AF vortex phases, respectively.

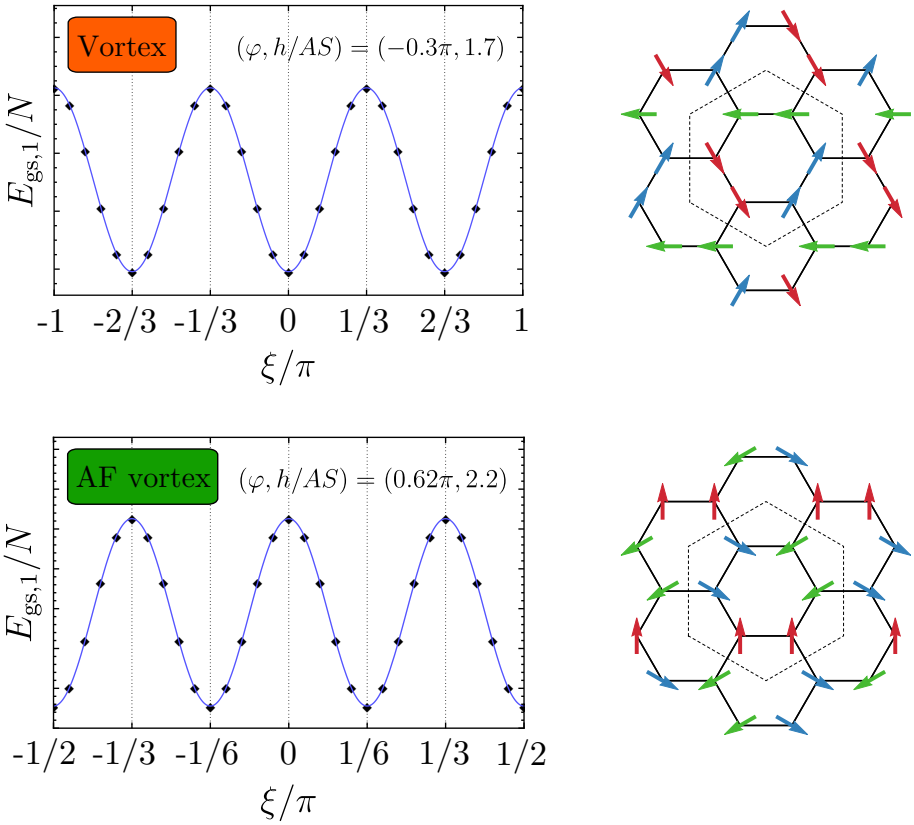

Figure 20 – ObD results for the vortex phases of the HK model in a [111] field derived within LSWT. Left panels: NLO contribution in $1/S$ to the ground-state energies of the vortex and AF vortex phases. The data are well fitted by the functions $\epsilon_q(\delta) = a + b\cos(3\delta)$, with $(a, b) = (-1.6149 \times 10^{-1}, -3.1730 \times 10^{-4})$, and $\epsilon_q(\delta) = a + b\cos(6\delta)$, with $(a, b) = (-1.8485 \times 10^{-1}, 2.351 \times 10^{-5})$. Right panels: Projections of the 120° spin configurations selected by quantum fluctuations onto the honeycomb plane.

Source: By the author.

that occurs at the classical level resurfaces in the $1/S$ corrections to the parametrization angles as a free parameter ξ', which is fixed by minimizing the term of $\mathcal{O}(S^0)$ of the ground-state energy. The resurgence of such a free parameter is therefore necessary to provide the full angle dependence of the energy at higher orders in the $1/S$ expansion. This guarantees that the energy can be determined consistently order by order, and that its minimization fixes the correct values of the spin angles.

4.10 Summary

In the chapter, we have studied the effects of quantum fluctuations in the HK model in an external magnetic field. We have applied nonlinear spin-wave theory both to the ordered and polarized phases to derive a consistent $1/S$ expansion for various observables, allowing us to compute the quantum corrections to the phase diagram at NLO in $1/S$. Our results indicate substantial modifications to the phase boundaries, including an overall

tendency of the high-field polarized phase to suppress ordered phases. This effect was found to be especially strong for the several large-unit-cell and multi-$\mathbf{Q}$ phases that arise in the classical limit for $\mathbf{h} \parallel [111]$.[1] In particular, one of the two magnetic vortex states is completely destabilized for $S \leq 1$, whereas the other is significantly suppressed.

We have also computed explicitly the quantum corrections to different observables, such as the direction of the ordered moments, the magnetization, and the spectrum. Our results for the magnetization curves are consistent with the general trend that the transition from an ordered phase to the partially polarized phase is shifted towards lower fields upon increasing $1/S$. The $1/S$ correction to the critical field can be computed either in the ordered phase, by evaluating the angle corrections to the direction of the ordered moments, or in the partially polarized phase, by tracing the spectral gap. We have explicitly demonstrated that these two, seemingly independent, approaches yield the same results.

5 LOW-TEMPERATURE THERMODYNAMICS IN α-RuCl$_3$

As discussed in Sec. 2.2.5, recent experiments have elevated α-RuCl$_3$ to the status of a prime candidate to realize Kitaev magnetism. However, while there is mounting evidence for the existence of a quantum spin liquid at intermediate field strengths,[44,47,51] clear-cut thermodynamic results indicating a transition between the spin liquid and high-field phase are still scarce. Moreover, as the spin-liquid signatures have not been traced to very low temperatures, they may as well represent a quantum critical regime instead of a stable phase.

In this chapter, we discuss the main results of a project[52] developed in collaboration with Dr. Lukas Janssen and Prof. Matthias Vojta from the Technical University of Dresden, and a group of experimentalists led by Dr. Anja Wolter and Prof. Bernd Büchner from the IFW Dresden. Our purpose was to look for signatures of an intermediate-field quantum spin liquid in a dilatometric study of α-RuCl$_3$. The elastic response of the material was measured for samples exposed to small uniaxial pressure along the direction perpendicular to the honeycomb planes (c^* axis) for temperatures down to 3 K and in-plane magnetic fields $\mu_0\mathbf{H}$ with magnitudes up to 14 T. Differently from previous studies, however, $\mathbf{H}$ was applied parallel to the Ru-Ru bonds (b direction), so as to inhibit the appearance of an additional ordered phase above the zigzag order.[40]

5.1 Overview of experimental results

By tracking changes in the length of the sample along the c^* axis, the team of experimentalists extracted measurements of the linear thermal expansion (TE), α_{c^*}, coefficient and linear magnetostriction (MS), λ_{c^*}. Both of these quantities were computed from raw experimental data by means of the relations

$$\alpha_{c^*} = \frac{\partial}{\partial T}\frac{\Delta L_{c^*}\left(T,\mu_0 H\right)}{L_{c^*}\left(300\,\mathrm{K},0\,\mathrm{T}\right)}, \qquad \lambda_{c^*} = \frac{\partial}{\partial\left(\mu_0 H\right)}\frac{\Delta L_{c^*}\left(T,\mu_0 H\right)}{L_{c^*}\left(300\,\mathrm{K},0\,\mathrm{T}\right)}, \tag{5.1}$$

where ΔL_{c^*} denotes the elongation of the sample along the c^* axis with respect to a reference value obtained at $T = 300$ K and $\mu_0 H = 0$ T.

As a first probe for magnetic phase transitions, consider the low-temperature results for the linear TE coefficient shown in Fig. 21(a). The sharp peak at zero field corresponds to a single phase transition between the ordered zigzag and the paramagnetic phase at $T_N = 7.2(1)$ K. With increasing field, the peak broadens, reduces in magnitude and shifts to lower temperatures, until it disappears at a critical field $\mu_0 H_{\mathrm{c1}} = 7.8(2)$ T. This represents the gradual suppression of the zigzag phase and highlights that the low-T contributions to α_{c^*} are primarily magnetic.

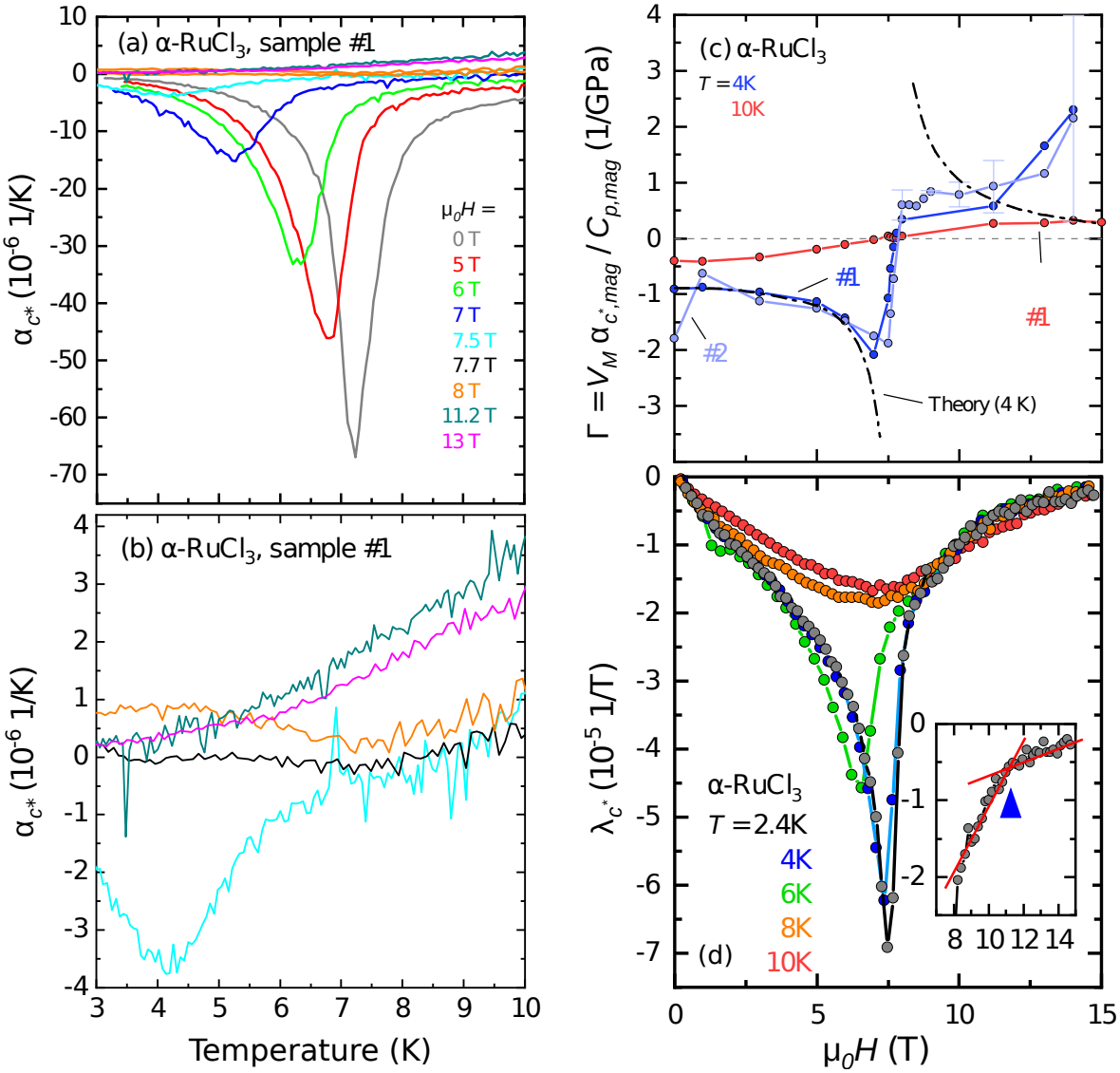

Figure 21 – Experimental results from a dilatometric study on α-$RuCl_3$ in a magnetic field $\mathbf{H} \parallel$ Ru-Ru bonds. (a) Linear TE coefficient along the c^* axis. The sharp peaks represent a transition from the zigzag order to a paramagnetic phase. (b) Zoom of into the data from (a) for fields close to $\mu_0 H_{c1} = 7.8(2)$ T. The anomalous behavior at $\mu_0 H = 8$ T suggests that a distinct intermediate-field regime exists between the zigzag and high-field polarized phases. (c) Grüneisen ratio at 4 K and 10 K for two different samples (#1 and #2) of α-$RuCl_3$. A theoretical curve (dot-dashed lines) corresponding to $T = 4$ K was added to fit the data below $\mu_0 H_{c1}$. Note that the high-field portion of the theoretical prediction differs considerably from the relatively flat Grüneisen ratio found in experiment. (d) Linear magnetostriction along the c^* axis. The inset highlights a kink seen at $\mu_0 H_{c2} \approx 11$ T for sufficiently low temperatures.

Source: Adapted from GASS *et al.*[52]

Fig. 21(b) displays a magnified region of Fig. 21(a) for selected values of $\mu_0 H$. Differently from the low-field data, $\alpha_{c^*}(T)$ is positive and monotonic in the high-field regime $\mu_0 H \gtrsim 11.2$ T. In addition, its magnitude decreases with increasing field, which is consistent with the picture of an increasing magnetic excitation gap of a high-field polarized phase. On the other hand, as one approaches the transition point $H = H_{c1}$ from above, α_{c^*} shows a nonmonotonic dependence in T while remaining positive (see data for $\mu_0 H = 8$ T). As this behavior differs qualitatively both from measurements below H_{c1} and at high fields, it suggests that a distinct intermediate-field regime exists between the zigzag order and the high-field phase. Such a conclusion has also been reached by applying other techniques to study α-$RuCl_3$ in an in-plane $\mathbf{H} \perp$ Ru-Ru bonds.[44,47,51]

As shown in Sec. 5.2.1, the linear TE coefficient is proportional to the derivative of the entropy with respect to uniaxial pressure along the c^* axis. Therefore, the vanishing of α_{c^*} indicates a maximum in the magnetic contribution to the entropy at H_{c1}. Such an entropy accumulation is predicted to occur near a continuous quantum phase transition[124,125] and can be identified experimentally by measuring the Grüneisen ratio $\Gamma = V_M \alpha / C_p$, where α and C_p are the magnetic contributions to the volumetric TE coefficient and the specific heat at constant hydrostatic pressure, respectively, and $V_M \simeq 55.9$ cm^3/mol is the molar volume of α-$RuCl_3$.[5–7] Upon approaching a quantum critical point (QCP), Γ changes sign along with α_{c^*} as a result of entropy accumulation in the quantum critical regime.[125] Further, if the QCP is driven by pressure, then Γ displays characteristic divergences.[124]

When applying this concept to α-$RuCl_3$, we note that phase transitions in the material can be driven either by a magnetic field or by pressure. Consequently, both the field and pressure derivatives of the entropy will display sign changes, which makes Γ a suitable probe to detect QCPs. Second, for a qualitative analysis, we calculate Γ by using the linear c^* axis TE coefficient α_{c^*} instead of its volumetric counterpart α, since α_{c^*} is much larger compared to that along the other directions.[126]

Specific-heat measurements performed on the same α-$RuCl_3$ crystals led to the Grüneisen ratio results presented in Fig. 21(c). The low-T data show that $\Gamma(H)$ becomes largest in magnitude right below H_{c1}, where it changes sign as expected. The low-field behavior is thus consistent with quantum critical phenomenology.[125] When combined with the fact that $\Gamma(T)$ does not change sign for $T > T_N$,[52] this implies the occurrence of a continuous quantum phase transition at H_{c1}, in agreement with a previous analysis on low-T specific heat results.[8] The low-T data for $\Gamma(H)$, however, show no appreciable dependence on the field in the interval $8\ \text{T} \leq \mu_0 H \leq 11$ T above H_{c1}. As a result, $\Gamma(H)$ is rather asymmetric around the critical field, Fig. 21(c).

While indicative of a intermediate-field regime, the previous observables fail to determine the magnitude of $\mu_0 H$ at which a transition (or crossover) to the high-field polarized phase takes place. Measurements of λ_{c^*} were then performed with the aim of

solving this issue. The results displayed in Fig. 21(d) show that, in addition to a sharp peak marking a continuous phase transition from the zigzag phase, the low-temperature linear MS exhibits a kink above H_{c1}, as highlighted in the inset. Upon increasing temperature, the position of this kink does not vary significantly around the value $\mu_0 H_{c2} \approx 11\,\mathrm{T}$ observed for $T = 2.4\,\mathrm{K}$, but its magnitude gradually decreases until it vanishes at $T \approx 8$ K. These observations are in line with the existence of an additional low-temperature quantum regime whose field width remains finite at the very low temperatures and should therefore be distinguished from the narrow quantum critical regime near H_{c1} and the semiclassical partially polarized regime above H_{c2}.

The main goal of the theoretical work described in this chapter was then to verify whether the anomalies observed in experiment could be explained by means of a semiclassical analysis.

5.2 Theoretical modeling

Following the lines of Sec. 2.2.5, we model the thermodynamic behavior of α-RuCl$_3$ by employing the Hamiltonian

$$\begin{aligned}\mathcal{H}'_{\mathrm{JK\Gamma J_3}} = \mathcal{H}_{\mathrm{JK\Gamma J_3}} + \mathcal{H}_{\mathrm{Z}} = \sum_{\langle ij\rangle} \left[J_1 \mathbf{S}_i \cdot \mathbf{S}_j + K_1 S_i^\gamma S_j^\gamma + \Gamma_1 \left(S_i^\alpha S_j^\beta + S_i^\beta S_j^\alpha \right) \right] \\ + \sum_{\langle\langle\langle ij\rangle\rangle\rangle} J_3 \mathbf{S}_i \cdot \mathbf{S}_j - g\mu_{\mathrm{B}}\mu_0 \mathbf{H} \cdot \sum_i \mathbf{S}_i \end{aligned} \tag{5.2}$$

with $\mathbf{H} \parallel \left[\bar{1}10\right]$ and $g \equiv g_{ab}$ being the in-plane g factor. Possible trigonal distortions spoiling C_3^* symmetry are therefore neglected along with the additional Γ' off-diagonal couplings shown in Eq. (2.15).

5.2.1 Linear thermal expansion and magnetostriction

Because our goal is to calculate changes of the sample length along the c^* axis, we must find a way to model the *linear* TE coefficient and the MS rather than their volumetric counterparts. Given the anisotropy of the α-RuCl$_3$ crystal and the high sensitivity of the magnetic couplings to its structure, it is therefore important to also distinguish uniaxial from hydrostatic pressure. Keeping this in mind, we begin our thermodynamic analysis by writing down the differential of the free energy

$$dF = -SdT + \int d^3r \sigma_{ij} d\eta_{ij} - g\mu_0\mu_{\mathrm{B}} M dH. \tag{5.3}$$

Here, S denotes the entropy, $g\mu_{\mathrm{B}} M = g\mu_{\mathrm{B}} \sum_i (\mathbf{S}_i \cdot \mathbf{H}/H)$ is the uniform magnetization and σ_{ij} and η_{ij} are the stress and strain tensors, respectively. To gain an idea of the meaning of the last two, one can imagine a cubic volume element $\delta\Omega$ of the *undeformed* solid. By definition, the stress tensor σ_{ij} expresses the force per unit area in the i direction that the surrounding medium exerts on the surface of $\delta\Omega$ which is normal to the j direction. If

the force is directed toward the outside (inside) of the $\delta\Omega$, then σ_{ij} is positive (negative).* Meanwhile, the strain tensor η_{ij} is related to the displacement each point on the surface of $\delta\Omega$ experiences with respect to its center in response to the external force. As such, the spatial integral in Eq. (5.3) goes over the volume of the undeformed crystal.[127,128]

Now, we may refine our description by taking the C_3^* symmetry of our model into account. This property implies that, under homogeneous stress, the system has only two independent length changes, namely of ℓ_{c^*} along the c^* axis and ℓ_{ab} perpendicular to it. Furthermore, it guarantees that the symmetric tensor η_{ij} becomes diagonal in a coordinate system with one axis parallel to $\mathbf{c}^*$. Thus, if we assume that stress is homogeneous throughout the sample and that the C_3^* symmetry is preserved under small uniaxial pressure, we may rewrite Eq. (5.3) in a simpler form:

$$dF = -SdT + V\sigma_i d\eta_i - g\mu_0\mu_{\mathrm{B}} M dH, \tag{5.4}$$

where V denotes the volume of the undeformed crystal, and we employ the shorthand notations $\eta_i \equiv \eta_{ii}$ and $\sigma_i \equiv \sigma_{ii}$. Each diagonal strain element η_i then encodes information about the elongation along the i-th principal axis, such that $d\eta_i = d\ln\ell_i$.[127,129] In the following, we shall identify $i = 3$ with the c^* direction.

Under these conditions, one can use Maxwell relations derived from the potential $G = F - V\sigma_i\eta_i$ to find

$$\alpha_{c^*} = \left(\frac{\partial \ln \ell_{c^*}}{\partial T}\right)_{\sigma,H} = -\frac{1}{V}\frac{\partial}{\partial T}\left(\frac{\partial G}{\partial \sigma_{c^*}}\right)_{\sigma',T,H} = \frac{1}{V}\left(\frac{\partial S}{\partial \sigma_c^*}\right)_{\sigma',T,H}, \tag{5.5}$$

$$\lambda_{c^*} = \left[\frac{\partial \ln \ell_{c^*}}{\partial (\mu_0 H)}\right]_{\sigma,T} = -\frac{1}{V}\frac{\partial}{\partial (\mu_0 H)}\left(\frac{\partial G}{\partial \sigma_{c^*}}\right)_{\sigma',T,H} = \frac{\mu_{\mathrm{B}}}{V}\left[\frac{\partial (gM)}{\partial \sigma_{c^*}}\right]_{\sigma',T,h}. \tag{5.6}$$

The σ' which appears above serves as a reminder that all stresses but σ_{c^*} are to be held constant in carrying out the derivatives.

However, because our model is two-dimensional, we have no means to calculate σ_{c^*} and thus cannot compute the observables directly from Eqs. (5.5) and (5.6). Instead, we must consider how uniaxial stress along c^* affects the microscopic parameters $\mathcal{J} \in \{J_1, K_1, \Gamma_1, J_3, g\}$ contained in the Hamiltonian, Eq. (5.2). This leads to

$$\alpha_{c^*} = \frac{1}{V}\sum_{\mathcal{J}} \frac{\partial S}{\partial \mathcal{J}}\frac{\partial \mathcal{J}}{\partial \sigma_{c^*}}, \qquad \lambda_{c^*} = \frac{\mu_{\mathrm{B}}}{V}\sum_{\mathcal{J}} \frac{\partial (gM)}{\partial \mathcal{J}}\frac{\partial \mathcal{J}}{\partial \sigma_{c^*}}. \tag{5.7}$$

5.2.2 Pressure dependence of the model parameters

As illustrated in Eq. (5.7), the sensitivity of each microscopic parameter to stress plays a key role in determining α_c^* and λ_c^*. For small distortions, we may evaluate $\mathcal{J}$ as an expansion up to first order in σ_{c^*}

$$\mathcal{J}(\sigma_{c^*}) \approx \mathcal{J}_0\left[1 + n_{\mathcal{J}}(\sigma_{c^*} - \sigma_0)\right], \tag{5.8}$$

* Note that this convention is opposite to that which defines pressure.

where σ_0 represents ambient stress and $\mathcal{J}_0$ is the corresponding unperturbed value of the model parameter. We have also defined

$$n_{\mathcal{J}} := \frac{1}{\mathcal{J}_0} \frac{\partial \mathcal{J}}{\partial \sigma_{c^*}}\bigg|_{\sigma_{c^*}=\sigma_0} . \tag{5.9}$$

A positive $n_{\mathcal{J}}$ therefore means that the absolute value of $\mathcal{J}$ increases in response to increasing tensile stress σ_{c^*} (i.e., decreasing uniaxial pressure along c^*).

Since the microscopic interactions in α-RuCl$_3$ are extremely sensitive to bond lengths and angles,[19] the pressure dependence of the exchange couplings is not easily modeled. Given the present lack of comprehensive *ab initio* information, we treat the several $n_{\mathcal{J}}$ as free parameters, which we shall adjust with the goal of reproducing the main features of the experimental results in regimes where LSWT is expected to be reliable.

5.2.3 Calculating thermodynamic observables from spin-wave theory

Having established a connection between stress along the c^* axis and the magnetic properties of the system, we must now compute the free energy in order to complete our thermodynamic analysis. In the following, we outline how to do so within LSWT. While this noninteracting-boson approach can be applied to both the ordered and the polarized high-field phases, it is expected to be reliable when the number of magnon excitations is small. This requirement is not met (i) at low fields for temperatures comparable to or above the Néel temperature and (ii) at high fields for temperatures comparable or above the magnon gap. By noting that the latter condition includes the quantum critical regime near H_{c1}, we choose to ignore a correction to the critical field coming from the theory of Chapter 4. Such a simplifying assumption should not affect the validity of our conclusions, provided that we analyze results for fields sufficiently distant from H_{c1}.

As a starting point, one must select a classical spin configuration that minimizes $\mathcal{H}'_{\mathrm{JK\Gamma J_3}}$. This problem has already been addressed in a previous study involving the same conditions we consider here.[87] Similarly to the HK model, the C_3^* symmetry of the Hamiltonian at zero field leads to a threefold degeneracy of the classical ground state in terms of different zigzag patterns. However, a $[\bar{1}10]$ field lifts such a degeneracy by selecting the configuration with zigzag chains running perpendicularly to it. This happens because the corresponding zero-field order is normal to the b axis, so that the spins cant uniformly in response to the magnetic field.[60] Canting increases until the critical field, H_{c1}, is reached and a continuous transition from the canted zigzag to a polarized state takes place.

Following the procedure described in Chapter 3, one can assemble the LSW Hamiltonian, $\mathcal{H}_{\mathrm{LSW}}$, and diagonalize it by means of a Bogoliubov transformation. Here, this step was performed analytically in the polarized phase, but required a numerical approach for $H < H_{c1}$. The eigenenergies $\varepsilon_{\mathbf{k}\nu} \equiv S\epsilon_{\mathbf{k}\nu}$, where $S = 1/2$ is now the spin size,

then provide all the necessary information to compute the free energy for a system of noninteracting bosons such as ours. From basic quantum thermodynamics, we have[61]

$$F = S^2 E_{\mathrm{gs},0} + S E_{\mathrm{gs},1} + k_{\mathrm{B}} T \sum_{\mathbf{k}\nu} \ln\left(1 - e^{-\beta\varepsilon_{\mathbf{k}\nu}}\right), \tag{5.10}$$

where $\beta = 1/(k_{\mathrm{B}}T)$ as usual. Then, by combining Eqs. (5.7) and (5.10), we find

$$\alpha_{c^*} = -\frac{1}{k_{\mathrm{B}}T^2 V} \sum_{\mathcal{J}} \mathcal{J}_0 n_{\mathcal{J}} \sum_{\mathbf{k}\nu} \frac{e^{\beta\varepsilon_{\mathbf{k}\nu}} \varepsilon_{\mathbf{k}\nu}}{\left(e^{\beta\varepsilon_{\mathbf{k}\nu}} - 1\right)^2} \frac{\partial \varepsilon_{\mathbf{k}\nu}}{\partial \mathcal{J}} \tag{5.11}$$

and

$$\lambda_{c^*} = -\sum_{\mathcal{J}} \frac{\mathcal{J}_0 n_{\mathcal{J}}}{\mu_0 V} \left\{ N \frac{\partial^2}{\partial \mathcal{J} \partial H} \left(E_{\mathrm{gs},0} - \frac{\mathrm{Tr}\mathbb{A}_{\mathbf{k}}}{2N_{\mathrm{s}}} \right) + \sum_{\mathbf{k}\nu} \left[\left(\frac{1}{2} + \frac{1}{e^{\beta\varepsilon_{\mathbf{k}\nu}} - 1} \right) \frac{\partial^2 \varepsilon_{\mathbf{k}\nu}}{\partial \mathcal{J} \partial H} \right.\right.$$
$$\left.\left. - \frac{\beta e^{\beta\varepsilon_{\mathbf{k}\nu}}}{\left(e^{\beta\varepsilon_{\mathbf{k}\nu}} - 1\right)^2} \frac{\partial \varepsilon_{\mathbf{k}\nu}}{\partial H} \frac{\partial \varepsilon_{\mathbf{k}\nu}}{\partial \mathcal{J}} \right] \right\}. \tag{5.12}$$

Note that, in order to get Eq. (5.12), we have used the fact that $\mathrm{Tr}\mathbb{A}_{\mathbf{k}}$ is momentum-independent for the phases we consider here. Another noteworthy point is that both α_{c^*} and λ_{c^*} are given as a linear combination of terms which result from varying one microscopic parameter at a time. While this does not hold beyond the approximation expressed by Eq. (5.8), it allowed us to analyze an arbitrarily wide range of sets $\{n_{\mathcal{J}}\}$ without demanding extra computational time.

A third quantity of interest is the magnetic heat capacity at constant strain,

$$C_\eta(T, H) = T \left(\frac{\partial S}{\partial T} \right)_\eta = \frac{1}{k_{\mathrm{B}} T^2} \sum_{\mathbf{k}\nu} \frac{e^{\beta\varepsilon_{\mathbf{k}\nu}} \varepsilon_{\mathbf{k}\nu}^2}{\left(e^{\beta\varepsilon_{\mathbf{k}\nu}} - 1\right)^2}. \tag{5.13}$$

In the following, we will compare α_{c^*}/C_η to the Grüneisen ratio measured in the experiments, even though both observables are not strictly equal. That is because the Grüneisen ratio measured in experiment corresponds to the ratio between the linear TE coefficient and the heat capacity at constant stress rather than constant strain. Still, we shall simply refer to α/C_η as the Grüneisen ratio from now on for simplicity.

5.2.4 Parameter sets

The reference values $\mathcal{J}_0$ for the coupling constants were set as in Eq. (2.18), with the global energy scale adjusted to $A = 4.31$ meV. This guarantees that, for $g = 2.8$,[33] the classical critical field of the model coincides with the value $\mu_0 H_{\mathrm{c1}} = 7.8$ T found in experiment. As for the pressure dependence of the exchange couplings, we chose to normalize all $n_{\mathcal{J}}$ with respect to $n_{\Gamma_1} > 0$ in order to work with dimensionless parameters. In this way, n_{Γ_1} represents an overall fitting factor which can be determined by matching the theoretical results to experimental data. As shown in Fig. 22(c), a good fit is obtained for $n_{\Gamma_1} = 0.9$ GPa^{-1}.

As a first trial, we looked into a scenario where uniaxial pressure would affect all exchange couplings, but not the g factor. Then, we adjusted the remaining free parameters to reproduce as many qualitative features from the experimental data as possible, regarding both the TE and the MS measurements. This approach yielded the set of coefficients labeled as set 1 in Table 3. However, as we shall explain in the next section, our magnetostriction results motivated us to consider a second scenario, whereby we removed the constraint $n_g = 0$. As a result, we arrived at set 2 of Table 3.

Before proceeding, we note that both sets 1 and 2 predict that the absolute values of all exchange couplings decrease with increasing pressure along the c^* axis. Although the intricate nature of the quantum chemistry behind the model prevents a clear judgment on how reasonable such an observation is, a previous *ab initio* study has suggested the same trend after considering a similar model for α-$RuCl_3$.[130]

5.3 Theoretical results

5.3.1 Linear thermal expansion coefficient

Let us begin by discussing our TE results, which are shown in Fig. 22(a,b). Both sets of coefficients presented in Table 3 reproduce gross features of the experimental data, such as: (i) α_{c^*} is negative for $H < H_{c1}$ and positive for $H > H_{c1}$; (ii) the magnitude of α_{c^*} is markedly smaller for $\mu_0 H \gtrsim 11$ T than for $\mu_0 H \lesssim 7$ T; (iii) at sufficiently high fields, α_{c^*} is suppressed by further increasing H. Moreover, set 1 leads to the correct field trend in the zigzag phase, whereby the magnitude of α_{c^*} becomes larger as one increases H at a fixed temperature. Set 2 only does so approximately, since the trend is spoiled near zero field. We recall that LSWT does not capture the thermal phase transition at T_N, hence a corresponding peak in $\alpha_c^*(T)$ is missing, and a comparison between experiment and theory should be restricted to $T < T_N$.

Upon analyzing different combinations of the coefficients $n_{\mathcal{J}}$, we were unable to obtain a reasonable agreement with experiment without considering a fairly large $n_{J_3} > 0$. This observation suggests that uniaxial pressure along the c^* axis *destabilizes* the zigzag phase, since this particular type of magnetic ordering is favored by a positive J_3. We also

Table 3 – Different sets of expansion coefficients $n_{\mathcal{J}}$ describing the pressure dependence of the model parameters, see Eq. (5.9). The value of n_{Γ_1} is used as reference scale, as described in the text.

	n_{J_1}/n_{Γ_1}	n_{K_1}/n_{Γ_1}	n_{J_3}/n_{Γ_1}	n_g/n_{Γ_1}
Set 1	0.3	0.3	1.6	0.0
Set 2	0.5	0.75	0.56	-0.65

Source: By the author.

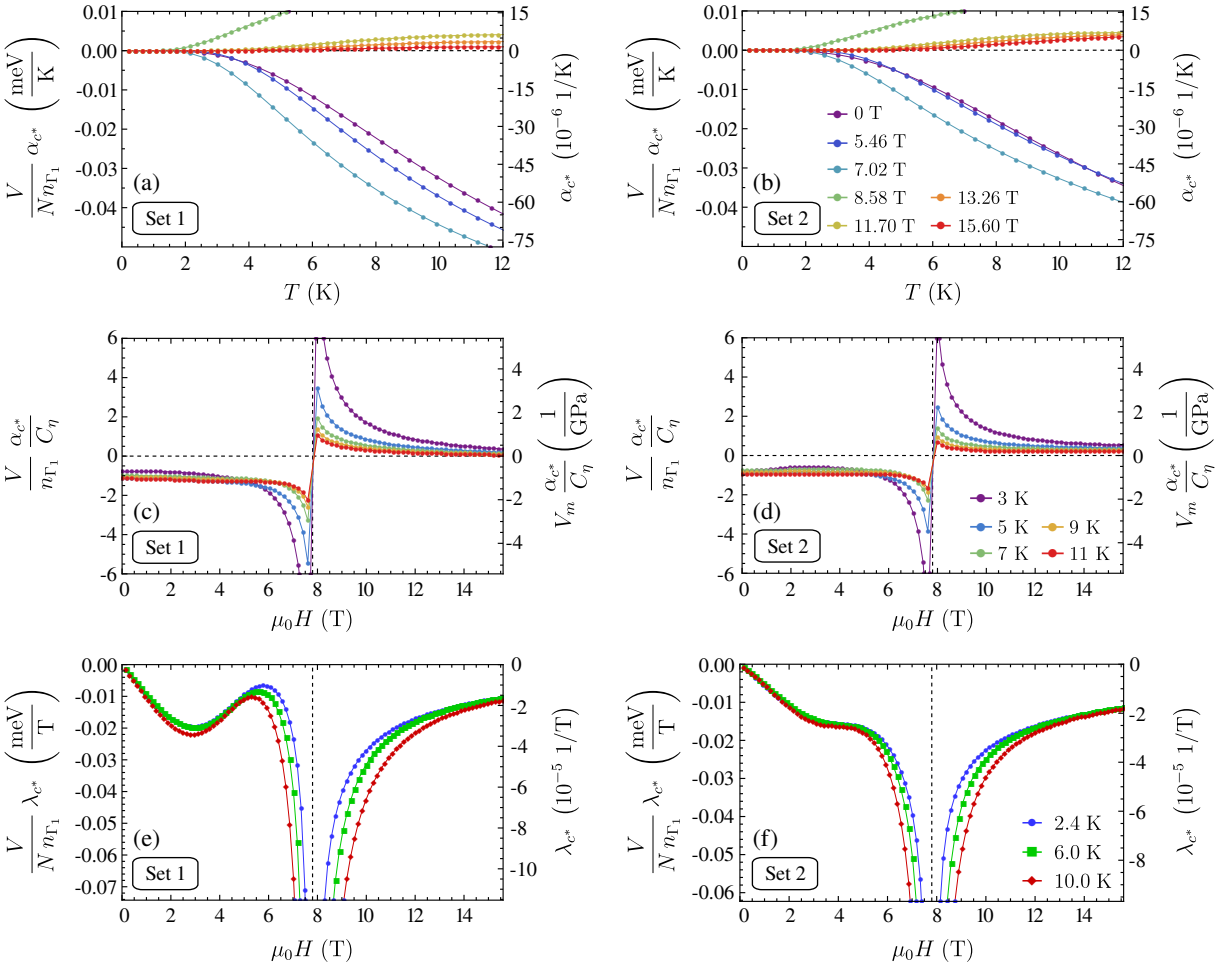

Figure 22 – LSWT results for the (a,b) linear TE coefficient, (c,d) Grüneisen ratio and (e,f) linear MS for the two sets of parameters given in Table 3. In the plots where the independent variable is the magnetic field, the vertical gridline represents the critical field, $\mu_0 H_{c1} = 7.8$ T. In all panels, the left vertical axis gives the theory result normalized to n_{Γ_1}, whereas the right vertical axis shows experimental units using $n_{\Gamma_1} = 0.9$ GPa^{-1} and $V/N = 92.8$ Å^3.[5–7] Our semiclassical analysis does not show any of the features interpreted as signatures of a novel phase at intermediate fields above H_{c1} and thus supports its genuine quantum character.

Source: Adapted from GASS *et al.*[52]

point out that the correct field evolution for $H < H_{c1}$ requires a large $n_{\Gamma_1} > 0$. Increasing n_{K_1} and n_{J_1} tends to cancel this trend and even produce negative values for α_{c^*} in the polarized phase at temperatures above than 15 K.

With that said, we emphasize that neither set 1 nor set 2, nor any other combination of coefficients we considered reproduces the nonmonotonic behavior of $\alpha_{c^*}(T)$ reported in experiment for fields slightly above H_{c1}. Instead, we generally find that α_{c^*} increases monotonically at a fixed temperature as $H \to H_{c1}^+$.

5.3.2 Grüneisen ratio

Next, we discuss the evolution of the Grüneisen ratio as a function of the magnetic field. The results presented in Fig. 22(c,d) show the correct signs above and below H_{c1}, as we have enforced this by a careful analysis of the TE data.

Close to H_{c1}, magnon excitations proliferate and the approximation of noninteracting bosons becomes inadequate. Hence, the evolution of α_{c^*} and α_{c^*}/C_η across the critical field cannot be reliably computed in our approach. On general grounds,[125] we expect both quantities to evolve smoothly at fixed finite T as function of H, crossing zero near H_{c1}. On the other hand, as mentioned above, we do expect our calculations to yield qualitatively correct results at sufficiently high fields and low temperatures, where the magnon excitation gap is comparable to or larger than $k_B T$. However, when the theoretical result for α_{c^*}/C_η at $T = 4K$ is superimposed on the corresponding experimental data for $\Gamma(H)$, see Fig. 21(c), we spot a significant difference: Although the match at low fields is convincing, the anomaly of the measured Γ above H_{c1} does not appear to be compatible with a semiclassical picture given by LSWT. This suggests an interpretation in terms of a genuine quantum regime at intermediate fields.

5.3.3 Linear magnetostriction

Moving on to the linear MS results shown in Fig. 22(e,f), we see that both sets of coefficients correctly produce negative values of λ_{c^*} for the whole range of magnetic fields considered here. However, set 1 notably leads to large nonmonotonic variations around an inflection point in the zigzag phase which are not observed in experiment. The origin of such a behavior can be traced back to the highly nontrivial evolution of magnon gap with the magnetic field, which is illustrated in Fig. 23. When trying to reduce the intensity of this feature in λ_{c^*}, we verified that it becomes even larger if one, for instance, decreases n_{K_1}. In fact, without considering variations in g, we were unable to find a parameter set capable of smoothing out such a contortion while preserving the main characteristics of α_{c^*}. As far as we could check, this is only accomplished by taking $n_g < 0$, which motivated us to consider the second set of coefficients.

When inspecting Fig. 22, one can see that $\lambda_{c^*}(H)$ displays a singularity at the same $\mu_0 H_{c1} = 7.8$ T for all three temperatures, including $T = 10$ K, which is larger than the Néel temperature measured in experiment. This happens because LSWT does not produce critical behavior at $T_N = 7.2$ K.

In regard to the behavior for $H > H_{c1}$, our results do not bear any resemblance to the kink found in experiment. Together with the absence of a nonmonotonic behavior in α_{c^*} around 8 T and the lack of the asymmetric, anomalous Grüneisen ratio above H_{c1}, this suggests that the physics in the regime between H_{c1} and H_{c2} cannot be fully accounted for by a continuous field-induced opening of a magnon gap, and therefore supports the

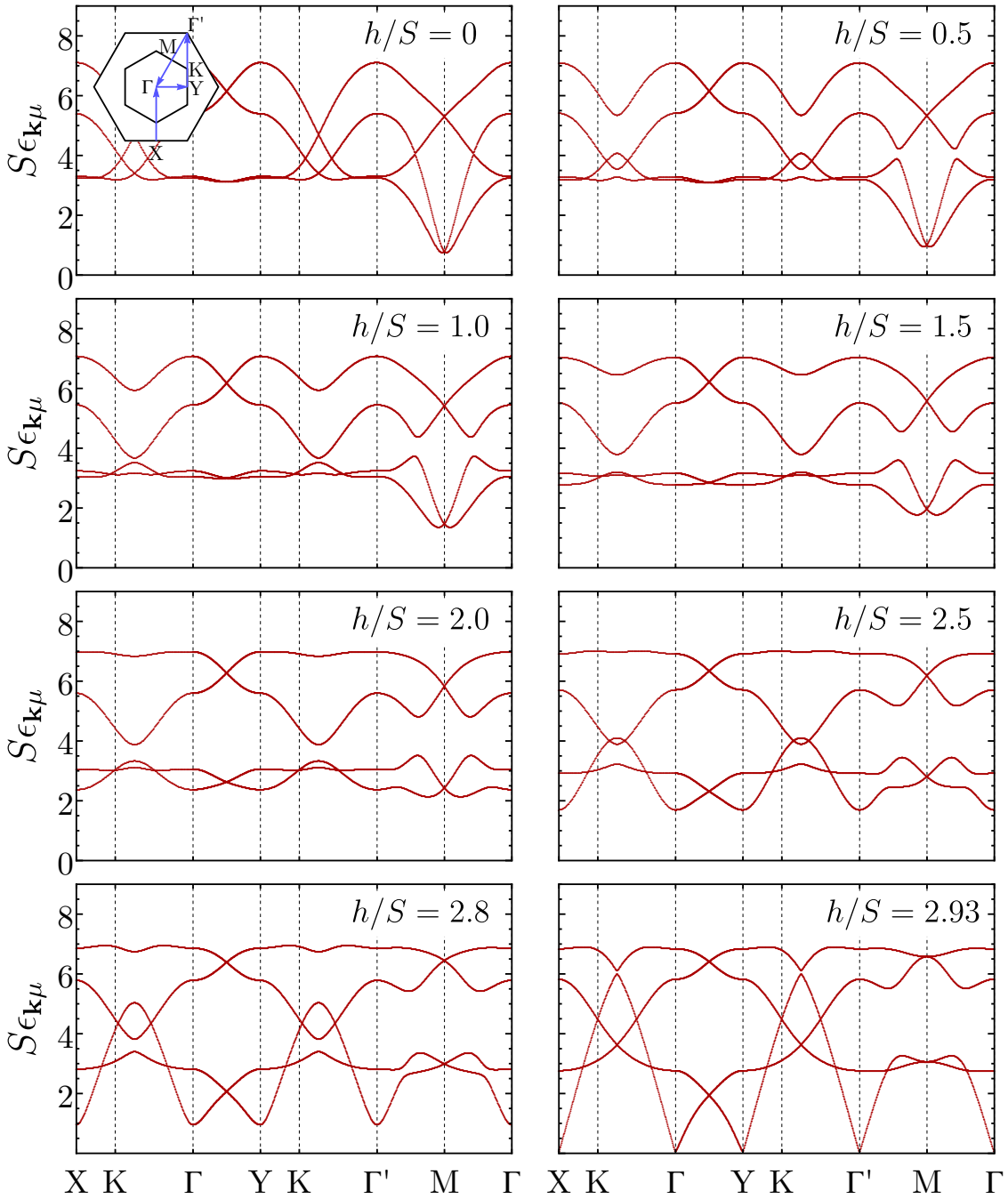

Figure 23 – Linear spin-wave spectrum of $\mathcal{H}'_{\mathrm{JK\Gamma J_3}}$, Eq. (5.2), as a function of $h = \mu_0 \mu_{\mathrm{B}} g H$ with the coupling constants of Eq. (2.18) and $g = 2.8$. In these units, $h/S = 2.93$ corresponds to $\mu_0 H = 7.8$ T. The path in reciprocal space runs over the first and second Brillouin zones, as shown in the inset. We note that the nontrivial evolution of the gap is the origin of a shoulder in the magnetostriction results of Fig. 22.

Source: By the author.

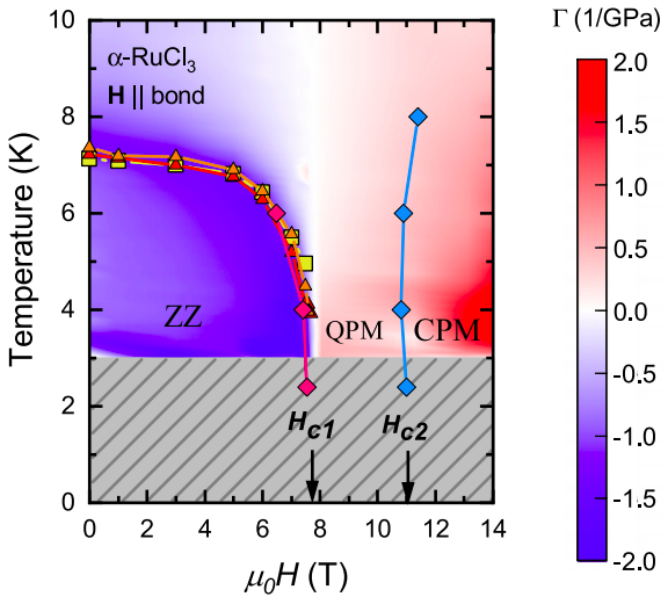

Figure 24 – $T - H$ phase diagram proposed for α-$RuCl_3$ with $\mathbf{H} \parallel$ Ru-Ru bonds. Yellow squares were extracted from peaks in the heat capacity at constant pressure,[8] whereas triangles and diamonds correspond to TE and MS measurements, respectively. The color scale illustrates the variation of the Grüneisen ratio across the diagram down to $T = 3$ K. In addition to the zigzag order (ZZ) at low fields and the semiclassical paramagnet (CPM) at high fields, our analysis supports the existence of a third regime at low temperatures, which has been identified as a quantum paramagnet (QPM). The field-driven transition at H_{c1} is continuous, while the one at H_{c2} is either a crossover or a weak first-order transition.

Source: GASS *et al.*[52]

interpretation of the experimental data as evidence for a novel quantum regime above H_{c1} at low temperatures.

5.4 Discussion

The experimental and theoretical results discussed above motivated the construction of a temperature-field phase diagram for α-$RuCl_3$ in a magnetic field $\mathbf{H} \parallel$ Ru-Ru bonds.[52] As depicted in Fig. 24, three distinct low-temperature regimes were identified: (i) a phase with long-range zigzag order for fields below $\mu_0 H_{c1} = 7.8(2)$ T (ZZ), (ii) an intermediate quantum paramagnetic regime between $\mu_0 H_{c1}$ and $\mu_0 H_{c2} \approx 11$ T (QPM), and (iii) a semiclassical paramagnetic state with a gapped magnon spectrum and partially polarized spins for fields above $\mu_0 H_{c2}$ (CPM).

In GASS *et al.*,[52] we speculate that the QPM regime might represent a topological quantum spin liquid, as claimed by the recent thermal Hall effect studies.[44,51] This phase cannot be distinguished from the CPM high-field phase on the basis of symmetry and hence does not need to be bounded from above by a thermal phase transition. The Grüneisen

ratio measurements allow us to draw a left boundary which reaches down to the QCP $\mu_0 H_{c1} = 7.8\,(2)$ T and $T = 0$. On the other hand, the absence of quantum critical behavior in $\Gamma\,(H)$ near H_{c2} rules out the possibility a second-order phase transition at higher fields. The QPM and CPM regimes should therefore be separated by either a crossover or a weak first-order transition. In the latter case, one should expect the transition line at H_{c2} to terminate at a critical endpoint at finite temperature, as represented by the blue line in Fig. 24.

6 EXACT DIAGONALIZATION APPLIED TO THE HEISENBERG-KITAEV MODEL

In this chapter, we discuss ED results we have obtained for the $S = 1/2$ HK model in magnetic fields applied in the [001] and [111] directions. While our main goal is to establish a comparison with our nonlinear spin-wave theory results from Chapter 4, we also inspect the stability of the GSL phase to increasing values of $|J|$. In doing so, we arrive at a result that might point toward a novel quantum tricritical point.

6.1 Methods

Before implementing the proper ED routine for the HK model, Eq. (4.1), it is necessary to define a *cluster*, i.e. a finite version of the system whose properties one wishes to investigate. Clearly, this entails setting up the geometrical arrangement of N sites by translating the unit cell of the lattice through vectors $\mathbf{T}(n_1, n_2) = n_1\mathbf{a}_1 + n_2\mathbf{a}_2$, where $\mathbf{a}_1$ and $\mathbf{a}_2$ are primitive vectors and $n_i \in \{0, 1, \ldots, L_i\} \subset \mathbb{Z}$. In addition, one has to specify the boundary conditions of the system to fully determine the interactions involving each of the N sites. In the following, we present results obtained by taking $\mathbf{a}_1 = \left(\sqrt{3}/2, 3/2\right)$ and $\mathbf{a}_2 = (0, 3)$ with $L_1 = 6$ and $L_2 = 2$. Under periodic boundary conditions, this choice results in the 24-site cluster represented in Fig. 25, which preserves the threefold rotational symmetry of the honeycomb lattice. Having determined the cluster and boundary conditions, we can implement our ED code in two separate steps.

The first step is to construct the Hamiltonian of the system. However, this is generally not achieved by a direct approach, since the exponential growth of the Hilbert

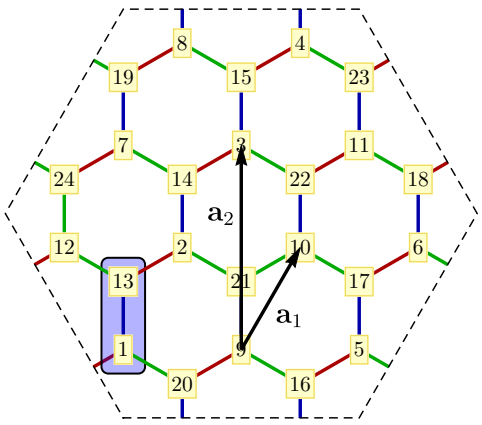

Figure 25 – 24-site cluster used in the ED calculations. Each site in the lattice is mapped back onto itself by six translations along the $\mathbf{a}_1$ vector or two translations along $\mathbf{a}_2$. The blue rectangle encloses the unit cell of the cluster.

Source: By the author.

space with N causes systems with sizes as small as $N = 24$ to exceed the memory capacity of modern computers. Thus, one usually uses symmetries of the Hamiltonian to work in subspaces with reduced dimensions and to enable the treatment of larger systems. Here, we exploit the translational invariance of Eq. (4.1) to operate in a subspace of momentum $\mathbf{k}$ of our choice. After building a basis of this subspace,[131] we compute the matrices corresponding to each of the three terms of $\mathcal{H}'_{\mathrm{HK}}$ stripped of the parameters J, K and h, and store the results in separate unformatted text files. Given that the process of constructing the matrices can be a significantly time-consuming, carrying it out only once is of extreme convenience, even when dealing with moderate-size clusters such as ours.

The second step consists of adding the three different matrices for a given set of parameters J, K and h, and later diagonalizing the combined matrix. To this end, we have applied the Lanczos algorithm,[131] which essentially reduces the computational cost of the process by only providing information for the ground state and the first few excited states.

After repeating the procedure summarized above for a series of values of φ and h, we found that the ground state $|\psi\rangle$ of the cluster in depicted in Fig. 25 generally belongs to the momentum sector $\mathbf{k} = (0, 0)$*. With the goal of identifying phase transitions, we used this information to calculate two quantities: The second derivative of the ground-state energy with respect to a control parameter r and the ground-state *fidelity*[4]

$$f(r) = |\langle \psi(r + dr) \,|\, \psi(r) \rangle| \,. \tag{6.1}$$

The latter measures the overlap between the ground states at r and $r + dr$, with dr being an arbitrarily small increment. In this sense, sharp peaks in the fidelity tend to indicate first-order phase transitions, whereas continuous phase transitions are typically associated with smooth peaks.

For the most part, our results were derived by taking $r = h$, i.e., by performing scans at constant φ. Besides being more convenient for the purpose of determining critical fields, this approach is also faster, since it saves time by combining the heavier J and K matrices only once per scan. When choosing $r = h$, we have further computed the total magnetization, Nm_h, of the system, both by taking the first derivative of the ground-state energy and by evaluating the expectation value $\frac{\mathbf{h}}{h} \cdot \sum_i \langle \psi \,|\, \mathbf{S}_i \,|\, \psi \rangle$, which follows directly from the field matrix. As expected, these two methods were always found to be completely equivalent.

6.2 Results for h ∥ [001]

Let us begin by analyzing the results obtained at the AF Heisenberg point, $\varphi = 0$. In Figs. 26(a-c), we see that both the second derivative of the ground-state energy and the fidelity exhibit a series of sharp peaks as a function of h, whereas the magnetization

* This is the largest of the momentum sectors and has a total of 1399176 basis states.

increases in steps. However, rather than indicating the occurrence of multiple phase transitions, these features simply reflect the finite size of the system. Indeed, the fact that the total magnetization is a conserved quantity of Heisenberg Hamiltonians implies that, for each value of h, the ground state must have a definite magnetization

$$Nm_h = 2nS, \quad \text{with} \quad n \in \{0, 1, \ldots, N/2\}\,, \tag{6.2}$$

which are precisely the values of m_h appearing in Fig. 26(c) for $N = 24$. If computational limitations did not impose restrictions on the size of the system, we would thus see the magnetization plateaus grow in number while reducing in width upon increasing N. This trend would persist until the plateaus merged into a continuous curve in the thermodynamic limit $N \to \infty$. Therefore, all of the peaks in Figs. 26(a,b) would disappear, except the one marking the transition to the polarized phase at $h/AS = 6$. This peak certainly survives the thermodynamic limit because the positive curvature of the magnetization curve (see Sec. 4.3.3) necessarily leads to a cusp at the critical field.

In Figs. 26(d-f), we find a similar behavior for $\varphi = 0.3\pi$. Two clear differences, however, can be spotted by inspecting Fig. 26(f): (i) The magnetization does not saturate after the last transition and (ii) the plateaus are no longer flat, as their slope increases with h (more visible at higher fields). Both of these observations are consistent with the fact that the total magnetization ceases to be a conserved quantity of the Hamiltonian in the presence of a nonzero Kitaev term. Still, the conclusion that all peaks in Figs. 26(d,e) but the last are washed out in the thermodynamic limit continues to apply, and we are left with a single continuous phase transition at $h/AS \approx 6.49$.

As one moves further away from $\varphi = 0$, the magnetization plateaus become steeper and less separated from each other, until they begin to merge near the AF Kitaev point. In particular, Fig. 26(i) shows that the $\varphi = 0.5\pi$ magnetization curve has a single discontinuity at $h/AS \approx 1.22$, in agreement with NASU *et al.*[74] Yet, as shown Figs. 26(g,h), the second derivative of ground-state energy and the fidelity both present a smaller peak at $h/AS \approx 1.29$ (the peak near $h = 0$ in the fidelity is likely to be spurious). If the latter is interpreted as a transition to the polarized phase, then one could argue that the results suggest the existence of an intermediate-field phase. This is precisely the conclusion reached in a previous ED study,[70] wherein the intermediate phase was identified as a GSL covering a significantly larger interval of h than the one found here. Such a discrepancy, however, is not symptomatic of an error, but rather follows from the use of inequivalent 24-site clusters (see the supplemental material of RONQUILLO; VENGAL; TRIVEDI[70]). Given the sensitive dependence of the location of the phase boundaries to the geometry of the cluster, it would be desirable to have a future DMRG study search for signatures of the intermediate-field phase in larger systems. An alternative method that may also yield helpful insights is cluster mean-field theory.[82]

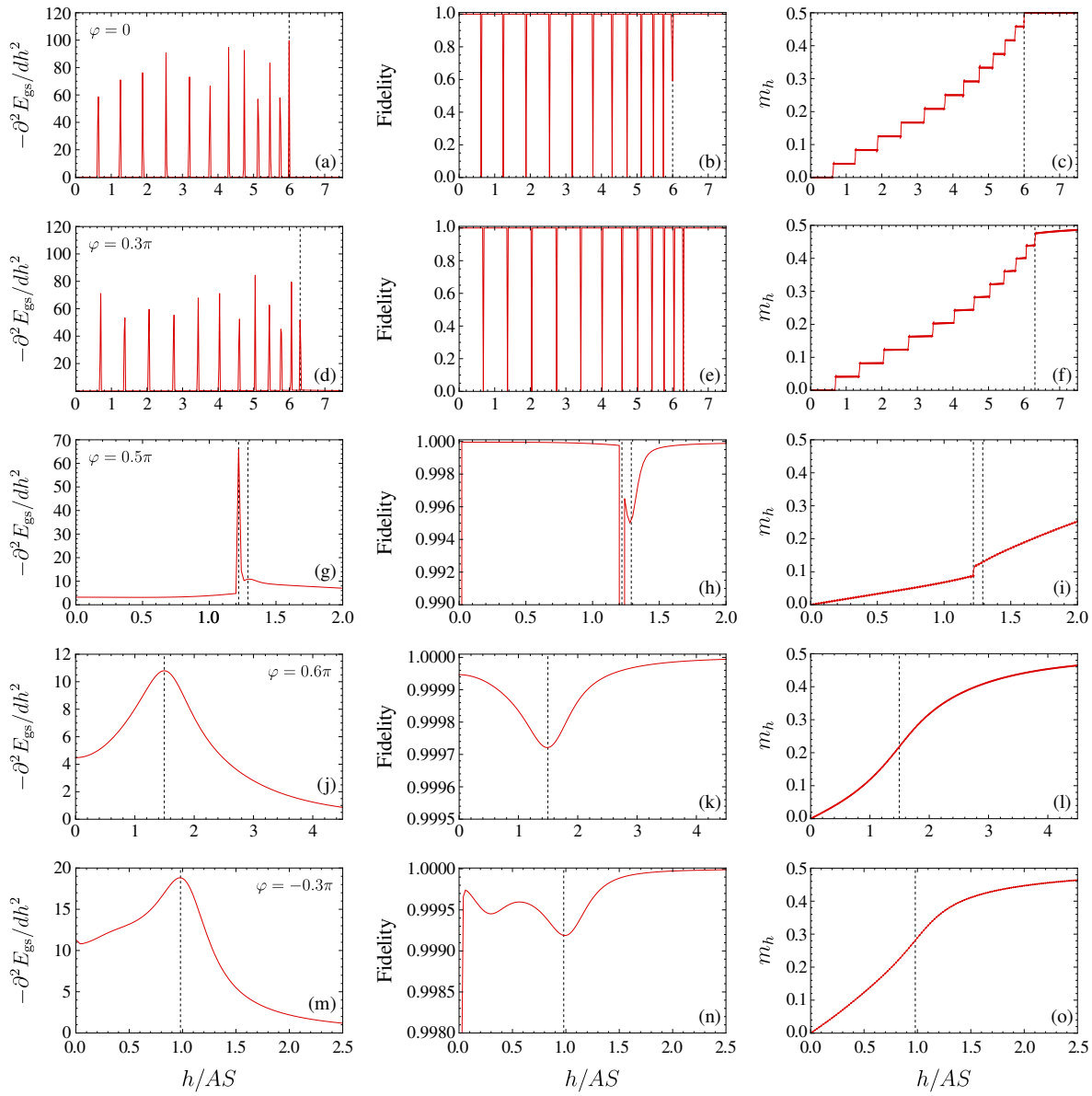

Figure 26 – 24-site ED results for the HK model in a magnetic field $\mathbf{h} \parallel [001]$ with (a-c) $\varphi = 0$, (d-f) $\varphi = 0.3\pi$, (g-i) $\varphi = 0.5\pi$, (j-l) $\varphi = 0.6\pi$ and (m-o) $\varphi = -0.3\pi$. A is a global energy scale related to the coupling constants by $J = A\cos\varphi$ and $K = 2A\sin\varphi$, where $S = 1/2$ is the spin size. Left: The opposite of the second derivative of the ground state energies with respect to the magnetic field. Middle: The fidelity, Eq. (6.1). Right: The magnetization per site in the direction of the magnetic field.

Source: By the author.

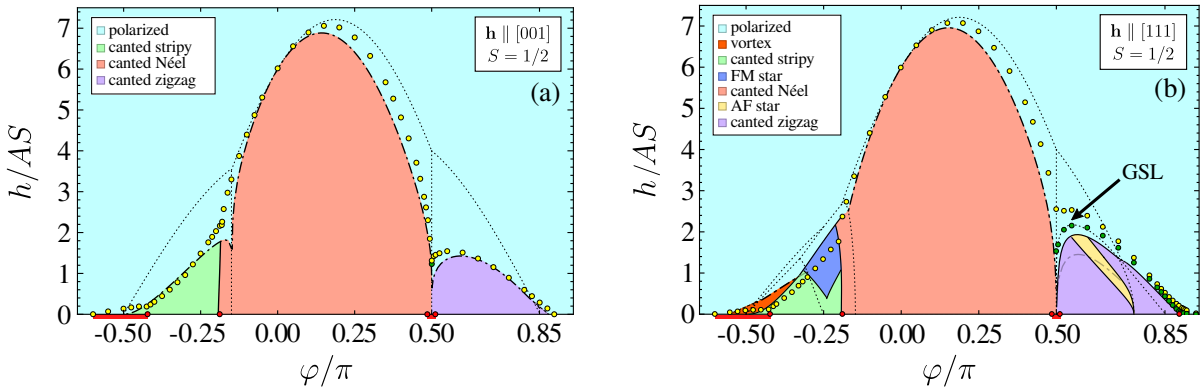

Figure 27 – 24-site ED results (dots) superimposed with the $S = 1/2$ phase diagrams of the HK model derived at NLO in $1/S$ for a magnetic field (a) $\mathbf{h} \parallel [001]$ and (b) $\mathbf{h} \parallel [111]$, see Figs. 15 and 18. Yellow dots indicate the last field-induced transition at a given value of φ, green dots mark the lower boundary of a possible intermediate-field GSL phase and red dots signal results obtained at zero field. Red stripes below the horizontal axis highlight the domain of spin liquid phases at $h = 0$.

Source: By the author.

Past the AF Kitaev point, we find completely continuous magnetization curves. This is what happens, for instance, at $\varphi = 0.6\pi$, see Fig. 26(l). Since we know from Sec. 2.2.2 that the system is in the zigzag phase at zero field, the single smooth peak in Figs. 26(j,k) can only indicate a direct continuous transition to the polarized phase.

The situation turns out not be as simple when we analyze values of φ belonging to the domain of the stripy phase. As illustrated in Figs. 26(m,n), besides a well-defined peak at $h/AS \approx 0.98$, two features appear at lower fields. The sharp peak in the fidelity near $h = 0$, in particular, is related to an abrupt growth in the magnitude of the Bragg peaks characterizing the two stripy patterns selected by the [001] field. We did not encounter, on the other hand, signs in the static structure factor capable of explaining the intermediate-field peak in Fig. 26(n).

After applying similar analyses for different values of φ, we arrived at the results compiled in Fig. 27(a). We do not show data points below the critical fields, however, because secondary features such as those in Figs. 26(j-k) intermingle with the signatures of phase transitions and render the precise identification of intermediate-field phase boundaries difficult. Still, the selected ED data set allows us to establish a comparison with our nonlinear spin-wave theory results from Chapter 4. Overall, we find that both methods are good agreement, which reasserts the consistency of the semiclassical approach. Further, we verify that Heisenberg couplings $|J| \approx 0.04\,|K|$ are already sufficient to destabilize the possible intermediate-field phase for the cluster in Fig. 25.

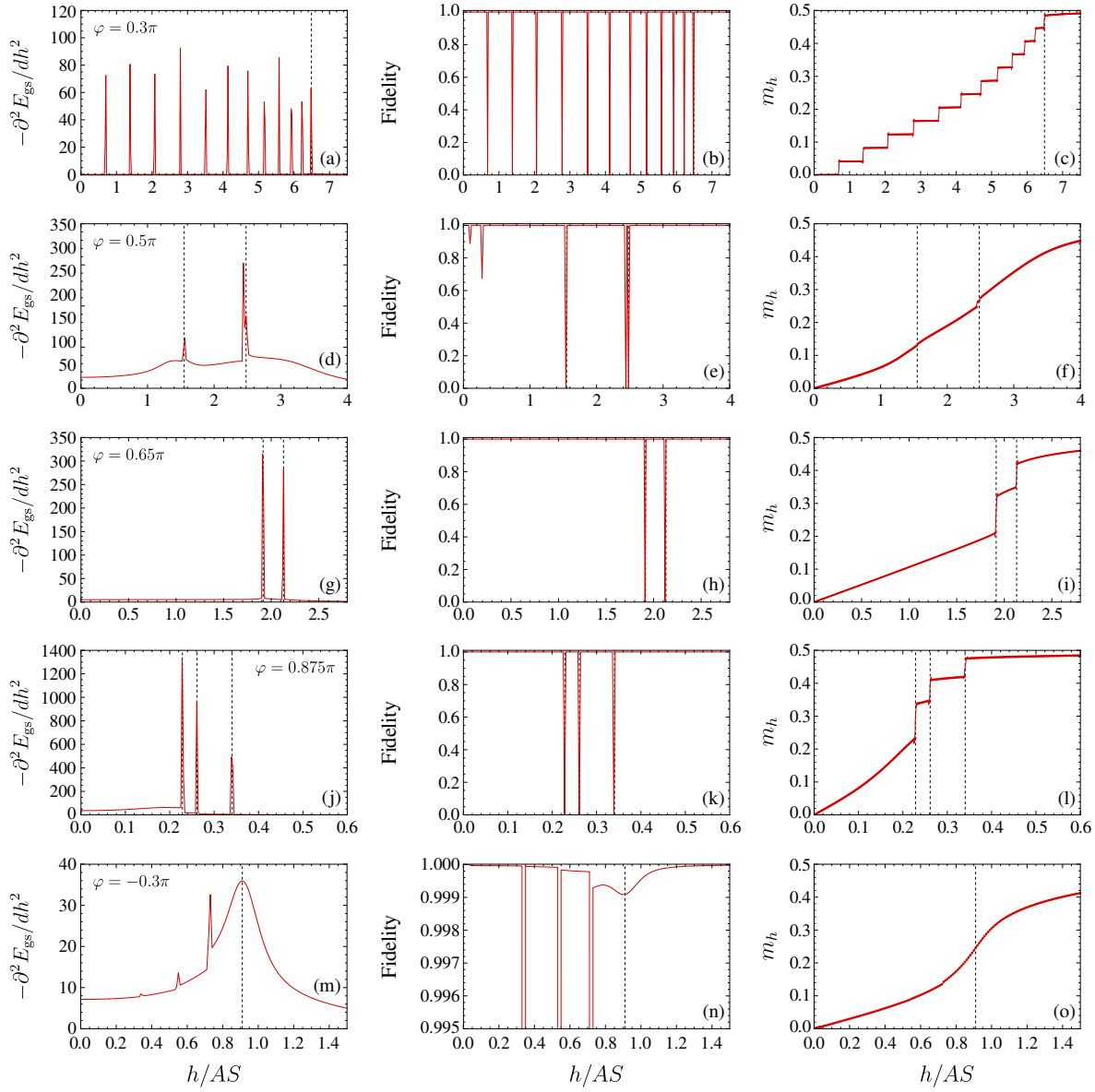

Figure 28 – 24-site ED results for the HK model in a magnetic field $\mathbf{h} \parallel [111]$ with (a-c) $\varphi = 0.3$, (d-f) $\varphi = 0.5\pi$, (g-i) $\varphi = 0.65\pi$, (j-l) $\varphi = 0.875\pi$ and (m-o) $\varphi = -0.3\pi$. A is a global energy scale related to the coupling constants by $J = A\cos\varphi$ and $K = 2A\sin\varphi$, where $S = 1/2$ is the spin size. Left: The opposite of the second derivative of the ground state energies with respect to the magnetic field. Middle: The fidelity, Eq. (6.1). Right: The magnetization per site in the direction of the magnetic field.

Source: By the author.

6.3 Results for h ∥ [111]

In Figs. 28(a-c), we see that the data collected for $\varphi = 0.3\pi$ in a [111] magnetic field show no qualitative difference with respect to the case of $\mathbf{h} \parallel [001]$. Therefore, as in the previous section, we consider that a single continuous transition occurs between the canted Néel and the polarized phases at the final peak of the second derivative of the ground state and the fidelity.

On the other hand, striking differences appear from the AF Kitaev point on. Figs. 28(d-f) show two distinguishable features at $h/AS \approx 1.55$ and 2.48 delimiting a considerably larger intermediate-field regime than that of Figs. 26(g-i). By now, several numerical studies have converged to the conclusion that these peaks represent the boundaries of the GSL mentioned in Sec. 2.1.2.[4,68–73] A remarkable property of this phase is its stability to the inclusion of Heisenberg interactions in a [111] field. While Figs. 28(g-i) confirm that the GSL is present at $\varphi = 0.65\pi$, we find that it also extends past $\varphi = 0.75\pi$,[71] where the $|J|$ becomes larger than K. In fact, Figs. 28(j-l) suggest that is might even be present at $\varphi = 0.875\pi$, near the right end of the zigzag phase. The meaning of the third peak appearing in the second derivative of the ground-state energy and in the fidelity remains unclear up to now.

Figs. 28(m-o) display the results obtained for $\varphi = -0.3\pi$. Similarly to the previous section, we observe a series of features below the smooth peak that signals the transition to the polarized phase. Yet, this time, none of the sharp peaks are associated with the selection of a subset of the three stripy patterns, since the C_3^* symmetry of the Hamiltonian is preserved. What might actually be implied is the existence of intermediate-field ordered phases, such as those presented in Chapter 4. Our preliminary static structure factor results suggest that the vortex phase is absent, as we do not find Bragg peaks at the K and K′ points, see Fig. 9(c,d), but we cannot rule out a transition to the FM star.

After assembling results for several other values of φ, we arrived at the phase diagram shown in Fig. 27(b). As in the previous section, we have refrained from determining the locations of phase boundaries below the upper critical fields. However, we emphasize that our data do not show any evidence for the existence of an ordered phase besides the canted zigzag in the interval $\varphi \in [0.5\pi, 0.87\pi]$. This supports the conclusion from Chapter 4 that the AF vortex is completely suppressed for $S = 1/2$, while suggesting that higher-order terms in $1/S$ should account for the disappearance of the remaining slither covered by the AF star. Apart from that, Fig. 27(b) reveal a good agreement between our ED and nonlinear spin-wave theory results. We also find consistency with other numerical studies[4,67,71] which focused on reduced φ intervals of the phase diagram.

One feature which has not been explored in the literature so far is the behavior of the upper critical field near the right end of the zigzag phase. Our ED results indicate that

the two-peak structure from Figs. 28(g,h) does not give way to a single peak ending at the zero-field transition point $\varphi \approx 0.900\pi$. Instead, Fig. 27(b) suggests that, for $\varphi > 0.900\pi$, a [111] magnetic field could stabilize quantum spin liquid regime between a zero-field ferromagnetic state and a high-field polarized phase. While the unlikelihood of this picture hints at a probable interference of finite-size effects, our results raise the question of whether the GSL actually reaches down to zero field. If so, does it end at quantum tricritical point shared with the canted zigzag and polarized phases? These issues are the subject of an ongoing investigation we are developing in collaboration with the DMRG experts Prof. Hong-Hao Tu, from the Technical University of Dresden, and Prof. Ying-Hai Wu, from the Huazhong University of Science and Technology.

7 CONCLUSION AND OUTLOOK

In this dissertation, we have investigated the behavior of extended Kitaev systems in an external magnetic field. Our primary concern has been to characterize the effects of quantum fluctuations on the stability and thermodynamic properties of magnetically ordered and high-field polarized phases. To this end, we have presented a detailed framework to implement spin-wave calculations for an arbitrary magnetic state, both within the linear (Chapter 3) and nonlinear regimes (Chapter 4 and Appendices B, C).

We believe that our findings from Chapter 4 can impact future theoretical and experimental research. Since the results are derived within a large-S expansion, they may be particularly relevant for higher-spin Kitaev materials. As discussed in Sec. 2.2.6, the Kitaev interaction is expected to be *antiferromagnetic* in proposed $S = 1$ systems.[22] This is a remarkable feature, for it allows a description of the zigzag magnetic order by means of the pure nearest-neighbor HK model. Our work demonstrates that nontrivial field-induced transitions between different types of antiferromagnetic orders, involving changes in the ordering wave vector and the geometry of the magnetic unit cell, are natural in such a situation. In order to make a more concrete comparison between our predictions for the HK model and the experimental results on the antimonates, in-field neutron diffraction measurements and/or angle-dependent thermodynamic measurements on single crystals would be desirable. This should allow one to elucidate the role of the observed anisotropy[58] as well as the nature of the field-induced phases. Although the Cr-based monolayers proposed as candidates for $S = 3/2$ Kitaev systems have a ferromagnetic ground state,[56,98,99] a recent study suggests that they may be driven to other paramagnetic or magnetic states by epitaxial strain.[97] In such a setup, our results show that an external field could also induce nontrivial intermediate phases, which should extend over larger ranges of exchange couplings and magnetic fields in comparison to the $S = 1/2$ and $S = 1$ cases. It would therefore be interesting to search for signatures of the corresponding metamagnetic transitions.

More broadly, the framework developed in Chapter 4 can be applied to other spin models with interactions that break SU(2) spin symmetry. This includes extensions of the HK Hamiltonian with additional interactions[14,19,85,87] or on different lattices,[84,119,132–135] but also goes beyond the scope of Kitaev magnetism, since the formalism is suitable to treat different classes of compass models[136] and even the anisotropic Hamiltonian used to describe rare-earth pyrochlores.[137,138] In cases such as these, our approach stands as an accessible complement to numerical simulations such as ED or DMRG, which work directly at the desired values of S, but are typically restricted to small lattice sizes.

In Chapter 5, we have developed a phenomenological approach to model the effect

of uniaxial pressure on the intricate low-temperature thermodynamics of α-$RuCl_3$. Our LSWT results are successful in reproducing experimental data at low magnetic fields, but are incapable of accounting for anomalous features seen in the linear TE coefficient, Grüneisen ratio and linear MS at intermediate field strengths. These findings support the existence of a quantum paramagnet lying between a magnetically ordered zigzag phase and a conventional paramagnet. Although neither our theoretical nor the experimental results from GASS *et al.*[52] provide evidence as to the nature of this intermediate-field regime, we speculate that it may represent the topological QSL suggested in earlier studies. In this case, our work helps to consolidate the existence of a transition between a spin-liquid and a high-field polarized phase.

Our contributions from Chapter 5 call for more detailed studies of the linear MS in α-$RuCl_3$ for different in- and out-of-plane field directions. Further theoretical work, in particular, is needed to characterize the field dependence of TE- and MS-related quantities near and in the putative QSL for generalized Kitaev models. This can provide a better understanding of the signatures marking field-driven transitions into and out of the QSL phase. We believe, however, that convincing results in this sense strongly rely on efforts to assess the influence of uniaxial pressure on the magnetic couplings. It would thus be desirable to have future studies tackle this issue, both from *ab initio* and phenomenological perspectives.

Finally, in Chapter 6 we take a different approach from the two previous chapters, as we employ the numerical technique of ED to study the $S = 1/2$ HK model in a magnetic field. This allows us to illustrate the consistency of our nonlinear spin-wave results from Chapter 4, while also analyzing the appearance of QSLs within the model. Our ED results agree with previous numerical studies, but also take a step further by raising a question about the existence of a new quantum tricritical point, involving the canted zigzag, U(1) GSL and [111] polarized phase. If confirmed, this can shed more light on the intriguing nature and stability of the U(1) GSL.

REFERENCES

1 JANSSEN, L.; ANDRADE, E. C.; VOJTA, M. Honeycomb-lattice Heisenberg-Kitaev model in a magnetic field: spin canting, metamagnetism, and vortex crystals. **Physical Review Letters**, v. 117, n. 27-30, p. 277202, 2016.

2 DONG, X.-Y.; SHENG, D. N. Spin-1 Kitaev-Heisenberg model on a two-dimensional honeycomb lattice. **Physical Review B**, v. 102, n. 12, p. 121102, 2020.

3 CHALOUPKA, J.; JACKELI, G.; KHALIULLIN, G. Zigzag magnetic order in the iridium oxide Na_2IrO_3. **Physical Review Letters**, v. 110, n. 9, p. 097204, 2013.

4 HICKEY, C.; TREBST, S. Emergence of a field-driven U(1) spin liquid in the Kitaev honeycomb model. **Nature Communications**, v. 10, n. 1, p. 530, 2019.

5 JOHNSON, R. D. *et al.* Monoclinic crystal structure of α-$RuCl_3$ and the zigzag antiferromagnetic ground state. **Physical Review B**, v. 92, n. 23, p. 235119, 2015.

6 PARK, S.-Y. *et al.* **Emergence of the isotropic Kitaev honeycomb lattice with two-dimensional Ising universality in α-$RuCl_3$**. 2016. Available from: https://arxiv.org/abs/1609.05690. Accessible at: 1 June 2020.

7 CAO, H. B. *et al.* Low-temperature crystal and magnetic structure of α-$RuCl_3$. **Physical Review B**, v. 93, n. 13, p. 134423, 2016.

8 WOLTER, A. U. B. *et al.* Field-induced quantum criticality in the Kitaev system α-$RuCl_3$. **Physical Review B**, v. 96, n. 4, p. 041405, 2017.

9 PESIN, D.; BALENTS, L. Mott physics and band topology in materials with strong spin–orbit interaction. **Nature Physics**, v. 6, n. 5, p. 376–381, 2010.

10 HASAN, M. Z.; KANE, C. L. Colloquium: topological insulators. **Reviews of Modern Physics**, v. 82, n. 4, p. 3045–3067, 2010.

11 WITCZAK-KREMPA, W.; CHEN, G.; KIM, Y. B.; BALENTS, L. Correlated quantum phenomena in the strong spin-orbit regime. **Annual Review of Condensed Matter Physics**, v. 5, n. 1, p. 57, 2014.

12 SCHAFFER, R.; LEE, E. K.-H.; YANG, B.-J.; KIM, Y. B. Recent progress on correlated electron systems with strong spin-orbit coupling. **Reports on Progress in Physics**, v. 79, n. 9, p. 094504, 2016.

13 YAN, B.; FELSER, C. Topological materials: Weyl semimetals. **Annual Review of Condensed Matter Physics**, v. 8, n. 1, p. 337–354, 2017.

14 TREBST, S. **Kitaev materials**. 2017. Available from: https://arxiv.org/abs/1408.4811. Accessible at: 15 Feb. 2019.

15 MORIYA, T. Anisotropic superexchange interaction and weak ferromagnetism. **Physical Review**, v. 120, n. 1, p. 91–98, 1960.

16 KHALIULLIN, G. Orbital order and fluctuations in Mott insulators. **Progress of Theoretical Physics Supplement**, v. 160, p. 155–202, 2005. DOI: 10.1143/PTPS.160.155.

17 JACKELI, G.; KHALIULLIN, G. Mott insulators in the strong spin-orbit coupling limit: from Heisenberg to a quantum compass and Kitaev models. **Physical Review Letters**, v. 102, n. 1, p. 017205, 2009.

18 CHALOUPKA, J.; JACKELI, G.; KHALIULLIN, G. Kitaev-Heisenberg model on a honeycomb lattice: possible exotic phases in iridium oxides A_2IrO_3. **Physical Review Letters**, v. 105, n. 2, p. 027204, 2010.

19 WINTER, S. M. *et al.* Models and materials for generalized Kitaev magnetism. **Journal of Physics:** condensed matter, v. 29, n. 49, p. 493002, 2017.

20 NATORI, W. M. H.; ANDRADE, E. C.; MIRANDA, E.; PEREIRA, R. G. Chiral spin-orbital liquids with nodal lines. **Physical Review Letters**, v. 117, n. 1, p. 017204, 2016.

21 NATORI, W. M. H.; ANDRADE, E. C.; PEREIRA, R. G. SU(4)-symmetric spin-orbital liquids on the hyperhoneycomb lattice. **Physical Review B**, v. 98, n. 19, p. 195113, 2018.

22 STAVROPOULOS, P. P.; PEREIRA, D.; KEE, H.-Y. Microscopic mechanism for a higher-spin Kitaev model. **Physical Review Letters**, v. 123, n. 3, p. 037203, 2019.

23 KITAEV, A. Anyons in an exactly solved model and beyond. **Annals of Physics**, v. 321, n. 1, p. 2, 2006.

24 BALENTS, L. Spin liquids in frustrated magnets. **Nature**, v. 464, n. 7286, p. 199–208, 2010.

25 SAVARY, L.; BALENTS, L. Quantum spin liquids: a review. **Reports on Progress in Physics**, v. 80, n. 1, p. 016502, 2016.

26 BROHOLM, C. *et al.* Quantum spin liquids. **Science**, v. 367, n. 6475, 2020. DOI: 10.1126/science.aay0668.

27 CHOI, S. K. *et al.* Spin waves and revised crystal structure of honeycomb iridate Na_2IrO_3. **Physical Review Letters**, v. 108, n. 12, p. 127204, 2012.

28 SINGH, Y. *et al.* Relevance of the Heisenberg-Kitaev model for the honeycomb lattice iridates A_2IrO_3. **Physical Review Letters**, v. 108, n. 12, p. 127203, 2012.

29 CHUN, S. H. *et al.* Direct evidence for dominant bond-directional interactions in a honeycomb lattice iridate Na_2IrO_3. **Nature Physics**, v. 11, n. 6, p. 462–466, 2015.

30 PLUMB, K. W. *et al.* α-$RuCl_3$: a spin-orbit assisted Mott insulator on a honeycomb lattice. **Physical Review B**, v. 90, n. 4, p. 041112, 2014.

31 SEARS, J. A. *et al.* Magnetic order in α-$RuCl_3$: A honeycomb-lattice quantum magnet with strong spin-orbit coupling. **Physical Review B**, v. 91, n. 14, p. 144420, 2015.

32 BANERJEE, A. *et al.* Proximate Kitaev quantum spin liquid behaviour in a honeycomb magnet. **Nature Materials**, v. 15, p. 733, 2016. DOI: 10.1038/nmat4604.

33 MAJUMDER, M. *et al.* Anisotropic $Ru^{3+}4d^5$ magnetism in the α-$RuCl_3$ honeycomb system: susceptibility, specific heat, and zero-field NMR. **Physical Review B**, v. 91, n. 18, p. 180401, 2015.

34 KUBOTA, Y. *et al.* Successive magnetic phase transitions in α-$RuCl_3$: XY-like frustrated magnet on the honeycomb lattice. **Physical Review B**, v. 91, n. 9, p. 094422, 2015.

35 DAS, S. D. *et al.* Magnetic anisotropy of the alkali iridate Na_2IrO_3 at high magnetic fields: evidence for strong ferromagnetic Kitaev correlations. **Physical Review B**, v. 99, n. 8, p. 081101, 2019.

36 YADAV, R. *et al.* Kitaev exchange and field-induced quantum spin-liquid states in honeycomb α-$RuCl_3$. **Scientific Reports**, v. 6, p. 37925, 2016. DOI: 10.1038/srep37925.

37 CÔNSOLI, P. M.; JANSSEN, L.; VOJTA, M.; ANDRADE, E. C. Heisenberg-Kitaev model in a magnetic field: $1/S$ expansion. **Physical Review B**, v. 102, n. 15, p. 155134, 2020.

38 WINTER, S. M. *et al.* Probing α-$RuCl_3$ beyond magnetic order: effects of temperature and magnetic field. **Physical Review Letters**, v. 120, n. 7, p. 077203, 2018.

39 CHERN, L. E.; KANEKO, R.; LEE, H.-Y.; KIM, Y. B. Magnetic field induced competing phases in spin-orbital entangled Kitaev magnets. **Physical Review Research**, v. 2, n. 1, p. 013014, 2020.

40 LAMPEN-KELLEY, P. *et al.* **Field-induced intermediate phase in α-$RuCl_3$:** non-coplanar order, phase diagram, and proximate spin liquid. 2018. Available from: https://arxiv.org/abs/1807.06192. Accessible at: 1 June 2020.

41 BANERJEE, A. *et al.* Excitations in the field-induced quantum spin liquid state of α-$RuCl_3$. **NPJ Quantum Materials**, v. 3, n. 1, p. 1–7, 2018.

42 LEAHY, I. A. *et al.* Anomalous thermal conductivity and magnetic torque response in the honeycomb magnet α-$RuCl_3$. **Physical Review Letters**, v. 118, n. 18, p. 187203, 2017.

43 SEARS, J. A. *et al.* Phase diagram of α-$RuCl_3$ in an in-plane magnetic field. **Physical Review B**, v. 95, n. 18, p. 180411, 2017.

44 KASAHARA, Y. *et al.* Majorana quantization and half-integer thermal quantum Hall effect in a Kitaev spin liquid. **Nature**, v. 559, n. 7713, p. 227–231, 2018. DOI: 10.1038/s41586-018-0274-0.

45 BAEK, S.-H. *et al.* Evidence for a field-induced quantum spin liquid in α-$RuCl_3$. **Physical Review Letters**, v. 119, n. 3, p. 037201, 2017.

46 DO, S.-H. *et al.* Majorana fermions in the Kitaev quantum spin system α-$RuCl_3$. **Nature Physics**, v. 13, n. 11, p. 1079–1084, 2017.

47 BALZ, C. *et al.* Finite field regime for a quantum spin liquid in α-$RuCl_3$. **Physical Review B**, v. 100, n. 6, p. 060405, 2019.

48 SANDILANDS, L. J. *et al.* Scattering continuum and possible fractionalized excitations in α-$RuCl_3$. **Physical Review Letters**, v. 114, n. 14, p. 147201, 2015.

49 WANG, Z. *et al.* Magnetic excitations and continuum of a possibly field-induced quantum spin liquid in α-$RuCl_3$. **Physical Review Letters**, v. 119, n. 22, p. 227202, 2017.

50 WELLM, C. *et al.* Signatures of low-energy fractionalized excitations in α-$RuCl_3$ from field-dependent microwave absorption. **Physical Review B**, v. 98, n. 18, p. 184408, 2018.

51 YOKOI, T. *et al.* **Half-integer quantized anomalous thermal Hall effect in the Kitaev material α-$RuCl_3$**. 2020. Available from: https://arxiv.org/abs/2001.01899. Accessible at: June 1, 2020.

52 GASS, S. *et al.* Field-induced transitions in the Kitaev material α-$RuCl_3$ probed by thermal expansion and magnetostriction. **Physical Review B**, v. 101, n. 24, p. 245158, 2020.

53 VINKLER-AVIV, Y.; ROSCH, A. Approximately quantized thermal Hall effect of chiral liquids coupled to phonons. **Physical Review X**, v. 8, n. 3, p. 031032, 2018.

54 YE, M.; HALÁSZ, G. B.; SAVARY, L.; BALENTS, L. Quantization of the Thermal Hall Conductivity at Small Hall Angles. **Physical Review Letters**, v. 121, n. 14, p. 147201, 2018.

55 GAO, Y. H. *et al.* Thermal Hall signatures of non-Kitaev spin liquids in honeycomb Kitaev materials. **Physical Review Research**, v. 1, n. 1, p. 013014, 2019.

56 LEE, I. *et al.* Fundamental spin interactions underlying the magnetic anisotropy in the Kitaev ferromagnet CrI_3. **Physical Review Letters**, v. 124, n. 1, p. 017201, 2020.

57 ZVEREVA, E. A. *et al.* Zigzag antiferromagnetic quantum ground state in monoclinic honeycomb lattice antimonates $A_3Ni_2SbO_6$, (A=Li, Na). **Physical Review B**, v. 92, n. 14, p. 144401, 2015.

58 WERNER, J. *et al.* Anisotropy-governed competition of magnetic phases in the honeycomb quantum magnet $Na_3Ni_2SbO_6$ studied by dilatometry and high-frequency ESR. **Physical Review B**, v. 95, n. 21, p. 214414, 2017.

59 BASKARAN, G.; SEN, D.; SHANKAR, R. Spin-S Kitaev model: classical ground states, order from disorder, and exact correlation functions. **Physical Review B**, v. 78, n. 11, p. 115116, 2008.

60 JANSSEN, L.; VOJTA, M. Heisenberg-Kitaev physics in magnetic fields. **Journal of Physics:** condensed matter, v. 31, n. 42, p. 423002, 2019.

61 COLEMAN, P. **Introduction to many-body physics**. Cambridge: Cambridge University Press, 2015.

62 LIEB, E. H. Flux phase of the half-filled band. **Physical Review Letters**, v. 73, n. 16-17, p. 2158–2161, 1994.

63 ESCHMANN, T. *et al.* Thermodynamic classification of three-dimensional Kitaev spin liquids. **Physical Review B**, v. 102, n. 7, p. 075125, 2020.

64 HERMANNS, M.; KIMCHI, I.; KNOLLE, J. Physics of the Kitaev model: fractionalization, dynamic correlations, and material connections. **Annual Review of Condensed Matter Physics**, v. 9, p. 17–33, 2018. DOI: 10.1146/annurev-conmatphys-033117-053934.

65 NAYAK, C. *et al.* Non-Abelian anyons and topological quantum computation. **Reviews of Modern Physics**, v. 80, n. 3, p. 1083–1159, 2008.

66 TONG, D. **Lectures on the quantum Hall effect**. 2016. Available from: https://arxiv.org/abs/1606.06687. Accessible at: 6 Feb. 2019.

67 JIANG, H.-C.; GU, Z.-C.; QI, X.-L.; TREBST, S. Possible proximity of the Mott insulating iridate Na_2IrO_3 to a topological phase: phase diagram of the Heisenberg-Kitaev model in a magnetic field. **Physical Review B**, v. 83, n. 24, p. 245104, 2011.

68 GOHLKE, M.; MOESSNER, R.; POLLMANN, F. Dynamical and topological properties of the Kitaev model in a [111] magnetic field. **Physical Review B**, v. 98, n. 1, p. 014418, 2018.

69 ZHU, Z.; KIMCHI, I.; SHENG, D. N.; FU, L. Robust non-Abelian spin liquid and a possible intermediate phase in the antiferromagnetic Kitaev model with magnetic field. **Physical Review B**, v. 97, n. 24, p. 241110, 2018.

70 RONQUILLO, D. C.; VENGAL, A.; TRIVEDI, N. Signatures of magnetic-field-driven quantum phase transitions in the entanglement entropy and spin dynamics of the Kitaev honeycomb model. **Physical Review B**, v. 99, n. 14, p. 140413, 2019.

71 JIANG, Y.-F.; DEVEREAUX, T. P.; JIANG, H.-C. Field-induced quantum spin liquid in the Kitaev-Heisenberg model and its relation to α-$RuCl_3$. **Physical Review B**, v. 100, n. 16, p. 165123, 2019.

72 PATEL, N. D.; TRIVEDI, N. Magnetic field-induced intermediate quantum spin liquid with a spinon Fermi surface. **Proceedings of the National Academy of Sciences**, v. 116, n. 25, p. 12199–12203, 2019.

73 ZOU, L.; HE, Y.-C. Field-induced QCD_3-Chern-Simons quantum criticalities in Kitaev materials. **Physical Review Research**, v. 2, n. 1, p. 013072, 2020.

74 NASU, J.; KATO, Y.; KAMIYA, Y.; MOTOME, Y. Successive Majorana topological transitions driven by a magnetic field in the Kitaev model. **Physical Review B**, v. 98, n. 6, p. 060416, 2018.

75 LIANG, S. *et al.* Intermediate gapless phase and topological phase transition of the Kitaev model in a uniform magnetic field. **Physical Review B**, v. 98, n. 5, p. 054433, 2018.

76 BEDNORZ, J. G.; MÜLLER, K. A. Possible high T_c superconductivity in the Ba-La-Cu-O system. **Zeitschrift für Physik B:** condensed matter, v. 64, n. 2, p. 189–193, 1986.

77 FAZEKAS, P. **Lecture notes on electron correlation and magnetism**. Singapore: World Scientific, 1999. (Series in modern condensed matter physics, v.5).

78 KUGEL, K. I.; KHOMSKII, D. I. The Jahn-Teller effect and magnetism: transition metal compounds. **Soviet Physics Uspekhi**, v. 25, n. 4, p. 231–256, 1982.

79 SHEKHTMAN, L.; ENTIN-WOHLMAN, O.; AHARONY, A. Moriya's anisotropic superexchange interaction, frustration, and Dzyaloshinsky's weak ferromagnetism. **Physical Review Letters**, v. 69, n. 5, p. 836–839, 1992.

80 YILDIRIM, T.; HARRIS, A. B.; AHARONY, A.; ENTIN-WOHLMAN, O. Anisotropic spin Hamiltonians due to spin-orbit and Coulomb exchange interactions. **Physical Review B**, v. 52, n. 14, p. 10239–10267, 1995.

81 IREGUI, J. O.; CORBOZ, P.; TROYER, M. Probing the stability of the spin-liquid phases in the Kitaev-Heisenberg model using tensor network algorithms. **Physical Review B**, v. 90, n. 19, p. 195102, 2014.

82 GOTFRYD, D. *et al.* Phase diagram and spin correlations of the Kitaev-Heisenberg model: importance of quantum effects. **Physical Review B**, v. 95, n. 2, p. 024426, 2017.

83 GOHLKE, M.; VERRESEN, R.; MOESSNER, R.; POLLMANN, F. Dynamics of the Kitaev-Heisenberg model. **Physical Review Letters**, v. 119, n. 15, p. 157203, 2017.

84 KIMCHI, I.; VISHWANATH, A. Kitaev-Heisenberg models for iridates on the triangular, hyperkagome, kagome, fcc, and pyrochlore lattices. **Physical Review B**, v. 89, n. 1, p. 014414, 2014.

85 RAU, J. G.; LEE, E. K.-H.; KEE, H.-Y. Generic spin model for the honeycomb iridates beyond the Kitaev Limit. **Physical Review Letters**, v. 112, n. 7, p. 077204, 2014.

86 RAU, J. G.; KEE, H.-Y. **Trigonal distortion in the honeycomb iridates:** proximity of zigzag and spiral phases in Na_2IrO_3. 2014. Available from: https://arxiv.org/abs/1408.4811. Accessible at: 1 June 2020.

87 JANSSEN, L.; ANDRADE, E. C.; VOJTA, M. Magnetization processes of zigzag states on the honeycomb lattice: identifying spin models for α-$RuCl_3$ and Na_2IrO_3. **Physical Review B**, v. 96, n. 6, p. 064430, 2017.

88 COOKMEYER, J.; MOORE, J. E. Spin-wave analysis of the low-temperature thermal Hall effect in the candidate Kitaev spin liquid α-$RuCl_3$. **Physical Review B**, v. 98, n. 6, p. 060412, 2018.

89 WINTER, S. M.; LI, Y.; JESCHKE, H. O.; VALENTÍ, R. Challenges in design of Kitaev materials: magnetic interactions from competing energy scales. **Physical Review B**, v. 93, n. 21, p. 214431, 2016.

90 WINTER, S. M. *et al.* Breakdown of magnons in a strongly spin-orbital coupled magnet. **Nature Communications**, v. 8, n. 1, p. 1152, 2017.

91 ZHU, Z.; WENG, Z.-Y.; SHENG, D. N. Magnetic field induced spin liquids in $S = 1$ Kitaev honeycomb model. **Physical Review Research**, v. 2, n. 2, p. 022047, 2020.

92 KHAIT, I.; STAVROPOULOS, P. P.; KEE, H.-Y.; KIM, Y. B. **Characterizing spin-one Kitaev quantum spin liquids**. 2020. Available from: https://arxiv.org/abs/2001.06000. Accessible at: 1 June 2020.

93 HICKEY, C. *et al.* Field-driven gapless spin liquid in the spin-1 Kitaev honeycomb model. **Physical Review Research**, v. 2, n. 2, p. 023361, 2020.

94 KURBAKOV, A. I. *et al.* Zigzag spin structure in layered honeycomb $Li_3Ni_2SbO_6$: a combined diffraction and antiferromagnetic resonance study. **Physical Review B**, v. 96, n. 2, p. 024417, 2017.

95 KOGA, A.; TOMISHIGE, H.; NASU, J. Ground-state and thermodynamic properties of an $S = 1$ Kitaev model. **Journal of the Physical Society of Japan**, v. 9, n. 6, p. 1575, 2018.

96 OITMAA, J.; KOGA, A.; SINGH, R. R. P. Incipient and well-developed entropy plateaus in spin-S Kitaev models. **Physical Review B**, v. 98, n. 21, p. 214404, 2018.

97 XU, C. *et al.* Possible Kitaev quantum spin liquid state in 2D materials with $S = 3/2$. **Physical Review Letters**, v. 124, n. 8, p. 087205, 2020.

98 GONG, C. *et al.* Discovery of intrinsic ferromagnetism in two-dimensional van der Waals crystals. **Nature**, v. 546, n. 7657, p. 265–269, 2017.

99 HUANG, B. *et al.* Layer-dependent ferromagnetism in a van der Waals crystal down to the monolayer limit. **Nature**, v. 546, n. 7657, p. 270–273, 2017.

100 LUTTINGER, J. M.; TISZA, L. Theory of dipole interaction in crystals. **Physical Review**, v. 70, n. 11-12, p. 954–964, 1946.

101 HOLSTEIN, T.; PRIMAKOFF, H. Field Dependence of the Intrinsic Domain Magnetization of a Ferromagnet. **Physical Review**, v. 58, n. 12, p. 1098–1113, 1940.

102 ALTLAND, A.; SIMONS, B. D. **Condensed matter field theory**. 2nd ed. New York: Cambridge University Press, 2010.

103 RAU, J. G.; MCCLARTY, P. A.; MOESSNER, R. Pseudo-Goldstone gaps and order-by-quantum disorder in frustrated magnets. **Physical Review Letters**, v. 121, n. 23, p. 237201, 2018.

104 BLAIZOT, J.; RIPKA, G. **Quantum theory of finite systems**. Cambridge: MIT Press, 1986.

105 WESSEL, S.; MILAT, I. Quantum fluctuations and excitations in antiferromagnetic quasicrystals. **Physical Review B**, v. 71, n. 10, p. 104427, 2005.

106 COLPA, J. Diagonalization of the quadratic boson Hamiltonian. **Physica A:** statistical mechanics and its applications, v. 93, n. 3-4, p. 327–353, 1978.

107 SMIT, R. L. *et al.* Magnon damping in the zigzag phase of the Kitaev-Heisenberg-Γ model on a honeycomb lattice. **Physical Review B**, v. 101, n. 5, p. 054424, 2020.

108 PRICE, C.; PERKINS, N. B. Finite-temperature phase diagram of the classical Kitaev-Heisenberg model. **Physical Review B**, v. 88, n. 2, p. 024410, 2013.

109 ZHITOMIRSKY, M. E.; NIKUNI, T. Magnetization curve of a square-lattice Heisenberg antiferromagnet. **Physical Review B**, v. 57, n. 9, p. 5013–5016, 1998.

110 ANDERSON, P. W. An approximate quantum theory of the antiferromagnetic ground state. **Physical Review**, v. 86, n. 5, p. 694–701, 1952.

111 KUBO, R. The spin-wave theory of antiferromagnetics. **Physical Review**, v. 87, n. 4, p. 568–580, 1952.

112 COLETTA, T.; LAFLORENCIE, N.; MILA, F. Semiclassical approach to ground-state properties of hard-core bosons in two dimensions. **Physical Review B**, v. 85, n. 10, p. 104421, 2012.

113 CHUBUKOV, A. V.; SACHDEV, S.; SENTHIL, T. Large-S expansion for quantum antiferromagnets on a triangular lattice. **Journal of Physics:** condensed matter, v. 6, n. 42, p. 8891, 1994.

114 CHERNYSHEV, A. L.; ZHITOMIRSKY, M. E. Spin waves in a triangular lattice antiferromagnet: decays, spectrum renormalization, and singularities. **Physical Review B**, v. 79, n. 14, p. 144416, 2009.

115 JOSHI, D. G.; COESTER, K.; SCHMIDT, K. P.; VOJTA, M. Nonlinear bond-operator theory and $1/d$ expansion for coupled-dimer magnets. I. Paramagnetic phase. **Physical Review B**, v. 91, n. 9, p. 094404, 2015.

116 JOSHI, D. G.; VOJTA, M. Nonlinear bond-operator theory and $1/d$ expansion for coupled-dimer magnets. II. Antiferromagnetic phase and quantum phase transition. **Physical Review B**, v. 91, n. 9, p. 094405, 2015.

117 ROUSOCHATZAKIS, I.; SIZYUK, Y.; PERKINS, N. B. Quantum spin liquid in the semiclassical regime. **Nature Communications**, v. 87, n. 6, p. 063703, 2018.

118 TAKAGI, H. *et al.* Concept and realization of Kitaev quantum spin liquids. **Nature Reviews Physics**, v. 1, n. 4, p. 264–280, 2019.

119 KRÜGER, W. G. F.; VOJTA, M.; JANSSEN, L. Heisenberg-Kitaev models on hyperhoneycomb and stripy-honeycomb lattices: 3D-2D equivalence of ordered states and phase diagrams. **Physical Review Research**, v. 2, n. 1, p. 012021, 2020.

120 GOHLKE, M.; CHERN, L. E.; KEE, H.-Y.; KIM, Y. B. Emergence of nematic paramagnet via quantum order-by-disorder and pseudo-Goldstone modes in Kitaev magnets. **Physical Review Research**, v. 2, n. 4, p. 043023, 2020.

121 CHALOUPKA, J.; KHALIULLIN, G. Magnetic anisotropy in the Kitaev model systems Na_2IrO_3 and $RuCl_3$. **Physical Review B**, v. 94, n. 6, p. 064435, 2016.

122 SIZYUK, Y.; WÖLFLE, P.; PERKINS, N. B. Selection of direction of the ordered moments in Na_2IrO_3 and α-$RuCl_3$. **Physical Review B**, v. 94, n. 8, p. 085109, 2016.

123 WU, C. Orbital ordering and frustration of p-band Mott insulators. **Physical Review Letters**, v. 100, n. 20, p. 200406, 2008.

124 ZHU, L.; GARST, M.; ROSCH, A.; SI, Q. Universally diverging Grüneisen parameter and the magnetocaloric effect close to quantum critical points. **Physical Review Letters**, v. 91, n. 6, p. 066404, 2003.

125 GARST, M.; ROSCH, A. Sign change of the Grüneisen parameter and magnetocaloric effect near quantum critical points. **Physical Review B**, v. 72, n. 20, p. 205129, 2005.

126 HE, M. *et al.* Uniaxial and hydrostatic pressure effects in α-$RuCl_3$ single crystals via thermal-expansion measurements. **Journal of Physics:** condensed matter, v. 30, n. 38, p. 385702, 2018.

127 LANDAU, L.; LIFSHITZ, E. **Theory of elasticity, theoretical physics**. Oxford: Butterworth-Heinemann, 1998. (Course of theoretical physics, v. 7).

128 CHAIKIN, P.; LUBENSKY, T. **Principles of condensed matter physics**. Cambridge: Cambridge University Press, 2000.

129 BARRERA, G. D.; BRUNO, J. A. O.; BARRON, T.; ALLAN, N. Negative thermal expansion. **Journal of Physics:** condensed matter, v. 17, n. 4, p. R217, 2005.

130 YADAV, R. *et al.* Strain-and pressure-tuned magnetic interactions in honeycomb Kitaev materials. **Physical Review B**, v. 98, n. 12, p. 121107, 2018.

131 SANDVIK, A. W. Computational studies of quantum spin systems. **AIP Conference Proceedings**, v. 1297, n. 1, p. 135–338, 2010.

132 LEE, E. K.-H.; KIM, Y. B. Theory of magnetic phase diagrams in hyperhoneycomb and harmonic-honeycomb iridates. **Physical Review B**, v. 91, n. 6, p. 064407, 2015.

133 O'BRIEN, K.; HERMANNS, M.; TREBST, S. Classification of gapless Z_2 spin liquids in three-dimensional Kitaev models. **Physical Review B**, v. 93, n. 8, p. 085101, 2016.

134 LI, M.; ROUSOCHATZAKIS, I.; PERKINS, N. B. Reentrant incommensurate order and anomalous magnetic torque in the Kitaev magnet β-Li_2IrO_3. **Physical Review Research**, v. 2, n. 3, p. 033328, 2020.

135 JANSSEN, L.; KOCH, S.; VOJTA, M. Magnon dispersion and dynamic spin response in three-dimensional spin models for α-$RuCl_3$. **Physical Review B**, v. 101, n. 17, p. 174444, 2020.

136 NUSSINOV, Z.; BRINK, J. van den. Compass models: theory and physical motivations. **Reviews of Modern Physics**, v. 87, n. 1, p. 1 – 59, 2015.

137 ROSS, K. A.; SAVARY, L.; GAULIN, B. D.; BALENTS, L. Quantum excitations in quantum spin ice. **Physical Review X**, v. 1, n. 2, p. 021002, 2011.

138 RAU, J. G.; MOESSNER, R.; MCCLARTY, P. A. Magnon interactions in the frustrated pyrochlore ferromagnet $Yb_2Ti_2O_7$. **Physical Review B**, v. 100, n. 10, p. 104423, 2019.

139 WEN, X. **Quantum field theory of many-body systems:** from the origin of sound to an origin of light and electrons. Oxford: Oxford University Press, 2004. (Oxford graduate texts).

Appendix

APPENDIX A – DETAILS ON THE NUMERICAL IMPLEMENTATION OF SPIN-WAVE CALCULATIONS

In this appendix, we comment on a few technical details regarding the numerical implementation of the spin-wave calculations of Chapters 4 and 5. This entire procedure was carried out by using *Mathematica 11*, which has the chief advantage of allowing us to manipulate symbolic expressions.

Following the guidelines of Chapter 3, our program initially requires three inputs to describe a given magnetic phase: (i) the number of sites per magnetic unit cell, N_s, of the phase; (ii) the classical parametrization angles, $\{\phi_\mu, \theta_\mu\}$; (iii) the different $\boldsymbol{\delta}$ vectors which connect pairs of interacting sites on the lattice. By using the first two pieces of information, the program computes the rotation matrices $\mathbb{R}_\mu \equiv \mathbb{R}\left(\phi_\mu, \theta_\mu\right)$ shown Eq. (3.2) and combines the results with the $\boldsymbol{\delta}$ vectors to determine the $2N_\mathrm{s} \times 2N_\mathrm{s}$ LSW matrix, $\mathbb{M}_\mathbf{k}$. While Secs. 4.2 and 4.3.1 deal specifically with the HK model, one can easily adapt the procedure leading to the matrices γ^μ_{mn} and r^μ_ν in Eqs. (4.3) and (4.5) to treat different Hamiltonians. By directly computing the appropriate generalizations of Eqs. (4.14) and (4.15), the code constructs $\mathbb{M}_\mathbf{k}$ as a function of the magnetic coupling constants $\mathcal{J}_0$, the magnitude of the magnetic field h/S, the wave vector $\mathbf{k}$ and, in the event of a accidental continuous degeneracy, an extra angle ξ (see Sec. 4.9.4).

As discussed in Sec. 3.2.1, physical quantities can be calculated in the LSW regime by diagonalizing the Bogoliubov matrix, $\sigma_3\mathbb{M}_\mathbf{k}$. To this end, we simply use the *Mathematica* built-in functions `Eigenvalues` and `Eigenvectors`. When using the latter, however, one must not forget to enforce the orthonormality conditions expressed in Eq. (3.28). As shown in Sec. 3.2, this procedure is generally well-defined except when the system has a type I zero mode at $\mathbf{k} = \mathbf{Q}$. In such cases, an attempt to normalize the zero-mode eigenvector $V_{\mathbf{Q}\mu}$ leads to a divergence, since $V^\dagger_{\mathbf{Q}\mu}\sigma_3 V_{\mathbf{Q}\mu} = 0$. If the diagonalization of $\sigma_3\mathbb{M}_\mathbf{Q}$ is absolutely necessary, one must therefore employ a special treatment for the zero-mode subspace.[104] Fortunately, this detour can often be avoided, as explained below.

Finally, we note that several physical observables, such as the thermodynamic quantities computed in Chapter 5, are given in terms of a sum over the first magnetic BZ. Rather than taking the thermodynamic limit and performing a numerical integration, e.g. via Simpson's rule, we find it more convenient to evaluate these sums directly over a refined but finite grid*. As long as the integrand $I\left(\mathbf{k}\right)$ does not present poles of order higher than 1, this procedure can be carried out straightforwardly, and we can thus avoid the nuisance of dealing with zero modes by selecting a grid that does not fall on top of high-symmetry points. In practice, we always adjust the first magnetic BZ so that it

* A commonly used alternative is to perform Monte Carlo integration.[114]

has a rectangular shape and choose a grid with a similar aspect ratio. In other words, if the first BZ has dimensions Δk_x and Δk_y, we create a grid with n_x and n_y subdivisions along the k_x and k_y axes, respectively, such that $n_x/n_y \approx \Delta k_x/\Delta k_y$. Typically, we take $\max(n_x, n_y) \in [230, 300]$.

APPENDIX B – COMPUTATION OF QUANTUM CORRECTIONS TO THE PARAMETRIZATION ANGLES (CHAPTER 4)

In this appendix, we develop the general theory for the computation corrections to the parametrization angles of noncollinear ordered phases of the HK model in a magnetic field. As outlined in Sec. 4.4, this calculation involves the linear ($n = 1$) and cubic ($n = 3$) contributions to the spin-wave Hamiltonian, Eq. (3.4). Starting with the former, we rewrite Eq. (4.7) as

$$\begin{aligned}
\mathcal{H}_1 &= \frac{1}{\sqrt{2}} {\sum_{i\mu\gamma}}' \left[\left(\gamma^{\mu}_{13} + i\gamma^{\mu}_{23}\right) a^{\dagger}_{i\mu} + \left(\gamma^{\mu}_{31} + i\gamma^{\mu}_{32}\right) a^{\dagger}_{j\nu_\gamma} \right] + \frac{h/S}{\sqrt{2}} \sum_{i\mu} r^{\mu}_1 a^{\dagger}_{i\mu} + \text{h.c.} \\
&= \frac{1}{\sqrt{2}} {\sum_{i\mu\gamma}}' \left[\left(\gamma^{\mu}_{13} + i\gamma^{\mu}_{23}\right) a^{\dagger}_{i\mu} + \left(\gamma^{\nu_\gamma}_{13} + i\gamma^{\nu_\gamma}_{23}\right) a^{\dagger}_{j\nu_\gamma} \right] + \frac{h/S}{\sqrt{2}} \sum_{i\mu} r^{\mu}_1 a^{\dagger}_{i\mu} + \text{h.c.} \\
&= \frac{1}{\sqrt{2}} \sum_{i\mu} \left[\sum_{\gamma} \left(\gamma^{\mu}_{13} + i\gamma^{\mu}_{23}\right) + \frac{h}{S} r^{\mu}_1 \right] a^{\dagger}_{i\mu} + \text{h.c.} \\
&= \sqrt{\frac{N_c}{2}} \sum_{\mu} \left[\sum_{\gamma} \left(\gamma^{\mu}_{13} + i\gamma^{\mu}_{23}\right) + \frac{h}{S} r^{\mu}_1 \right] a^{\dagger}_{\mathbf{0}\mu} + \text{h.c.}
\end{aligned} \tag{B.1}$$

In the first step, we have made use of the fact that $\gamma^{\mu}_{mn} = \gamma^{\nu_\gamma}_{nm}$. Meanwhile, the final step follows from the fact that that only the bosonic mode with momentum $\mathbf{k} = \mathbf{0}$ is left after a Fourier transform:

$$\sum_i a_{i\mu} = \frac{1}{\sqrt{N_c}} \sum_{\mathbf{k}} a_{\mathbf{k}\mu} \overbrace{\sum_i e^{i\mathbf{k}\cdot\mathbf{r}_{i\mu}}}^{=N_c\,\delta_{\mathbf{k}\mathbf{0}}} = \sqrt{N_c}\, a_{\mathbf{0}\mu}. \tag{B.2}$$

As discussed in Sec. 4.4, one must account for $1/S$ corrections to the classical parametrization angles when going beyond quadratic order of the spin-wave Hamiltonian. As long as we stop the expansion of the spin-wave Hamiltonian at order $n = 3$, it is consistent to expand the corrected angles to first order in S^{-1}, as in Eqs. (4.22) and (4.23). This yields $\mathcal{H}_1\left(\tilde{\boldsymbol{\phi}}, \tilde{\boldsymbol{\theta}}\right) = S^{-1}\delta\mathcal{H}_1 + \mathcal{O}\left(S^{-2}\right)$ with

$$\delta\mathcal{H}_1 = \sqrt{\frac{N_c}{2}} \sum_{\mu} \left[\boldsymbol{\nabla} Z_\mu \big|_{\boldsymbol{\phi},\boldsymbol{\theta}} \begin{pmatrix} \boldsymbol{\delta\theta} \\ \boldsymbol{\delta\phi} \end{pmatrix} a^{\dagger}_{\mathbf{0}\mu} + \text{h.c.} \right] \tag{B.3}$$

and

$$Z_\mu\left(\tilde{\boldsymbol{\phi}}, \tilde{\boldsymbol{\theta}}\right) = \sum_{\gamma} \left(\tilde{\gamma}^{\mu}_{13} + i\tilde{\gamma}^{\mu}_{23}\right) + \frac{h}{S} \tilde{r}^{\mu}_1. \tag{B.4}$$

Here, we employ the shorthand notation $\tilde{\gamma}^{\mu}_{mn} = \gamma^{\mu}_{mn}\left(\tilde{\boldsymbol{\phi}}, \tilde{\boldsymbol{\theta}}\right)$ and $\tilde{r}^{\mu}_1 = r^{\mu}_1\left(\tilde{\boldsymbol{\theta}}\right)$. The gradient of Z_μ is then given by

$$\boldsymbol{\nabla} Z_\mu = \left(\frac{\partial Z_\mu}{\partial \tilde{\phi}_1}, \ldots, \frac{\partial Z_\mu}{\partial \tilde{\phi}_{N_s}}, \frac{\partial Z_\mu}{\partial \tilde{\theta}_1}, \ldots, \frac{\partial Z_\mu}{\partial \tilde{\theta}_{N_s}} \right). \tag{B.5}$$

Each of the partial derivatives above can be written more explicitly as

$$\frac{\partial Z_\mu}{\partial \tilde{\phi}_\nu} = \sum_\gamma \frac{\partial}{\partial \tilde{\phi}_\nu} \left(\tilde{\gamma}^\mu_{13} + i\tilde{\gamma}^\mu_{23}\right), \qquad \frac{\partial Z_\mu}{\partial \tilde{\theta}_\nu} = \sum_\gamma \frac{\partial}{\partial \tilde{\theta}_\nu} \left(\tilde{\gamma}^\mu_{13} + i\tilde{\gamma}^\mu_{23}\right) + \delta_{\mu\nu} \frac{h}{S} \frac{\partial \tilde{r}^\mu_1}{\partial \tilde{\theta}_\nu}. \tag{B.6}$$

With this, we proceed to the cubic term, $n = 3$. Since we are only accounting for NLO effects in $1/S$, it suffices to evaluate all γ^μ matrices at the classical parametrization angles, $(\boldsymbol{\phi}, \boldsymbol{\theta})$. According to our discussion in Sec. 4.4, we must now cast Eq. (4.10) into normal order, $\mathcal{H}_3 = :\mathcal{H}_3: + \mathcal{H}_3^{(1)}$. By using Wick's theorem,[139] one finds that the residual linear term, $\mathcal{H}_3^{(1)}$, depends on the averages

$$\begin{aligned} m_{\mu\nu,\gamma} &= \left\langle a^\dagger_{i\mu} a_{j\nu_\gamma} \right\rangle & \Delta_{\mu\nu,\gamma} &= \left\langle a_{i\mu} a_{j\nu_\gamma} \right\rangle \\ n_\mu &= \left\langle a^\dagger_{i\mu} a_{i\mu} \right\rangle & \delta_\mu &= \left\langle a_{i\mu} a_{i\mu} \right\rangle . \end{aligned} \tag{B.7}$$

Note that we explicitly indicate the bond type γ involved in the parameters $\Delta_{\mu\nu,\gamma}$ and $m_{\mu\nu,\gamma}$. This distinction is essential here due to the bond-dependent nature of the Kitaev interactions. Our considerations from Sec. 3.2.1 allow us to express all of the quantities above in terms of the eigenvectors $V_{\mathbf{k}\mu}$ of $\sigma_3 \mathbb{M}_{\mathbf{k}}$ with positive eigenvalues. If we denote by $\boldsymbol{\delta}_\gamma$ the vector that connects a site μ to its nearest neighbor ν along a γ-bond, we obtain

$$\begin{aligned} m_{\mu\nu,\gamma} &= \frac{1}{N_c} \sum_{\mathbf{k}\lambda} e^{-i\mathbf{k}\cdot\boldsymbol{\delta}_\gamma} V^*_{\mathbf{k}\lambda,N_\mathrm{s}+\nu_\gamma} V_{\mathbf{k}\lambda,N_\mathrm{s}+\mu} & n_\mu &= \frac{1}{N_c} \sum_{\mathbf{k}\lambda} \left|V_{\mathbf{k}\lambda,N_\mathrm{s}+\mu}\right|^2 \\ \Delta_{\mu\nu,\gamma} &= \frac{1}{N_c} \sum_{\mathbf{k}\lambda} e^{-i\mathbf{k}\cdot\boldsymbol{\delta}_\gamma} V^*_{\mathbf{k}\lambda,N_\mathrm{s}+\nu_\gamma} V_{\mathbf{k}\lambda,\mu} & \delta_\mu &= \frac{1}{N_c} \sum_{\mathbf{k}\lambda} V^*_{\mathbf{k}\lambda,N_\mathrm{s}+\mu} V_{\mathbf{k}\lambda,\mu}. \end{aligned} \tag{B.8}$$

The single-boson term $\mathcal{H}_3^{(1)}$ then reads

$$\mathcal{H}_3^{(1)} = -\sqrt{\frac{N_\mathrm{c}}{2}} \sum_{\mu\gamma}{}' \left[m^*_{\mu\gamma} \left(\gamma^\mu_{31} + i\gamma^\mu_{32}\right) + \Delta_{\mu\gamma} \left(\gamma^\mu_{31} - i\gamma^\mu_{32}\right) + n_{\nu_\gamma} \left(\gamma^\mu_{13} + i\gamma^\mu_{23}\right) \right] a^\dagger_{\mathbf{0}\mu} + \text{h.c.}. \tag{B.9}$$

The corrected reference state is determined by demanding the additional linear term to be zero, $\mathcal{H}_3^{(1)} + \delta\mathcal{H}_1 \stackrel{!}{=} 0$. From Eqs. (B.3) and (B.9), one can see that this leads to a system of linear equations

$$\boldsymbol{\nabla} Z_\mu \big|_{\boldsymbol{\phi},\boldsymbol{\theta}} \begin{pmatrix} \boldsymbol{\delta\theta} \\ \boldsymbol{\delta\phi} \end{pmatrix} = x_\mu, \qquad \mu \in \{1, \ldots, N_\mathrm{s}\}, \tag{B.10}$$

with coefficients

$$x_\mu = \sum_\gamma \left[n_{\nu_\gamma} \left(\gamma^\mu_{13} + i\gamma^\mu_{23}\right) + m^*_{\mu\gamma} \left(\gamma^\mu_{31} + i\gamma^\mu_{32}\right) + \Delta_{\mu\gamma} \left(\gamma^\mu_{31} - i\gamma^\mu_{32}\right) \right]. \tag{B.11}$$

Although we have developed the results with reference to the HK Hamiltonian, it is worth noting that the formalism remains valid for other spin models under a suitable adaptation of the γ^μ matrices, Eq. (4.4).

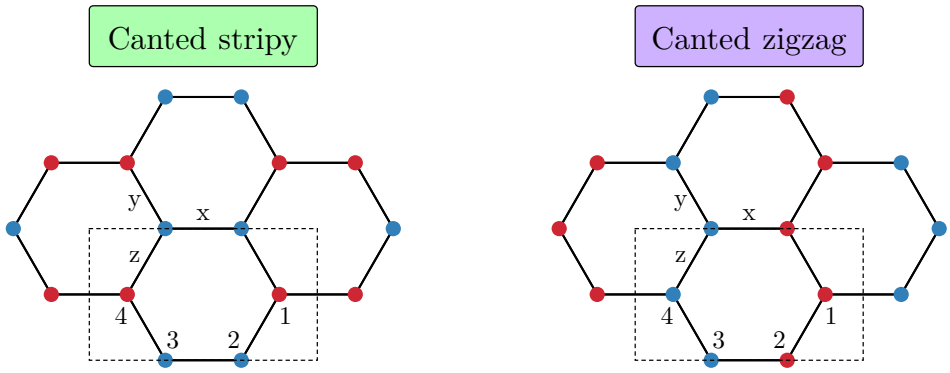

Figure 29 – Representation of the patterns of the canted stripy and canted zigzag phases used to obtain the results in Eqs. (B.14) and (B.13). Each of the four magnetic sublattices is labeled by a number from 1 to $N_\mathrm{s} = 4$.

Source: By the author.

As an application of the procedure, we present explicit results for $\mathbf{h} \parallel [001]$. In this case, all ordered phases are coplanar, so that the azimuthal angles ϕ_μ are exempt from $1/S$ corrections. Moreover, the fact that ObD mechanisms do not interfere with the uniform canting allows us to compute a single quantity, $\delta\theta = \delta\theta_\mu$, $\forall\, \mu \in \{1, \ldots, N_\mathrm{s}\}$, for each phases.

Starting with the canted Néel,

$$\delta\theta = \frac{\cot\theta}{3J+K}\left[\left(J\sum_{\gamma=x,y,z} + \frac{K}{2}\sum_{\gamma=x,y}\right)(\Delta_\gamma + m_\gamma - n_1)\right]. \tag{B.12}$$

Interestingly, the expression above singles out the source of the divergence of $\delta\theta$ at $h = h_{\mathrm{c}0}$. In the presence of a nonzero Kitaev interaction, the LSW Hamiltonian becomes nondiagonal in the Holstein-Primakoff bosons $\left\{a^\dagger_{\mathbf{k}\mu}, a_{\mathbf{k}\mu}\right\}$ at $h = h_{\mathrm{c}0}$. This fact, which follows from the polarized state not being an eigenstate of the Hamiltonian, causes the mean-field averages $\Delta_\gamma \equiv \Delta_{12,\gamma}$, $m_{12,\gamma} \equiv m_\gamma$ and n_1, as well as the entire term in square brackets in Eq. (B.12), to have nonzero values. Therefore, we conclude that $\delta\theta$ diverges as $\cot\theta$ when $h \to h_{\mathrm{c}0}$, whereas the product $\tan\theta\,\delta\theta$ is generally nonzero and finite away from the Kitaev point $\varphi = \pi/2$.

In the treatment of the canted stripy and canted zigzag, one must bear in mind that a magnetic field along [001] direction partially lifts the degeneracy between three distinct patterns of each phase, as discussed in Sec. 4.1.2. In the case of the canted stripy (zigzag), the pattern with stripes (zigzag chains) running parallel (perpendicularly) to the z-bonds becomes unfavorable. By using the configurations represented in Fig. 29, one finds

$$\delta\theta = \frac{\cot\theta}{J+K}\left[\left(J+\frac{K}{2}\right)\left(\Delta_{32,x} + m^*_{32,x} - n_2\right) - \frac{K}{2}\left(\Delta_{34,y} + m^*_{34,y} + n_4\right)\right]. \tag{B.13}$$

for the canted zigzag and

$$\delta\theta = \frac{\cot\theta}{2J}\left[J\sum_{\gamma=y,z}\left(\Delta_{34,\gamma} + m^*_{34,\gamma} - n_4\right) + \frac{K}{2}\left(\Delta_{32,x} + \Delta_{34,y} + m^*_{32,x} + m^*_{34,y} + n_2 - n_4\right)\right]. \tag{B.14}$$

for the canted stripy. Note that Eqs. (B.13) and (B.14) are also proportional to $\cot\theta$, so that the argument presented below Eq. (B.12) applies for all ordered phases in a [001] field.

APPENDIX C – NONLINEAR SPIN-WAVE THEORY IN THE [001] POLARIZED PHASE (CHAPTER 4)

Finally, we discuss the computation of $1/S$ corrections to the magnon spectrum of the high-field polarized phase. In a general system, the NLO contributions in $1/S$ are generated by the cubic and quartic terms of spin-wave Hamiltonian. Nevertheless, because the classical reference state for the polarized phase is collinear, combinations of the type $S^{\pm}_{i\mu}S^{3}_{j\nu}$ do not appear after one performs the required rotations to the spin coordinate system (see Chapter 3 for details). Consequently, no contributions with an odd number of bosons are produced by the Holstein-Primakoff transformation. For this reason, we shall focus solely on the quartic terms of the spin-wave Hamiltonian. The decoupling $\mathcal{H}_4 = :\mathcal{H}_4: + :\mathcal{H}_4^{(2)}: + \mathcal{H}_4^{(0)}$ leads to a quadratic term with a general form

$$
\begin{aligned}
:\mathcal{H}_4^{(2)}: = f_1 \sum_{\mathbf{k}\mu} :a^{\dagger}_{\mathbf{k}\mu}a_{\mathbf{k}\mu}: + \sum_{\mathbf{k}} \left[f_2(\mathbf{k}) :a^{\dagger}_{\mathbf{k}1}a^{\dagger}_{-\mathbf{k}2}: + f_3(\mathbf{k}) :a_{-\mathbf{k}1}a^{\dagger}_{-\mathbf{k}2}: \right] \\
+ f_4 \sum_{\mathbf{k}\mu} :a^{\dagger}_{\mathbf{k}\mu}a^{\dagger}_{-\mathbf{k}\mu}: + \text{h.c.},
\end{aligned}
\tag{C.1}
$$

Note that, independent of the direction of the magnetic field, neither the function f_1 nor f_4 depend on the wave vector $\mathbf{k}$, because they multiply pairs of bosons related to the same sublattice. Now one uses the Bogoliubov transformation to rewrite Eq. (C.1) in terms of the Bogoliubov quasiparticles. The result reads

$$
\mathcal{H}_4^{(2)} = \frac{1}{2} \sum_{\mathbf{k}} \beta^{\dagger}_{\mathbf{k}} \left(\sum_{n=1}^{4} \mathbb{S}_{\mathbf{k}n} \right) \beta_{\mathbf{k}} + \text{h.c.}
\tag{C.2}
$$

with

$$
\begin{aligned}
\mathbb{S}_{\mathbf{k}1} &= f_1 \sum_{\mu=1}^{4} |p_\mu\rangle \langle p_\mu| & \mathbb{S}_{\mathbf{k}2} &= f_2(\mathbf{k}) |p_1\rangle \langle p_4| + f_2(-\mathbf{k}) |p_2\rangle \langle p_3| \\
\mathbb{S}_{\mathbf{k}4} &= f_4 \sum_{\mu=1}^{2} \left(|p_\mu\rangle \langle p_{\mu+2}| + |p_{\mu+2}\rangle \langle p_\mu| \right) & \mathbb{S}_{\mathbf{k}3} &= f_3(\mathbf{k}) |p_3\rangle \langle p_4| + f_3(-\mathbf{k}) |p_2\rangle \langle p_1|
\end{aligned}
\tag{C.3}
$$

and

$$
\langle p_\mu| = \begin{pmatrix} V_{\mathbf{k}1,\mu} & V_{\mathbf{k}2,\mu} & W_{-\mathbf{k}1,\mu} & W_{-\mathbf{k}2,\mu} \end{pmatrix}, \qquad \mu \in \{1, \ldots, 4\}.
\tag{C.4}
$$

We thus find the self-energy

$$
\Sigma_{\mathbf{k}} = \sum_{n=1}^{4} \mathbb{S}_{\mathbf{k}n} + \text{h.c.},
\tag{C.5}
$$

which is evidently Hermitian.

As in Appendix B, we can use Wick's theorem to compute the coefficients f_n in terms of the averages from Eq. (B.7). While laborious, this procedure is straightforward.

In the case of $\mathbf{h} \parallel [001]$, the results simplify considerably due to the fact that all averages from Eq. (B.7) are real and obey the relations

$$\begin{aligned} n_1 &= n_2 = n, & m_x &= m_y, \\ \delta_1 &= \delta_2 = 0, & \Delta_x &= -\Delta_y \text{ and } \Delta_z = 0. \end{aligned} \tag{C.6}$$

Taking all of this into account, we arrive at

$$\begin{cases} f_1 = \frac{J}{2}\left(3n - \sum_\gamma m_\gamma\right) + K\left(n - m_x - \Delta_x\right) \\ f_2\left(\mathbf{k}\right) = \left(J\Delta_x - Kn\right)\left(e^{i\mathbf{k}\cdot\boldsymbol{\delta}_x} - e^{i\mathbf{k}\cdot\boldsymbol{\delta}_y}\right) \\ f_3\left(\mathbf{k}\right) = J\sum_\gamma\left(m_\gamma - n\right)e^{i\mathbf{k}\cdot\boldsymbol{\delta}_\gamma} + K\left[2m_z e^{i\mathbf{k}\cdot\boldsymbol{\delta}_z} - n\left(e^{i\mathbf{k}\cdot\boldsymbol{\delta}_x} + e^{i\mathbf{k}\cdot\boldsymbol{\delta}_y}\right)\right] \\ f_4 = 0. \end{cases} \tag{C.7}$$

Along with the eigenvectors of the Bogoliubov transformation, the expressions above complete the information necessary to compute the spectrum at NLO in $1/S$.

Examples of the resulting spectra are shown in Fig. 30. Overall, this panel is a good illustration of the key concepts discussed in Sec. 4.6. First, note how magnon interactions at $\varphi = 0.3\pi$ lead to a finite gap, Δ_1, as $h \to h_{\mathrm{c0}}^+$. In contrast, the spectra immediately above the transitions to the canted zigzag and canted stripy are shown to diverge at the corresponding instability wave vectors, $\mathbf{Q} = M_1, M_3$, as $h \to h_{\mathrm{c0}}^+$. Both of these observations are consistent with the considerations from Sec. 4.6. A common feature to all dispersions is that interactions cause the energy of the excitations to *increase*. At a fixed value of h, this reduces the density of magnons at low energies and hence allows the polarize phase to remain stable over a larger portion of the phase diagram. Finally, we note that the nonlinear spin-wave spectra in the bottom row of Fig. 30 display a kink at the Γ point, which becomes more pronounced as one approaches h_{c0}. This can be understood as an enhancement of the asymmetry between the k_x and k_y directions already seen in the LSW spectrum, possibly due to three-magnon decay processes. However, we leave further clarification on this point for future work.

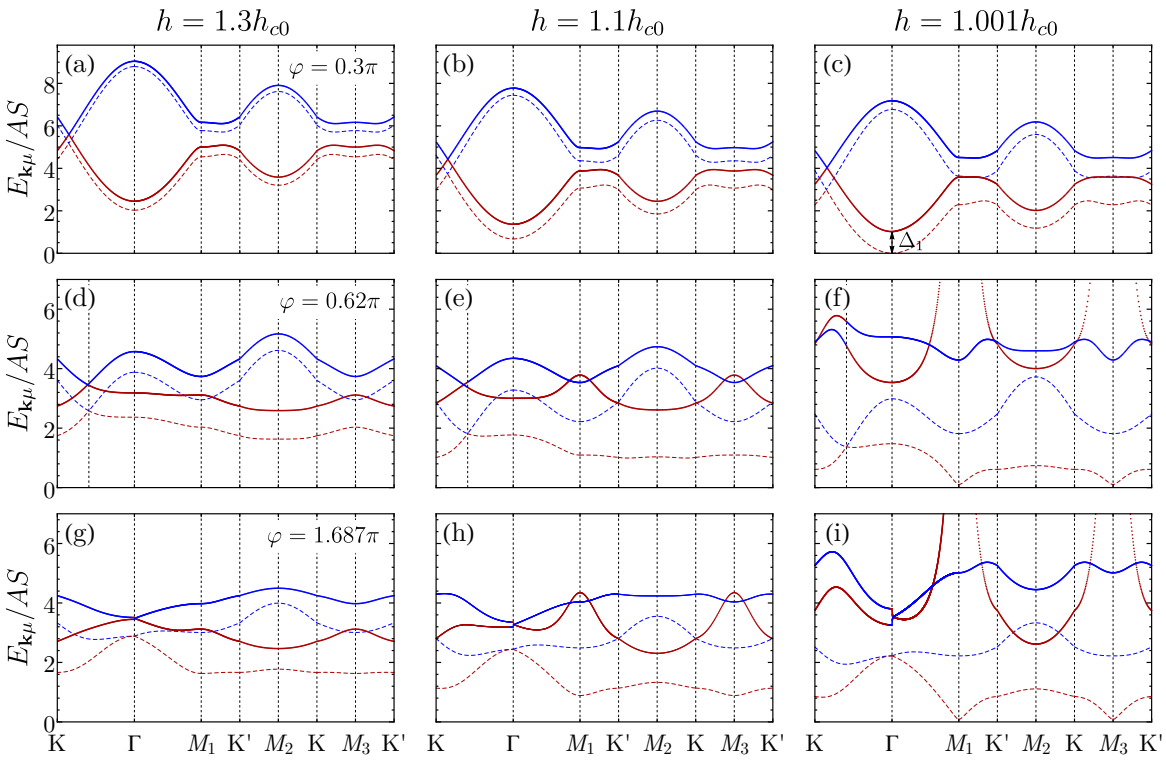

Figure 30 – Nonlinear spin-wave spectra (dots) in the [001] polarized phase including NLO contributions in $1/S$ for $S = 1/2$. The dashed lines correspond to the LSW results. Each row illustrates the effect of lowering the magnetic field from 130% to 100.1% of the classical critical field, h_{c0}, at a constant value of φ. Plots (a)-(c) show data for $\varphi = 0.3\pi$, whereas (d)-(f) and (g)-(i) correspond to $\varphi = 0.62\pi$ and $\varphi = 1.687\pi$, respectively. The spectrum acquires a finite and nonzero gap as $h \to h_{c0}^{+}$ above the canted Néel phase, whereas the gap diverges as one approaches the transition to the canted zigzag or canted stripy phases. This is consistent with the discussion regarding the reduction of the critical field in Sec. 4.6.

Source: By the author.